Mechanics and microstructure modeling of the solid electrolyte $Li_7La_3Zr_2O_{12}$

Von der Fakultät für Georessourcen und Materialtechnik der
Rheinisch-Westfälischen Technischen Hochschule Aachen

zur Erlangung des akademischen Grades eines

Doktors der Naturwissenschaften

genehmigte Dissertation

vorgelegt von

Roland Sandt, M.Sc.

Berichter: Univ.-Prof. Dr. rer. nat. Robert Spatschek
Univ.-Prof. Dr. rer. nat. Robert Svendsen

Tag der mündlichen Prüfung: 10.09.2024

Publications contained in this dissertation:

R. Sandt, Y. Wang, & R. Spatschek, Investigation of mechanical properties of garnet structured $Li_7La_3Zr_2O_{12}$ under Al^{3+} and Ta^{5+} co-substitutions. *Solid State Ionics* **402**, 116364 (2023).
DOI: https://doi.org/10.1016/j.ssi.2023.116364

R. Sandt, Y. Le Bouar & R. Spatschek, Quantum annealing for microstructure equilibration with long-range elastic interactions. *Scientific Reports* **13**, 6036 (2023).
DOI: https://doi.org/10.1038/s41598-023-33232-w

R. Sandt, Y. Le Bouar & R. Spatschek, Microstructure equilibration with consideration of elastic and interfacial interactions via quantum annealing with application to the solid electrolyte LLZO. *Physical Review Research* **6**, 033047 (2024).
DOI: https://doi.org/10.1103/PhysRevResearch.6.033047

R. Sandt & R. Spatschek, Efficient low temperature Monte Carlo sampling using quantum annealing. *Scientific Reports* **13**, 6754 (2023).
DOI: https://doi.org/10.1038/s41598-023-33828-2

Hochschulschriftenvermerk: D 82 (Diss. RWTH Aachen University, 2024)

Abstract

The efficient electrical energy storage is an important challenge of research, where many crucial topics like the usage of electrical vehicles are strongly related in the overall context of the proceeding climate change. Solid state batteries are suitable candidates for next-generation battery systems, and especially the solid state electrolyte $Li_7La_3Zr_2O_{12}$ (LLZO) influences the ionic conductivity and the mechanical stability of the whole battery system. Therefore, a mechanical characterization and the understanding of microstructure formations of LLZO are necessary, and are in the scope of the present work. For that, established and novel developed approaches and scale bridging descriptions are used in the framework of the mechanical properties of LLZO.

On the electronic scale, density functional theory (DFT) simulations allow the precise ab initio calculation of the mechanical properties of cubic LLZO, which is stabilized via co-substitutions of aluminium and tantalum. Here, prescreening methods, exploiting an electronic model, an artificial neural network and preliminary DFT calculations, determine energetically suitable substitution positions and therefore increase the efficiency of the productive computations. The directional properties of Young's modulus and shear modulus indicate an anisotropy of LLZO, however, the elastic properties of isotropic polycrystalline LLZO are not deviating much from the averaged outcomes. The resulting values of the lattice constants, elastic moduli and hardness show the influence of the co-substitutions, but overall the structural and mechanical properties of cubic LLZO are preserved.

Realistic LLZO is a porous material, whose characteristics cannot be captured via DFT simulations, therefore a scale bridging description via a differential effective medium theory approach is used to investigate the influence of pores on the mechanical parameters. For a porosity of 10 % in LLZO, a decay of 27 % for Young's modulus is expected. The general agreement between the predicted and experimental values is good, allowing to use this model for consistency checks of experimental and theoretical outcomes.

Depending on the doping level, the microstructure consists of a mixture of a tetragonal

and a cubic phase, where the latter is beneficial due to its higher ionic conductivity. The formation of an equilibrated microstructure therefore has a strong influence on the overall electrochemical performance of this solid electrolyte material. Mechanical mismatches between the phases are expected to contribute to the spatial arrangement of the phases, which is difficult to assess with established modeling approaches. Therefore, a novel quantum annealing (QA) method for the determination of the equilibrium microstructure with long-range elastic interactions between coherent grains was developed. Comparisons with classical algorithms show that quantum annealing can accelerate the simulations drastically, even for huge system sizes with several thousands of grains, where conventional algorithms exhibit high computational demand. In order to simulate realistic LLZO microstructures, Voronoi tesselations are used to generate the grains. The QA method is demonstrated under consideration of systems with shear and tetragonal eigenstrains, whose resulting microstructures are additionally analyzed regarding applied tensile strains and random grain rotations.

For the application of the developed QA approach to LLZO, the DFT results are used in order to formulate the eigenstrain. The resulting microstructures show the interplay between chemical and elastic contributions, where elastic effects favor a formation of ion conducting channels in doped LLZO.

In materials science the physical properties at finite temperatures are of high interest, while so far the presented DFT and QA simulations of LLZO consider only ground state energies at 0 K. Thermal expansion is a crucial issue in solid state batteries, which cannot be characterised via the presented QA microstructure equilibrations. Therefore, a QA method for the efficient sampling of finite temperature properties is developed, which shows high performance at low temperatures and operates at low computational demand. The performance of the approach is demonstrated using benchmarking scenarios of spin glasses and Ising chains. The QA sampling is very accurate where conventional approaches fail and therefore complements classical methods perfectly.

Kurzfassung

Die effiziente Speicherung elektrischer Energie stellt eine wichtige Herausforderung in der Wissenschaft dar, wo mehrere essentielle Themen, wie die Nutzung elektrischer Fortbewegungsmittel, eng im Kontext des fortschreitenden Klimawandels stehen. Festkörperakkumulatoren sind geeignete Kandidaten für Batteriesysteme der nächsten Generation, wo insbesondere der Festkörperelektrolyt $Li_7La_3Zr_2O_{12}$ (LLZO) die ionische Leitfähigkeit und die mechanische Stabilität des gesamten Batteriesystems beeinflusst. Daher ist die mechanische Charakterisierung und das Verständnis der Bildung von Mikrostrukturen in LLZO von elementarer Bedeutung und stellt den thematischen Rahmen der vorliegenden Arbeit dar. Dafür werden etablierte und neuartige, entwickelte Ansätze und skalenübergreifende Beschreibungen im Kontex der mechanischen Eigenschaften von LLZO genutzt.

Auf der elektronischen Skala erlauben Simulationen mittels der Dichtefunktionaltheorie (DFT) die präzise ab initio Berechnung der mechanischen Eigenschaften kubischen LLZOs, welches durch kombinierte Substituierungen mit Aluminium und Tantal stabilisiert wird. Mittels Screeningmethoden, die ein elektronisches Modell, ein künstliches neuronales Netzwerk und initiale DFT Berechnungen ausnutzen, werden energetisch passende Substitutionspositionen bestimmt und damit die Effizienz weiterer Berechnungen erhöht. Die richtungsabhängigen Eigenschaften des Elastizitätsmoduls und des Schermoduls zeigen eine Anisotropie von LLZO, wobei die elastischen Eigenschaften von isotropem polykristallinem LLZO unwesentlich von den gemittelten Resultaten abweichen. Die resultierenden Werte für die Gitterkonstanten, elastischen Module und Härte offenbaren den Einfluss der kombinierten Substitutionen, allerdings bleiben insgesamt strukturelle und mechanische Eigenschaften des kubischen LLZOs erhalten.

Realistisches LLZO ist ein poröses Material, dessen Charakteristiken nicht mittels DFT Simulationen erfasst werden können, was die Nutzung einer skalenübergreifenden Beschreibung mittels eines Ansatzes der differentiellen effektiven Mediumtheorie zur Untersuchung des Einflusses von Poren auf die mechanischen Parameter nötig macht. Für eine Porösität

von 10 % in LLZO ist eine Abnahme von 27 % des Elastizitätsmoduls zu erwarten. Die allgemeine Übereinstimmung zwischen den vorhergesagten und experimentellen Werten ist überzeugend und erlaubt die Nutzung dieses Modells für die Konsistenzprüfung experimenteller und theoretischer Resultate.

In Abhängigkeit des Substituierungsgehalts besteht die Mikrostruktur aus einer Mischung von tetragonalen und kubischen Phasen, wobei letztere aufgrund ihrer höheren ionischen Leitfähigkeit erwünscht ist. Die Formation einer equilibrierten Mikrostruktur hat daher einen starken Einfluss auf die gesamte elektrochemische Leistung des Festelektrolyts. Mechanische Missverhältnisse zwischen den Phasen tragen zur räumlichen Anordnung der Phasen bei, welche nur schwer mit bestehenden Modellierungsansätzen zugänglich ist. Daher wurde eine neuartige *quantum annealing* (QA) Methode für die Bestimmung von equilibrierten Mikrostrukturen mit langreichweitigen elastischen Interaktionen zwischen kohärenten Körnern entwickelt. Vergleiche mit klassischen Algorithmen zeigen, dass QA, sogar für große Systeme mit mehreren tausend Körnern, die Simulationen drastisch beschleunigen kann, wo konventionelle Algorithmen einen hohen Rechenaufwand aufweisen. Um realistische Mikrostrukturen von LLZO zu simulieren, werden Voronoi Diagramme zur Erzeugung von Körnern verwendet. Die QA Methode wird unter Berücksichtigung von Systemen mit geschertem und tetragonalem *eigenstrain* demonstriert, dessen resultierenden Mikrostrukturen zusätzlich im Hinblick auf externe Verformungen und zufälligen Kornrotationen analysiert werden.

Für die Anwendung der entwickelten QA Methode auf LLZO, werden die DFT Resultate genutzt, um den *eigenstrain* zu formulieren. Die resultierenden Mikrostrukturen zeigen das Zusammenspiel chemischer und elastischer Beiträge, wobei elastische Effekte zur Bildung von ionisch leitenden Kanälen in dotiertem LLZO führen.

In den Materialwissenschaften sind die physikalischen Eigenschaften bei endlichen Temperaturen von großem Interesse, während die bisher thematisierten DFT und QA Simulationen lediglich den Grundzustand bei 0 K berücksichtigen. Die thermische Ausdehnung ist ein wichtiges Thema in Festkörperbatterien, welches nicht mit den beschriebenen QA Gleichgewichtsmikrostrukturen charakterisiert werden kann. Daher wird eine QA Methode für das effiziente *sampling* bei endlichen Temperaturen entwickelt, welche große Übereinstimmungen bei niedrigen Temperaturen und niedrigen Rechenaufwand zeigt. Die Leistung des Ansatzes wird anhand von Spingläsern und Isingketten demonstriert. Das QA *sampling* ist sehr präzise, wo konventionelle Algorithmen versagen, und ergänzt daher bestehende, klassische Methoden ideal.

Acknowledgements

First and foremost I would like to thank Prof. Dr. Robert Spatschek for being an extraordinary doctoral supervisor. His guidance, support, and motivation have been invaluable to me.

I also would like to thank all current and former colleagues at IEK-2 for the amazing time at the campus. Especially, I would like to thank Lara C. P. dos Santos and Yang Hu for making my PhD journey unforgettable.

I would like to thank Prof. Dr. Yann Le Bouar for essential discussions and feedback.

I also thank Prof. Dr. Bob Svendsen for being my second examiner.

My research was funded via the BMBF project Meet HiEnD 3 and the Helmholtz project ZeDaBase. Our successful project time and our project meetings were always very interesting and inspiring to me.

Last but not least, I thank my friends and my family for supporting me throughout my life. In particular, I would like to express my greatest gratitude to Anna for all the support and love she has given me.

List of publications

B. Celik, R. Sandt, L.C.P. dos Santos, & R. Spatschek, Prediction of Battery Cycle Life Using Early-Cycle Data, Machine Learning and Data Management. *Batteries* **8**, 266 (2022).

R. Sandt, Y. Le Bouar & R. Spatschek, Quantum annealing for microstructure equilibration with long-range elastic interactions. *Scientific Reports* **13**, 6036 (2023).

R. Sandt & R. Spatschek, Efficient low temperature Monte Carlo sampling using quantum annealing. *Scientific Reports* **13**, 6754 (2023).

R. Sandt, Y. Wang, & R. Spatschek, Investigation of mechanical properties of garnet structured $Li_7La_3Zr_2O_{12}$ under Al^{3+} and Ta^{5+} co-substitutions. *Solid State Ionics* **402**, 116364 (2023).

L.C.P. dos Santos, T. Hang, R. Sandt, M. Finsterbusch, Y. Le Bouar & R. Spatschek, Elastic energy driven multivariant selection in martensites via quantum annealing. *Physical Review Research* **6**, 023076 (2024).

R. Sandt, Y. Le Bouar & R. Spatschek, Microstructure equilibration with consideration of elastic and interfacial interactions via quantum annealing with application to the solid electrolyte LLZO. *Physical Review Research* **6**, 033047 (2024).

Y. Hu, R. Sandt & R. Spatschek, Practical feature filter strategy to machine learning for small datasets in chemistry. *Scientific Reports* **14**, 20449 (2024).

Publications that contributed to the dissertation

Publication 1: **R. Sandt, Y. Wang, & R. Spatschek**, Investigation of mechanical properties of garnet structured $Li_7La_3Zr_2O_{12}$ under Al^{3+} and Ta^{5+} co-substitutions. *Solid State Ionics* **402**, 116364 (2023).
DOI: `https://doi.org/10.1016/j.ssi.2023.116364`

Publication 2: **R. Sandt, Y. Le Bouar & R. Spatschek**, Quantum annealing for microstructure equilibration with long-range elastic interactions. *Scientific Reports* **13**, 6036 (2023).
DOI: `https://doi.org/10.1038/s41598-023-33232-w`

Publication 3: **R. Sandt, Y. Le Bouar & R. Spatschek**, Microstructure equilibration with consideration of elastic and interfacial interactions via quantum annealing with application to the solid electrolyte LLZO. *Physical Review Research* **6**, 033047 (2024).
DOI: `https://doi.org/10.1103/PhysRevResearch.6.033047`

Publication 4: **R. Sandt & R. Spatschek**, Efficient low temperature Monte Carlo sampling using quantum annealing. *Scientific Reports* **13**, 6754 (2023).
DOI: `https://doi.org/10.1038/s41598-023-33828-2`

Contributions to the publications

The principle ideas, the formulation of the research goals, the design of methodology and the creation of models were developed by R. Sandt (publications 1-4) and R. Spatschek (publications 2-4).

Programming, designing and implementation of computer code were done by R. Sandt (publications 1-4), R. Spatschek (publications 2-4) and Y. Le Bouar (publication 2).

Statistical, mathematical, computational and other formal techniques to analyze and synthesize data were performed by R. Sandt (publications 1-4), R. Spatschek (publications 1-4), Y. Le Bouar (publications 2-3) and Y. Wang (publication 1).

The research and investigation process, especially the data collection, were done by R. Sandt (publications 1-4) and Y. Wang (publication 1).

Data curation, validation of research outputs and visualization and presentation of the published work were done by R. Sandt (publications 1-4).

The initial drafts of the published work and revisions were written by R. Sandt (publications 1-4), while the manuscripts were reviewed and edited by R. Spatschek (publications 1-4) and Y. Le Bouar (publications 2-3).

Contents

Chapter 1

Introduction

The urgent and necessary fight against climate change and its overarching consequences for nature and society are strongly connected to the human power generation and consumption. One of the most important challenges is the efficient electrical energy storage to allow the independent usage of fluctuating renewable energy or to increase the driving range and overall performance of electrical vehicles. In the last decades, lithium-ion batteries dominated and revolutionized the field of energy storage [1], where nowadays many electrical devices rely on this technology. Although electric car sales in Germany are currently and temporarily affected by a recession, the sales of electric cars worldwide are strongly increasing, where in 2022 14% of all new cars sold were electric, compared to less than 5% in 2020 [2]. It is expected that electric cars will contribute with about 20% to the total car sales in 2023 [2]. However, besides remarkable progress in electrode and electrolyte design, challenges like the safety behaviour or fast charging remains problematic [1] and presents a limitation in the overall transition towards a "greener" society. Crucial for efficient electric mobility are high performance battery systems with high energy densities, long lifetimes and driving ranges and the realistic possibility of fast charging at public charging stations. A promising solution for these issues are solid state batteries, which present several advantages and solve the problematic safety behaviour of battery systems with liquid electrolytes. Many car manufacturers started in the last years coorporations and investments in research and fabrication of solid state batteries for electric car applications, e.g Mercedes-Benz [3] or Toyota [4]. The performance and lifetime of solid state batteries is strongly connected to the used electrolyte and its mechanical properties. The mechanical properties play a crucial role regarding thermal expansion during operation, contact behaviour of the electrode-electrolyte interface or deflection of lithium dendrites

inside the electrolyte.

The microstructure of materials such as the solid electrolyte LLZO influences their properties, where especially, for solid state transformations, elastic effects can play a central role. Mismatch stresses between different phases or grains can influence the microstructure evolution and also the final equilibrated appearance, where ideally, tailoring of the microstructure leads to the desired parameters and behaviour. But how can the microstructure of a solid electrolyte be tailored and analyzed via simulations? This is a major challenge due to the multiple length and time scales, and a full and generic computational description has not yet been reached due to the complex interplay of physical effects on all scales. At this point the question arises whether new modeling and computational approaches may support the material modeling and potentially drastically accelerate the microstructure simulation of solid electrolytes.

Quantum computing is an emerging technology, which has the potential to boost demanding computations of multiscale phenomena in solid electrolytes. Instead of conventional data storage and handling, quantum computing uses qubits as basic entity, which requires a complete rethinking of algorithmic approaches. However, this general purpose machines suffer from insufficient number of qubits and system erros and decoherence, whose solution will take a long time despite promising progress in hardware and software research [5].

During the ongoing development of universal quantum computers the new field of adiabatic quantum computing developed in parallel, which is available under the name of quantum annealing. Here, machines with thousands of qubits and couplers are already today available. This technology has the potential to be competitive compared to conventional computing, leading to the ongoing debate about *quantum supremacy* of quantum annealing, i.e. if a quantum annealer is really superior to classical computing. Nevertheless, from a more applied perspective the important question is whether a specific problem formulation is possible for the quantum annealing topology.

Mechanical effects play a crucial part in the fabrication and operation of solid state batteries, where the development and application of suitable modeling approaches are highly desired for an efficient and accurate mechanical characterisation. Therefore, the aim of the present thesis is to develop methodical simulation concepts for quantum computing and their application in materials science. The underlaying framework is the solid electrolyte $Li_7La_3Zr_2O_{12}$ (LLZO) and its mechanical properties, which are computed either with classical and quantum tools and techniques.

1.1 Literature review

The inorganic oxide LLZO [6] still draws great attention in the scientific community due to its favourable characteristics as promising solid electrolyte in modern batteries. LLZO occurs in two different phases: the thermodynamically stable tetragonal phase and the desired cubic phase with high lithium ion conductivity, which is unstable at ambient temperatures. The tetragonal phase exhibits an ordered geometry with fully occupied atomic sites, while the cubic structure is disordered with partially filled sites [7], leading to questions about the mechanical behaviour and stability of the corresponding phases. Many experimental studies [7–16] investigate the mechanical and microstructural properties of the cubic phase via single substitutions with aluminium, gallium or tantalum, showing a successful stabilization of the cubic phase with increased ionic conductivity. Nonemacher et al. [14] prepared LLZO samples with different amounts of aluminium or tantalum and analyzed the microstructural and electrical properties, while ab initio simulations supported the mechanical investigations. Several other studies use ab initio simulations, e.g. for the analysis of lithium diffusion in tetragonal LLZO [17], the calculation of the lithium ion conductivity [18] and exploration of defective configurations [19–21] of pure and single doped LLZO and further density functional studies about the stability of cubic LLZO [22–24]. Yu et al. [25] investigated the elastic properties of single substituted LLZO with tantalum or aluminium by using DFT calculations and computed elastic constants. Overall, theoretical and experimental studies concerning co-substitutions in LLZO are related to the characterization of the ionic conductivity [26–29]. Important for the lifetime limitation of solid state batteries is the lithium dendrite growth inside the electrolyte, which can lead to the failure of the cell and is investigated in many studies [30–35]. In the context of dendrite propagation, the mechanical properties of the electrolyte are again of highest importance, because Fincher et al. [36] controlled the dendrite growth direction by applying an external stress. Additionally, McConohy et al. [37] confirmed that lithium intrusions form along microctructural defects inside the electrolyte, whose propagation direction can also be influenced mechanically.

Generally, the modeling and simulation of physical properties is an important part of materials science, where besides DFT calculations other methods are also of interest. Fourier transform methods are an efficient way to compute the elastic interactions between precipitates of bulk materials [38, 39], but the determination of the optimized microstructure on top of these calculations is much more demanding due to the characteristic long-ranged elastic interactions even for the simplest case of coherent interfaces and

vanishing elastic contrast between the phases. Additional challenges arise due to proximity of interfaces [40, 41], while phase field methods [42–45] are powerful, established tools, but suffer from the mentioned large simulation times. Indeed, machine learning methods are widespread in materials science [46–49], where these methods can also support DFT simulation workflows [50–53].

One of the most promising and powerful computation technologies is quantum computing, where research focus on several challenges, i.e. algorithm development [54, 55], error correction [56–59], quantum cryptography [60, 61] and quantum processor unit (QPU) architecture [62–65]. However, in the perspective of materials science, general purpose quantum computing applications are not yet widespread, while several studies focus on quantum annealing [66–70] as a technology that is already usable today. Quantum annealing allows highly efficient energy minimizations, however, applications in materials science [71–76] are still rare due to the specific binary quadratic problem formulation. A suitable material class are the shape memory alloys [77, 78], whose mapping to spin glass is subject of research [79–82]. Benchmarking of quantum annealing versus classical computations and performance tests [83–86] represent the dominating focus of recent research, while applications of quantum annealing in other research fields are also important [87–93]. Due to the probabilistic nature of the quantum annealing process, also solutions with higher energy are found, which allow the usage of the quantum annealer as a noisy Gibbs sampler [94, 95], where attention is paid to the sampling process [96–99].

1.2 Scope of the work

The general purpose of this work is the computation of mechanical properties and the microstructure modeling of the solid electrolyte $Li_7La_3Zr_2O_{12}$ (LLZO). First, the focus lies on co-substituted LLZO, where the influence of different tantalum and aluminium amounts on the structural and mechanical properties is investigated. The ab initio calculations for the cubic phase are performed via density functional theory (DFT) simulations, as implemented in the Vienna ab initio simulation package (VASP) [100], where a crucial step is the identification of energetically favourable substitution sites via prescreening methods. Via an electronic model, which bases on the computation of electrostatic interaction energies via Ewald summations, a machine learning assisted structure equilibration and preliminary Γ point simulations, the high precision structure is obtained and the three elastic constants of the cubic system are determined. The knowledge of these elastic constants allows the

computation of further mechanical properties, i.e. directional Young's modulus and shear modulus. Via the Zener ratio, the quantification of the system's anisotropy is performed and homogenization models enable the calculation of effectively isotropic, polycrystalline material properties, namely isotropic Young's modulus and Vicker's hardness. Leaving the electronic structure scale towards polycrystalline LLZO, a scale bridging description via the differential effective medium theory is necessary to adress the influence of pores on the effective Young's modulus.

To capture the microstructure equilibration with long-range elastic interactions, a novel, highly efficient computational approach is necessary. Therefore, a quantum annealing method is developed, which requires the formulation of the system's elastic energy in terms of an Ising Hamiltonian. Here, shape memory alloys, which exhibit structural phase transitions, can demonstrate the general, developed approach due to their successful mapping to spin glas descriptions. The one-dimensional model is used to benchmark the performance of the annealing process via comparison to classical algorithms, while for an extension to higher dimension the system is initially discretized to cuboidal grains. These grains can be in a cubic or tetragonal phase and homogeneous elasticity with Fourier transformation approaches is used to describe the elastic interactions between the grains. The quantum annealing runs are performed then on a D-Wave machine with Pegasus topology, while different transformation eigenstrains and the influence of boundary conditions on the resulting microstructures are investigated. The extension to irregular grain shapes by using a Voronoi tesselation and the introduction of random grain orientations lead to more realistic microstructures, which are analyzed under the influence of external strains.

This quantum annealing approach for the determination of realistic microstructures is further investigated regarding large scale simulations, the introduction of interfacial energies and the possibility of a cutoff for elastic energy calculations. Finally, the microstructure equilibration technique is applied to LLZO systems, whose mechanical properties are determined via the previous ab initio DFT simulations. Under inclusion of elastic and chemical energy contributions, the equilibrated phase distribution of cubic and tetragonal phases in LLZO are investigated.

So far all simulations via DFT and quantum annealing, besides DFT extrapolations, are performed at 0 K. Therefore, an additional novel quantum annealing approach is developed for an efficient Monte Carlo sampling at finite temperatures. The goal is to calculate physical properties, especially with high efficiency in the regime of low temperatures, where classical approaches show large statistical noise. Firstly, spin glasses and their low tem-

perature thermodynamics are investigated to illustrate the whole sampling process via the quantum annealer. An extension to larger systems occurs under consideration of the one-dimensional Ising model due to the availability of an analytical solution. Several different annealing settings and the influence of varying magnetic fields are analyzed before magnetization and heat capacity are calculated via the devloped quantum annealing sampling. Finally, the performance of the approach compared to classical Monte Carlo sampling is investigated.

Chapter 2

Theory & methods

2.1 Electrochemical energy storage

In our modern world, the storage of electrochemical energy is crucial regarding the fabrication of products, the usage of electronic devices or the powering of electrical vehicles. One of the most used battery systems for energy storage are lithium-ion batteries, which provide high energy densities, light weights and long lifetimes [101, 102]. Lithium-ion batteries are rechargeable battery systems, which nowadays mainly use liquid electrolytes, i.e. lithium salts dissolved in a liquid solvent. Besides the liquid electrolyte, lithium-ion batteries consist of a positive and a negative electrode, denoted as cathode and anode, and additionally a separator. The anode usually consists of carbon materials, while for the cathode several materials like the oxide $LiCoO_2$ or the inorganic compound $LiFePO_4$ are used [103]. The seperator is a thin porous membrane between both electrodes, whose primary function is the separation of the electrodes to prevent short circuits between them and enabling ion movement through the cell. Lithium ions Li^+ move during the charging process from the cathode through the separator and intercalate to the anode. Electrons move then from the cathode to the anode through the external circuit. The necessary electrical energy for the charging process is finally stored as chemical energy inside the cell. During discharging of the cell, reactions and processes are reversed and at the anode lithium ions Li^+ and electrons e^- are released through an oxidation half-reaction. Then, lithium ions move through the electrolyte to the cathode and react in a reduction half-reaction, while the electrons move to the cathode via the external circuit, leading to an useable electric current. The driving force for this lithium ion shuttling is the difference of chemical potentials between the electrodes.

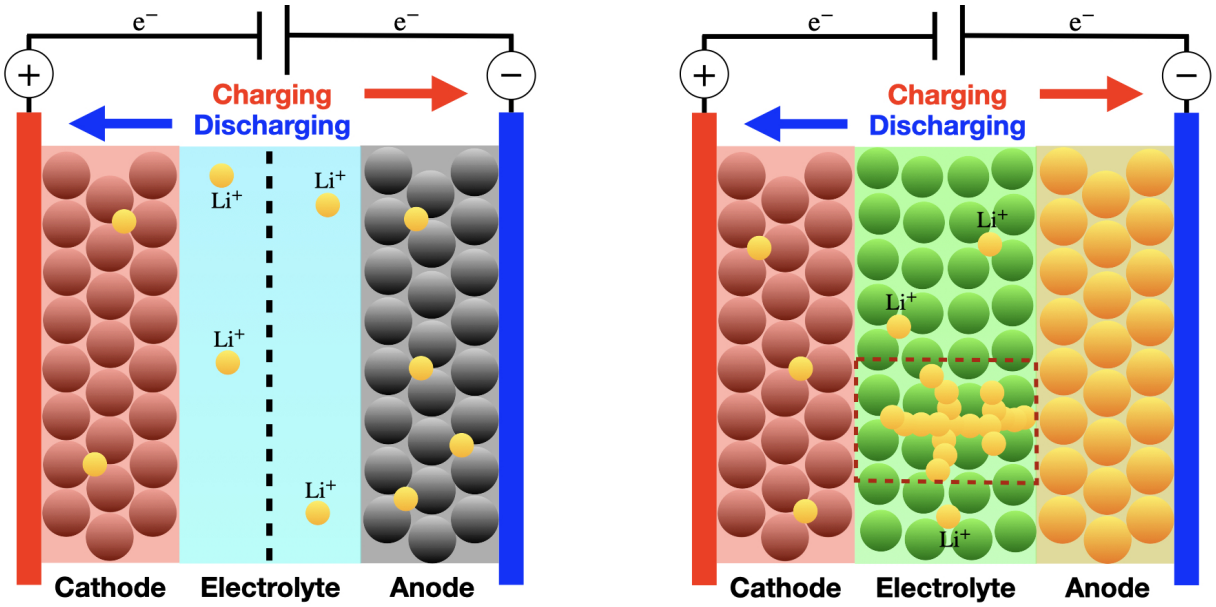

Figure 2.1: Schematic illustration of the two battery systems. Left: Lithium-ion battery with the electrodes and in between the liquid electrolyte. The blue and red bar represents the current collectors, which are attached to the electrodes and separate them from the external electronics. The yellow circles describe the lithium ions, whose moving direction depends on the charging (red arrow) and the discharging (blue arrow) process. Right: Solid state battery with solid electrolyte. Here, the highlighted area sketches possible lithium dendrite growth from the anode, through the electrolyte, towards the cathode.

However, besides the advantages of lithium ion batteries also downsides are present, i.e. safety aspects like leakage of the liquid electrolyte or the improper operation of the battery. Here, overcharging, low cell voltage during discharging or usage at temperature extremes can lead to overheating, short circuits and thermal runaways, which are extremely dangerous due to the usual high flammability of the electrolyte [103]. Another important topic is the ageing of lithium-ion batteries, which results in performance and capacity loss due to several chemical and physical processes, i.e. the degradation of anode and cathode, the deposition of metallic lithium on the anode surface, known as lithium plating [104], and the formation of an unstable, evolving solid electrolyte interphase (SEI) layer [105], which is formed by electrolyte decomposition products at the anode and can lead to an increased battery resistance. In order to overcome and solve these issues, solid state batteries are developed as promising battery systems for many applications and needs in daily life and science.

2.1.1 Solid state battery

A solid state battery consists of solid electrodes and a solid electrolyte and shows high potential for applications in electric vehicles and other commercial, portable electronics. The function of energy storage inside these batteries is comparable to lithium-ion batteries, but instead of an additional separator the solid electrolyte separates the electrodes and allows lithium ions to pass through. The cathode of the battery typically uses materials similar to those found in lithium-ion batteries, while the anode can consist of lithium metal. Solid state batteries exhibit differences in performance and stability to conventional lithium-ion batteries and can solve many problems like the problematic safety behaviour [106–108]. Due to the usage of a solid, nonflammable electrolyte instead of a liquid, the risk of leakage and combustion is reduced to a minimum. Regarding energy density, especially if lithium metal anodes are used [106, 109, 110], solid state batteries are also superior compared to lithium-ion batteries and can allow faster charging [1], what is highly desired in fast charging applications in electric vehicles. Overcoming issues like the formation of unstable SEI layers, solid state batteries can exhibit long lifetimes [109], however there are several challenges and problems to solve.

For fabrication and operation of solid state batteries, the solid battery components are exposed to deformations and stresses inside the cell, which can result in defects and a limited lifetime. Maintaining tight contact between the electrodes is crucial for optimal performance. However, this also results in high stresses within the battery components. During cycling of the cell, the electrodes are exposed to internal stresses due to temperature changes and the lithium ion intercalation, which lead to volume changes and high mechanical stresses within the solid electrolyte [111]. As a result, structural defects and especially micro-cracks are formed where preferentially lithium dendrites grow [15, 37], which shorten the lifetime of the battery further. Typically, failure and sudden degradation of this battery type are caused by lithium metal dendrite growth inside the electrolyte. These lithium metal intrusions [37], which are often but not necessarily tree-like, propagate through the electrolyte and connect the electrodes, leading to short circuits and premature defect of the cell. Additionally, at the anode side lithium plating on the electrolyte-electrode interface and inside the electrolyte along grain boundaries and pores creates high local stresses, which belong to the main reasons of battery failure [112]. Therefore, the mechanical behaviour, stability and characterization are important topics for the fabrication and operation of solid state batteries. Overall, the performance of the battery is strongly influenced by the used solid electrolyte and the cell's mechanical behaviour. Therefore, the choice of the

electrolyte material is a crucial step in the fabrication, where $Li_7La_3Zr_2O_{12}$ (LLZO) shows promising properties as solid electrolyte.

2.1.2 Solid electrolyte $Li_7La_3Zr_2O_{12}$

LLZO is an oxide, which is widely used as solid electrolyte material due to its high ionic conductivity and chemical stability in contact with lithium metal reactions [6, 108]. The garnet structured LLZO exhibits two different phases, namely a thermodynamically stable tetragonal phase with the lattice parameters $a = b \neq c$, which shows a poor ionic conductivity of about $10^{-6}\,\mathrm{S/cm}$ due to the disadvantageous distribution of lithium [7]. The other possible configuration is the cubic phase with the lattice parameters $a = b = c$, which is highly desired due to the high lithium-ion conductivity of about $10^{-4}\,\mathrm{S/cm}$ [7]. The reason for this difference is that the lithium ions bind to all available sites in the tetragonal phase and therefore the migration of lithium ions in the cubic phase is better due to more vacant ionic positions [7]. Raju et al. [7] state that an 8 per formula unit LLZO structure has 56 lithium ions, while the number of possible lithium ion positions is 56 in the tetragonal phase and 120 in the cubic phase. However, the cubic phase is unstable at ambient temperatures with a typical transition temperature of $450 - 1000\,\mathrm{K}$ [7], but substitutions of different aliovalent chemical elements allow the stabilization of the cubic phase. Here, Ta^{5+}, Al^{3+} and Ga^{3+} are suitable candidates for substitutions [8, 113]. In general, substitutions affect the structural composition via volume changes of the unit cell, the access of migration pathways and the configurational changes of binding sites [114]. To avoid possible negative effects by substitutions, the combined substitutions are suitable to avoid the blocking effect of aluminium (Al), which decreases the ionic conductivity by blocking lithium ion pathways [26, 115]. Aluminium therefore stabilizes the cubic phase, but the gained higher ionic conductivity is directly lost. Tantalum (Ta) substitutions show a beneficial lithium ion conductivity of the electrolyte [116]. However, besides the stabilizing effect of Ta, a doping with this element increases the material's costs drastically [14], where the combined doping of Al and Ta stabilizes the cubic phase efficiently under avoidance of the mentioned element's downsides [26]. In order to have a solid state battery with high performance, the solid electrolyte and also its doped variants play a crucial role, where mechanical effects strongly influence the lifetime of the cell.

2.2 Continuum mechanics

2.2.1 Linear elasticity

In this work multi-grain setups and combined substituted solid electrolytes are described via the theory of linear elasticity, which in general assume solids as continuous bodies. Applied forces on the solids lead to deformations, resulting in changes of volume and shape of the body. Here, only elastic deformations are considered, i.e. any displacements are reversible. Any point in the body is described by a vector $\mathbf{r}$, while a deformation displaces all points, leading to a different vector $\mathbf{r}'$ [117]. The displacement is then defined as the difference between these vectors

$$u_i = x_i' - x_i \,, \tag{2.1}$$

with components x_i of vector $\mathbf{r}$ and x_i' of vector $\mathbf{r}'$. In the framework of linear elasticity, i.e. only small deformations are considered, the change in a length element under deformation is defined via the strain tensor [118]

$$\epsilon_{ij} = \frac{1}{2}\left(\frac{\partial u_i}{\partial x_j} + \frac{\partial u_j}{\partial x_i}\right), \tag{2.2}$$

which is symmetric $\epsilon_{ij} = \epsilon_{ji}$. An undeformed body is in mechanical equilibrium, therefore the forces on this body vanish. However, under deformation the arrangement inside the body is changed and internal forces arise, which tend to recover the equilibrium configuration. These forces are called internal stresses and are described via the stress tensor σ_{ij} (dimension: force per area), which is also symmetric $\sigma_{ij} = \sigma_{ji}$. For linear elasticity with small deformations, the strain is proportional to the applied stress, and this relation is given by *Hooke's law*

$$\sigma_{ij} = C_{ijkl}\, \epsilon_{kl} \,, \tag{2.3}$$

with the fourth-rank elasticity tensor C_{ijkl}, which connects strain and stress. In Cartesian coordinates strain and stress tensor have each nine components and therefore the elasticity tensor has 81 components, whose number can be reduced due to symmetry considerations to less then 21 independent components [118]. For isotropic systems, i.e. independence of direction in space for the properties, Hooke's law is given by

$$\sigma_{ij} = \lambda \epsilon_{kk} \delta_{ij} + 2\mu \epsilon_{ij} \,, \tag{2.4}$$

with the first Lamé coefficient λ and shear modulus μ. Note that Einstein's sum convention is used here. The internal stresses balance each other out in equilibrium and therefore the equations of equilibrium of a deformed body are [118]

$$\frac{\partial \sigma_{ij}}{\partial x_j} = 0. \tag{2.5}$$

The elastic energy density can be calculated via [118, 119]

$$f = \frac{1}{2}\sigma_{ij}\epsilon_{ij} = \frac{1}{2}\lambda\epsilon_{kk}^2 + \mu\epsilon_{ij}^2\,, \tag{2.6}$$

which depends on the strain tensor quadratically.

2.2.2 Eigenstrain

The picture of this strain concept can be expanded by the term *eigenstrain* [120], which describes the inelastic strain of a material caused by effects like thermal expansion, phase transformations or crystallographic inclusions. These eigenstrains cause internal stresses inside the material, which are called eigenstresses and are independent of any external applied force. In the case of infinitesimal deformations, the total strain ϵ_{ij} is considered as the sum of the elastic strain $\epsilon_{ij}^{\mathrm{el}}$ and the eigenstrain $\epsilon_{ij}^{(0)}$ [121]

$$\epsilon_{ij} = \epsilon_{ij}^{\mathrm{el}} + \epsilon_{ij}^{(0)}. \tag{2.7}$$

Then, the isotropic Hooke's law with elastic strain $\epsilon_{ij}^{\mathrm{el}} = \epsilon_{ij} - \epsilon_{ij}^{(0)}$ is given by

$$\sigma_{ij} = \lambda\left(\epsilon_{kk} - \epsilon_{kk}^{(0)}\right)\delta_{ij} + 2\mu\left(\epsilon_{ij} - \epsilon_{ij}^{(0)}\right). \tag{2.8}$$

The integration of the elastic energy density with elastic strain (eq. (2.6)) leads to the elastic energy for isotropic materials

$$E_{\mathrm{el}} = \int_V \left(\frac{\lambda}{2}\left(\epsilon_{kk}(\mathbf{r}) - \epsilon_{kk}^{(0)}(\mathbf{r})\right)^2 + \mu\left(\epsilon_{ij}(\mathbf{r}) - \epsilon_{ij}^{(0)}(\mathbf{r})\right)^2\right)\mathrm{d}\mathbf{r}. \tag{2.9}$$

2.2.3 Inclusions

Many materials are inhomogeneous and consist of different phases and multiple grains. A specific case is a single inclusion inside a large medium. In particular, the elastic energy

of inclusions with a strain mismatch inside an isotropic body can be considered, where the elastic moduli for inclusions and body are the same. J.D. Eshelby considered ellipsoidal inclusions with general eigenstrains and found a solution, which states that strain and stress fields inside the inclusion are uniform [121, 122]. For homogeneous elasticity tensor and external stress, there is only a dependence between the external, potential energy and the inclusion's volume [123, 124], which is generalized in the *Bitter-Crum theorem*. This theorem states that if in addition the eigenstrain is purely isotropic and dilatational, the total elastic energy depends only on the volume fraction of the inclusions and not on their shape, position, number or size [124].

2.3 Density functional theory

In the present work solid electrolyte's mechanical properties are calculated via *ab initio* computations, i.e. only using nature's laws and constants. These calculations and simulations are based on the *density functional theory* (DFT), which allows quantum mechanical descriptions for atomic and molecular systems with reasonable computational demand. The overall goal is to solve the time-independent Schrödinger equation

$$\hat{H}\Psi = E\Psi, \tag{2.10}$$

with complex wave function Ψ, Hamiltonian operator $\hat{H}$ and system's total energy E. Solids usually contain several thousands of electrons and nuclei, which are strongly coupled due to Coloumb forces. Therefore, the corresponding wave functions are high-dimensional and the complexity of the describing Schrödinger equation increases enormously. To simplify the description, the first assumption is the *Born-Oppenheimer approximation* [125], which states that the nuclei are fixed in space and corresponding motions of electrons and nuclei are treated separately due to the significant mass differences. This leads to the separation of electronic and nuclear contributions in the Schrödinger equation. Then, the many-body Hamiltonian of a N-electron system is given by

$$\hat{H} = \sum_{i}^{N}\left(-\frac{\hbar^2}{2m_i}\nabla_i^2\right) + \frac{1}{2}\sum_{i\neq j}^{N}\frac{e^2}{|\mathbf{r}_i - \mathbf{r}_j|} + \sum_{i}^{N} V_{\text{ext}}(\mathbf{r}_i), \tag{2.11}$$

where the first term describes the kinetic energy, the second term characterises the Coulomb interaction between the electrons and $V_{\text{ext}}(\mathbf{r}_i)$ presents the external potential arrising from

the electron-nuclei interaction.

2.3.1 Hohenberg-Kohn theorems & Kohn-Sham equations

Solving this time-independent Schrödinger equation of a N-electron system is highly computationally demanding, because the wave function has to be calculated for N interacting electrons with $3N$ coordinates. Here, the DFT allows the system's transformation to an electron-density-dependent problem [126] and therefore reducing the formulation's complexity, i.e. the electron density only depends on three spatial coordinates. The theoretical background of the interplay between wave functions, Hamiltonian, external potential $V_{\text{ext}}(\mathbf{r}_i)$ and electron density is given by the *Hohenberg-Kohn theorems* [127]. The first theorem states that the external potential $V_{\text{ext}}(\mathbf{r}_i)$ of the many-body problem is a unique functional of the ground state's electron density. This implies that the knowledge about the ground state's electron density allows the calculation of the corresponding external potential and thus the wave function. Therefore, this inversion is in contrast to the general way of computing the electron density from the wave function, which is determined by solving the Schrödinger equation with known Hamiltonian and included external potential. The system's energy is then written as a functional of the electron density $\rho(\mathbf{r})$ [126]

$$E[\rho(\mathbf{r})] = F[\rho(\mathbf{r})] + \int V_{\text{ext}}(\mathbf{r})\rho(\mathbf{r})\,\mathrm{d}\mathbf{r}, \tag{2.12}$$

with the universal functional $F[\rho(\mathbf{r})] = T[\rho(\mathbf{r})] + U[\rho(\mathbf{r})]$ consisting of the electronic, kinetic energy operator $T[\rho(\mathbf{r})]$ and the electron-electron interaction functional $U[\rho(\mathbf{r})]$. This universal functional is independent of the external potential and therefore the connection between external potential and electron density is unique.

The second Hohenberg-Kohn theorem states that the energy minimizing electron density of the system is the ground state electron density ρ_0. This ground state energy can then be determined via the variational principle with $E[\rho(\mathbf{r})] \geq E_0[\rho_0(\mathbf{r})]$. Therefore, the application of the Hohenberg-Kohn theorems allows a different formulation, where the $3N$ dimensional wave function is replaced with the electron density, resulting in a three variable problem. However, solving the resulting Kohn-Sham equations is still computational demanding due to the unknown universal functional $F[\rho(\mathbf{r})]$, consisting of N coupled electron interactions.

Kohn and Sham [128] solved this problem by mapping the N electron system to an non-interacting one-electron system, where the electronic interactions are expressed through an

effective potential V_{eff}. The corresponding Kohn-Sham Hamiltonian is given by

$$\hat{H}_{\text{KS}} = -\frac{\hbar^2}{2m}\nabla^2 + V_{\text{H}}[\rho](\mathbf{r}) + V_{\text{ext}}[\rho](\mathbf{r}) + V_{\text{xc}}[\rho](\mathbf{r}) = -\frac{\hbar^2}{2m}\nabla^2 + V_{\text{eff}}[\rho](\mathbf{r}), \tag{2.13}$$

with the noninteracting kinetic energy and the Hartree potential $V_{\text{H}}[\rho](\mathbf{r}) = \int \frac{e^2\rho(\mathbf{r'})}{|\mathbf{r}-\mathbf{r'}|}\,\mathrm{d}\mathbf{r'}$ describing the interaction between one electron at $\mathbf{r}$ and the mean electron density at $\mathbf{r'}$. $V_{\text{ext}}[\rho](\mathbf{r})$ presents again the external potential from the electron-nuclei interaction and the contribution $V_{\text{xc}}[\rho](\mathbf{r})$ describes the correlation and exchange between electrons and therefore quantum mechanical many-body effects. The computation of the kinetic energy, the Hartree energy and the external energy is unproblematic, however the exchange-correlation potential $V_{\text{xc}}[\rho](\mathbf{r})$ is unknown and is determined via approximations.

The *local density approximation* (LDA) assumes local dependence of the exchange-correlation potential $V_{\text{xc}}[\rho](\mathbf{r})$ on a uniform electron density and on the energy per electron of an homogeneous electron gas. The system is approximated as locally homogeneous, where at each point of space a uniform electron density is assigned, leading to following expression

$$V_{\text{xc}}^{\text{LDA}}[\rho(\mathbf{r})] = \int \rho(\mathbf{r})\epsilon_{\text{xc}}^{\text{hom}}[\rho(\mathbf{r})]\,\mathrm{d}\mathbf{r}, \tag{2.14}$$

with exchange and correlation energies per electron $\epsilon_{\text{xc}}^{\text{hom}} = \epsilon_{\text{x}}^{\text{hom}} + \epsilon_{\text{c}}^{\text{hom}}$ of the homogeneous electron gas. This approximation achieves good results for systems with slowly varying electron densities and no large gradients, e.g. simple metals. However, the LDA underestimates lattice parameters and therefore overestimates mechanical parameters like bulk modulus [126].

In order to describe inhomogeneous systems with varying electron densities, the *generalized gradient approximation* (GGA) is used to determine the exchange-correlation potential by including the gradient of the electron density $\nabla\rho(\mathbf{r})$. The GGA is suitable for almost all systems and leads to an accurate computation of the exchange-correlation potential. One of the most famous GGA formulations is the improved functional by Perdew- Burke and Ernzerhof (PBE) [129].

Finally, these approximations allow the calculation of the effective potential V_{eff}, leading to the *Kohn-Sham equations*

$$\left(-\frac{\hbar^2}{2m}\nabla^2 + V_{\text{eff}}[\rho](\mathbf{r})\right)\phi_i(\mathbf{r}) = \epsilon_i\phi_i(\mathbf{r}), \tag{2.15}$$

with energy ϵ_i and Kohn-Sham orbitals $\phi_i(\mathbf{r})$, which define the electron density via $\rho(\mathbf{r}) =$

$\sum_i |\phi_i(\mathbf{r})|^2$ [128]. This eigenvalue equation is solved in an iterative self-consistent procedure, which involves an electronic and ionic minimization for the electron density. Starting point is the estimation of an initial electron density and the solution of the Kohn-Sham equations via diagonalization. The resulting new electron density is then used as the initial input, until the change of the electron density or the total energy fulfills certain criteria and leads to a stopping of the electronic loop. Then, the forces of the system are calculated and the ionic positions are updated and the electronic iterations start again. The whole procedure is stopped, if the thresholds for the electronic and ionic minimizations are reached and the ground state electron density is determined, leading to the computation of the total energy and further physical properties of the system.

2.3.2 Treatment of solids

The treatment of solids requires the consideration of an almost infinite number of electrons and atoms and therefore further simplifications are necessary like the introduction of a *pseudopotential*, which approximates the complicated motion effects of core electrons by a simpler potential with fewer nodes in the resulting pseudo-wavefunctions [126].

Additionally, the periodically arrangement in solids can be exploited by reformulating the wave function. According to the *Bloch theorem* [130] the wave function is expressed as

$$\Psi_k(\mathbf{r}) = \exp(i\mathbf{kr}) \cdot u_k(\mathbf{r}), \tag{2.16}$$

with a periodic function $u_k(\mathbf{r})$, which has the same periodicity as the crystal lattice such that $u_k(\mathbf{r}) = u_k(\mathbf{r} + \mathbf{R})$. The real lattice vector is defined by $\mathbf{R} = n_1\mathbf{a}_1 + n_2\mathbf{a}_2 + n_3\mathbf{a}_3$ with unit cell vectors $\mathbf{a}_i$ and integer numbers n_i. The periodic function is given under Fourier expansion as

$$u_k(\mathbf{r}) = \sum_{\mathbf{G}} c_k(\mathbf{G}) \cdot \exp(i\mathbf{Gr}), \tag{2.17}$$

with Fourier coefficients $c_k(\mathbf{G})$ and the reciprocal lattice vector $\mathbf{G}$. This leads to the wave function

$$\Psi_k(\mathbf{r}) = \sum_{\mathbf{G}} c_k(\mathbf{k} + \mathbf{G}) \cdot \exp(i(\mathbf{k} + \mathbf{G})\mathbf{r}), \tag{2.18}$$

meaning that the wave function is expressed by the superposition of plane waves. Therefore, it is sufficient to consider only a small part of the periodic solid for accurate DFT calculations, i.e. specific $\mathbf{k}$-vectors from the first Brillouin zone. Additionally, an energy

cutoff is introduced to reduce the maximum set of plane waves due to the fact that low energy plane waves contribute the strongest to the total energy in the search for the ground state energy. The energy cutoff is given by [126]

$$E_{\text{cutoff}} \geq \frac{\hbar^2}{2m}|\mathbf{k}+\mathbf{G}|^2, \tag{2.19}$$

where the specific value of E_{cutoff} is system dependent and the convergence of the DFT results has to be checked carefully.

2.4 Quantum computing

Classical computing stores information in bits, which are either in state 0 or 1, and performs computations via arrangements of logic gates. Quantum computing on the other hand uses for information storage so called *qubits*, which identify again these two states but also their superposition. A quantum state of a qubit $|\psi\rangle$ can be written as the linear combination of two basis states $\{|0\rangle, |1\rangle\}$

$$|\psi\rangle = \alpha|0\rangle + \beta|1\rangle, \tag{2.20}$$

with complex amplitudes α and β, which obey the normalization condition $|\alpha|^2 + |\beta|^2 = 1$. All superposition states are handled simultaneously in computations, what leads to quantum parallelism, which can accelerate computations drastically compared to classical operations. A measurement on a quantum system leads to the collapse of the wave function to one possible eigenstate. This occurs as a probabilistic process, which is in contrast to the deterministic, classical computations.

Furthermore, different qubits can be coupled and form mixed states, where this principle is known as *entanglement*. These states cannot be described independently of each other and therefore can be considered as a single object with multiple, possible states, ensuring the computational power of quantum computing. Considering two quantum systems a and b, states, which can be formulated as products of pure states

$$|\psi\rangle = |\psi\rangle_a \otimes |\psi\rangle_b, \tag{2.21}$$

with tensor product $\otimes$ are called separable. If this formulation as combination of product

states is not possible, the states are entangled, e.g. a Bell state [131] of a two-qubit system

$$|\Psi^+\rangle = \frac{1}{\sqrt{2}} \left(|0\rangle_a|1\rangle_b + |1\rangle_a|0\rangle_b\right). \tag{2.22}$$

In quantum computing these entangled Bell states can be created via quantum circuits, consisting of a Hadamard gate, which maps to superposition states, and a CNOT gate for the transformation of quantum states. Further quantum gates allow the construction of quantum circuits, which lead to the implementation of quantum algorithms like Shor's algorithm for the factoring of prime numbers or Grover's search algorithm for unstructured databases [131]. These algorithms could beat the performance of the classical counterparts easily, however, general purpose quantum computers with a reasonable number of qubits and error control are not available yet.

2.4.1 Quantum annealing

While the quantum computer's sizes grow and better error control and corrections are invented, a technology named as *quantum annealing* has been developed and has already today the potential to be competetive compared to classical machines. Quantum annealing belongs to the class of adiabatic quantum computing and is commercially available with over 5000 qubits arranged on a lattice. The quantum annealing process is used to solve discrete optimization problems and to sample from low-energy states. Qubits store and process information and are realized via superconducting loops, where the direction of a circulating current inside a loop defines different spin states [132]. The interaction of each qubit with external flux biases allows the construction of an energy landscape with variable barrier height and energy difference [132]. The computation starts with the initialization of the system in the ground state of the known Hamiltonian

$$H_0 \sim -\sum_i \sigma_i^x, \tag{2.23}$$

with Pauli matrices σ_i, i.e. a strong transverse magnetic field [133, 134]. This Hamiltonian is turned during the quantum annealing process into the desired Hamiltonian, which is based on an Ising model [135]

$$H_p = \sum_i h_i s_i + \sum_{i<j} J_{ij} s_i s_j \,, \tag{2.24}$$

with spin states $s_i = \pm 1$, bias h_i and coupling strength J_{ij} between qubits i and j. The Ising model describes a discrete magnetic model with spins, which are arranged on a lattice and interact ferromagnetically or antiferromagnetically with their neighbors. With this model it is possible to identify phase transitions and it is widely used in statistical mechanics, where the general case with arbitrary couplings h_i and J_{ij} is called *spin glass*. Another widely used formulation is the *quadratic unconstrained binary optimization* (QUBO)

$$E(x) = \sum_{i \leqslant j} x_i Q_{ij} x_j \,, \tag{2.25}$$

with binary variables $x_i \in \{0, 1\}$ and upper triangular matrix of real weights Q_{ij}. The QUBO and Ising formulations are computationally equivalent and can be transformed into each other via the relation $x_i = \frac{s_i+1}{2}$ between the binary variables.

The goal during the annealing process is to find the energetic minimum of this Ising Hamiltonian $\min_{\{s_i=\pm 1\}} H_p$. The annealing process follows the time dependence [136]

$$H(s) = \frac{1}{2} A(s) H_0 + \frac{1}{2} B(s) H_p \,, \tag{2.26}$$

with annealing evolution functions $A(s)$ and $B(s)$ and normalized anneal parameter $s \in [0, 1]$. The initial, known ground state is given for $s = 0$, $A(0) \gg B(0)$, while for $s = 1$, $A(1) \ll B(1)$, the desired problem Hamiltonian is present [137]. The normalized anneal parameter s increases linearly for the standard annealing schedule, while the incorporation of quenches and pauses inside this curve influences the resulting energy states, i.e. it comes to an intermediate freezing of the system at excited energy states [138]. This variation of the annealing schedule is beneficial for the sampling of the quantum Boltzmann distribution, where then more excited energy states are considered with performance advantages for increasing system sizes compared to classical approaches [138]. Another schedule type is the reverse annealing, which initialize the qubits in a classical state as a starting point for a local minima search [139]. Both Hamiltonians H_0 and H_p do not commute [135], and the time of the transition of the initial Hamiltonian to adopt the low energy state is sufficiently large. This is important for the validity of the adiabatic theorem of quantum mechanics [140], which states that a system remains in its eigenstate, if changes occur adiabatically. Additionally, quantum annealing uses tunneling to leave metastable regions and entanglement to create entangled states inside the quantum annealing processor (QPU) [141].

Due to the probabilistic nature of the QA process and imperfections of the machines, the lowest energy state is not always found, especially if close low energy states exist. Therefore, a suitable number of repetitions is made and the annealing process is repeated according to a given number of reads to identify the configuration with the lowest detected energy. Another possibillity to overcome technical machine's biases is to use spin flip reversals, which improve the sampling and the solution's quality further by automatically transforming the couplings according to $J_{ij} \rightarrow J_{ij} g_i g_j$ and $h_i \rightarrow h_i g_i$ with random gauges $g_i \in \{-1, +1\}$ [142]. This inversion of spins leaves the physical problem invariant. In order to initialize a problem on the QPU, the *minor embedding* is used to generate a subgraph of coupled qubits, so called chains, to cover one variable of the problem [143, 144]. These chains are weighted and constrained according to a chain strength term to ensure that each subgraph of coupled qubits returns the same value. If the chain strength is not large enough, the subgraphs will result in different values at the end of the annealing and so called *chain breaks* occur, which lead to non-optimal outcomes. If the QPU's architecture is still not fitting, hybrid quantum annealing is useful for huge systems, using the interplay between classical algorithmus and quantum annealing in areas of high computational complexity [136, 143].

2.4.2 Optimization & sampling

An important part of current quantum computing is the benchmarking against classical algorithms. The situation in research regarding quantum supremacy is still a hot and ongoing topic and a lot depends on the different problem classes and modified and improved classical algorithms [83–86].

The simplest approach for the minimization of a N spin system is the brute force approach, for which all 2^N possible configurations are computed and the solution with the lowest energy is selected. Iterations over all spin configurations are extremely computational demanding, but result in the true ground state of the system. This deterministic approach scales with $\sim \mathcal{O}(2^N)$.

Simulated annealing [145] is a probabilistic approach, which starts with a random initial spin configuration. In each iteration a new configuration is generated by a single spin flip, which is accepted if its energy is lower than the previous configuration. However, if the energy difference between new and old spin system ΔE is positive, the configuration is not directly denied. The acceptance of the candidate configuration depends on the probability given by the Boltzmann factor $\exp(-\Delta E/T)$ with temperature T. The idea

is to avoid being stuck in local energy minima and to enable the approximation of the global minima. This is similar to quantum annealing, which employs tunneling to leave metastable regions [66]. The temperature T is reduced during the simulation according to specific cooling schedules, leading to higher sensitivity to subtle energy variations and finally convergence towards an energetic minimum. The optimization of the simulation's stopping criteria and the used cooling strategie is a crucial step. Besides a simple linear cooling, there exists several alternatives, e.g. exponential or logarithmic schedules [146]. Simulated annealing is a time-consuming approach due to the optimization of algorithm parameters to avoid being caught in high energy local minima, however, the results are often very promising [147].

Monte Carlo methods are statistical techniques, which are based on random sampling and the Boltzmann factor $\exp(-\Delta E/T)$. They are used mainly for numerical integration, optimization problems and importance sampling. The Metropolis Monte Carlo algorithm [148] generates random samples from a probability distribution and is equivalent to the simulated annealing algorithm for constant temperature. These sequences of samples are *Markov chains*, which are only dependent on the previous configurations. Further physical quantities can be computed via the obtained random samples, i.e. the estimated expectation value of an observable $A(x)$ is defined as

$$\langle A \rangle = \sum_{i=1}^{N} P(x)A(x), \tag{2.27}$$

with Boltzmann probability

$$P(x) = \exp(-\beta E(x))/Z. \tag{2.28}$$

Here, $\beta = 1/kT$ and the canonical partition function is given by $Z = \sum_{i=1}^{N} \exp(-\beta E(x))$.

2.5 Artificial neural networks

Machine learning (ML) is an important part of artificial intelligence. ML algorithms allow an efficient analysis of huge data sets and are able to accelerate computations significantly in many interdiciplinary fields of research and daily life. Here, the processing of data is differentiated in several categories: (i) The *supervised learning* where input and desired output values are given with the goal to predict output from new data. (ii) The *unsupervised learning* which tries to find structure and patterns in unlabeled data, and (iii) the

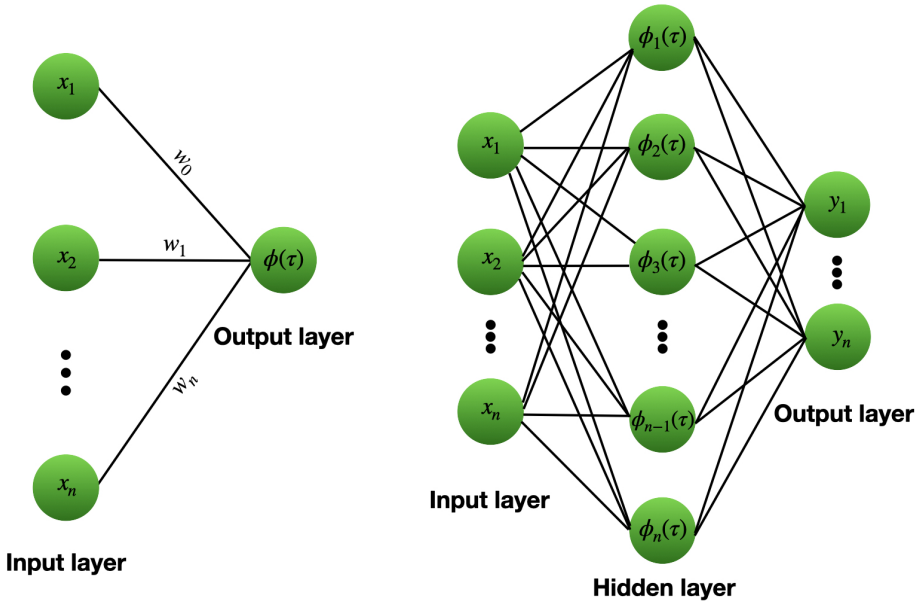

Figure 2.2: Sketch of two fully connected ANNS. Left: single-layered perceptron with inputs x_i, weights w_i and output $y = \phi(\tau)$. Right: multilayered perceptron with one additional hidden layer. Both ANNs are feedforward neural networks.

reinforcement learning whose idea is to control the learning process via positive or negative feedback. However, also the combination of (i) and (ii) exist, i.e. the *semi-supervised learning* where labled and unlabled data sets are analysed.

A widely used ML method are *artificial neural networks* (ANNs), which allow to tackle prediction, recognition and classification tasks [149]. ANNs are inspired by the human brain and its biological neural network, consisting of several layers and nodes as artificial neurons. Like the biological counterparts, the neurons are connected, receive signals from other neurons and also send them, if a certain activation threshold is triggered. The *perceptron* [150] is a simple ANN algorithm for supervised learning and also the basis of modern ANNs. It was published 1957 by F. Rosenblatt and consists of one input layer of artificial neurons, which also represents the output layer. The neurons act like a linear regression model, where each input is weighted separately to control the importance and afterwards the inputs are summed according to [151]

$$\tau = \sum_{i=1}^{n} w_i x_i + b\,, \tag{2.29}$$

with weights w_i, inputs x_i and bias b, which represents an additional control parameter for the learning process. The output y is then given by the activation function $y = \phi(\tau)$, which mimicks biological neurons with their activation threshold. There are several possible activation functions depending on the architecture of the ANN and the specific problem to solve. Typical functions are the non-linear heaviside step function or the linear function $y = x$. Finally, the resulting output y_i is compared with the desired output $\hat{y}_i$ and in each learning iteration the weights and bias of the neurons are adjusted according to [151]

$$w_{i,\text{new}} = w_{i,\text{old}} + \alpha(\hat{y}_i - y_i)x_i \,, \tag{2.30}$$

until the difference between calculated and desired output is minimized. Here, the hyperparameter α describes the learning rate, whose reasonable choice is essential for the learning process.

The complexity of the perceptron can be increased via the inclusion of more neuron layers. The multilayer perceptron consists of an input layer, several hidden layers for the processing and transformations of the input data and an output layer. There are two general types of information flow in multilayer ANNs: the *feedforward neural networks* with an information flow in one direction, i.e. from the input layer through the hidden layers to the output layer, and *recurrent neural networks*, whose information flow occurs also in the back direction and connects input and output of neurons.

Chapter 3

Summary & discussion

The goal of this work is the determination of mechanical properties and the microstructure modeling of the solid electrolyte $Li_7La_3Zr_2O_{12}$ (LLZO). Different simulation techniques and modeling approaches were successfully developed and used to characterize LLZO extensive and to extend the research field of materials science by new, highly efficient modeling methods. In this work the whole range of the electronic scale, over the inclusion of pores, up to the macroscopic level with thousands of grains is covered.

First, ab initio DFT simulations of the cubic phase under Ta and Al substitutions are performed to investigate the influence of substitutions on the structural and mechanical properties. Due to the large set of possible lithium substitution sites, an electronic model based on the electrostatic energy is used to determine energetically suitable lithium positions for substitution. The computational demand of this prescreening workflow can be reduced with an ANN, which predicts directly the equilibrium coordinates of the ions. This ML approach can be very helpful in the context of unit cells with high numbers of different atoms, where the prediction of equilibrated structures reduces the necessary number of simulations. To make the ANN more accurate for substitutions levels, which deviate strongly from the training data, the training dataset can be extended and the direct prediction of further physical quantities is subject of future research. Preliminary ab initio simulations at the Γ point lead to the final high precision structure for productive calculations, where the prescreening approaches increase the efficiency and accuracy of the computations.

The knowledge of the three elastic constants allows the calculation of the directional properties of Young's modulus and shear modulus, where slightly divergent values for the different directions are found. This indicates an anisotropy, which is also confirmed by the Zener ratio, however, the Zener value ranges in the magnitude of other isotropic oxides,

what leads to the conclusion that the elastic properties of isotropic polycrystalline LLZO will not deviate much from the averaged results. The resulting mechanical properties are determined for a wide range of substitution levels, where the resulting lattice constants show a clear Ta substitution dependence. The decreasing lattice constants of systems with high Ta level is expected due to the smaller ionic Ta radius compared to the substituted Zr, however, the variations of the lattice constants are small ($< 0.1\,\text{Å}$). The resulting Young's modulus decreases with increasing Al level, where the variations of values are also small and overall the Young's moduli are comparable to the tetragonal LLZO phase. These results are again found in the calculated hardness, which shows only a weak dependence on substitutions and results in values close to the unsubstituted structure. Therefore, the co-substitutions preserve the structural and mechanical properties of LLZO. This presents an important contribution regarding the stabilization of cubic LLZO and the fabrication of batteries using this solid electrolyte.

The DFT calculations do not capture the fact that LLZO is a porous material, whose pores influence the mechanical properties. A scale bridging description via a differential effective medium theory approach between the electronic scale and the larger scale of pores is expected to be accurate with measured effective elastic constants for low pore concentrations. The typical porosity of LLZO is of the order of 10 % and leads to an expected decay of 27 % for Young's modulus, where different values of Poisson ratio ν do not influence the elastic modulus decrease. The comparison and validation of the calculated Young's modulus values with single Ta substituted experimental results shows a good agreement, where the computed and experimental values only differ by a few GPa. Therefore, this model can be used for consistency checks of theoretical and experimental results. Generally, the inclusion of pores via the differential medium theory enables an effective and accurate description for application relevant solid electrolytes. Together with the DFT calculated mechanical properties of co-substituted LLZO, the mechanical behaviour of the solid electrolyte is precisely characterized, leading to potential material optimizations regarding the mechanical suppression of dendrites and other mechanical based issues during the operation of batteries (publication 1).

In order to compute the microstructure equilibration with long-range elastic interactions, a novel quantum annealing method is developed. First, the general approach, where the elastic interactions between coherent grains of different phases, orientations or variants are considered, is illustrated in a one-dimensional Ising formulation. The goal of the quantum annealing method is to minimize the elastic energy and to find the optimal variant

configuration. For benchmarking and performance tests, the approach is compared to classical, numerical techniques, where the brute force approach shows the highest computation time and even small system sizes ($N \approx 40$) are too large for reasonable computations. The simulated annealing algorithm produces good result, whereas pure quantum annealing is by far the fastest method to solve optimization problems and represents an almost constant elapsed QPU access time with about three orders of magnitude faster computation times. However, beyond around $N = 50$ spins chain breaks occur occasionally and can influence the resulting microstructure. Therefore, hybrid quantum annealing is used, which leads to a slightly increased computation time compared to pure QA, allowing the calculation of system sizes of 10^3 grains with an almost constant timing. Thus, hybrid quantum annealing is the fastest approach for large system sizes and outperforms the compared classical algorithms easily.

For transformations in higher dimensions, the system is discretized into small cuboidal grains, whose elastic energy is determined via the usage of homogeneous elasticity, which reduces the problem formulation to pairwise interactions as demanded by the necessary binary quadratic description of QA machines. Fourier transformation approaches are exploited to compute distance and orientation dependent interactions between grains and two different eigenstrains are introduced, leading to different resulting microstructure patterns. Here, the calculation of the $\mathcal{O}(N^2)$ elastic energy interactions dominates the total computing time, where the $\mathcal{O}(2^N)$ possible grain configurations are optimized via QA in negligible times. The resulting microstructures depend on the used boundary conditions, i.e. for shear eigenstrain energetically equivalent stripe patterns with nonuniform widths are obtained, while for tetragonal eigenstrains single variants ($\langle \sigma_{ij} \rangle = 0$) or regular inclined stripes ($\langle \epsilon_{ij} \rangle = 0$) are found. These inclined stripes have an inclination angle $\phi \approx 33°$ corresponding to a detailed analysis, which reveals the influence of the granular structure and antialiasing effects on the inclination angle.

In order to bridge the gap towards realistic microstructures, the grains are generated according to a Voronoi tesselation and external strains are applied, which lead to the appearance of a magnetic term in the Ising formulation. The resulting microstructures with tetragonal eigenstrain show similiar characteristics as before, where now the increasingly applied external strain favors the selection of just one variant. Additionally, random grain rotations are introduced and lead at high strains not to a selection of one variant, because of local grain rotations and corresponding alignment with the strain direction.

Concluding, this new method for the equilibration of solid phase microstructures with

long-range elastic interactions enables a highly efficient QA computation with several thousand interacting grains, where conventional, classical algorithms are outperformed. The problem formulation is the crucial step in quantum annealing, which is implemented here with high performance, allowing realistic material descriptions. Thus, the model belongs to one of the few application relevant QA methods in the field of materials science and presents therefore an important contribution to research (publication 2).

A detailed derivation of the coefficients of the underlying Ising formulation leads to explicit and accurate expressions for the elastic interactions between the grains, whose accuracy is crucial for the determination of correct equilibrated microstructures. The inclusion of a real space cutoff to truncate the elastic interactions is not legitimate as it leads to wrong predictions.

An important test of the developed model is the application to large systems under external mechanical loads, i.e. $N = 2500$ grains are considered, where the computation of the Ising coefficients is the computational demanding part. Here, hybrid quantum annealing just needs about one minute for the determination of the equilibrium microstructure. For tetragonal eigenstrain, the expected microstructures under varying tensile strain in horizontal direction are found, which show decreasing stripe thickness with increasing strain. Therefore, generalizations to 3D systems with high numbers of grains are possible for the microstructure equilibration with representative volume elements. This will be an important area of focus for future research.

Finally, the QA technique is directly applied to LLZO under usage of the previous calculated lattice parameters and inclusion of a chemical contribution, which represents the volume fractions of the grains. Here, the doping level in LLZO determines the phase fractions of tetragonal and cubic phases, leading to a competing interplay between chemical and elastic effects. The resulting microstructures for varying chemical energy strength and phase fractions reveal that the elastic contributions favor a formation of ion conducting channels of cubic phase. This self-organization process through the presence of elastic effects may enable a grain engineering in the future.

Apart from the considered bulk energies, also the interplay with interfacial energies is investigated, where negative and positive interfacial energies show the expected influence on the resulting microstructures. Depending on the sign of the interfacial energy, the system favors more or less interfaces in the resulting pattern, leading to structures where interfacial and elastic contributions compete (publication 3).

So far the focus of this work lies on ground state energies at $T = 0\,\mathrm{K}$, however, regarding

materials science the physical properties of solid electrolytes at finite temperatures are of high interest. The developed Monte Carlo sampling method via quantum annealing allows the determination of finite temperature properties at low computational costs. For the first demonstration of the sampling method a spin glass system is considered, which shows that the distribution of states follows a Boltzmann distribution. Via the low energy configuration set and the approximated canonical partititon function, further observables can be computed. The computed thermodynamic properties coincide with the theoretical expectation at low temperatures, where at higher temperatures deviations from theory are found. Therefore, the imperfect QA process delivers a set of states in the phase space, which contributes strongest to the partition function due to their high Boltzmann weight.

In order to investigate the performance and limitations of the sampling approach, the 1D Ising model and its analytical solution is considered for the calculation of further thermodynamic properties. The QA sampling is much faster and requires less computer ressources than classical algorithms, because the QA sampling uses the same configurations for all temperatures, while for the Metropolis algorithm a separate Markov chain is generated for each temperature.

A limitation of the QA approach is that only smaller system sizes can be considered via pure QA due to the available machine sizes, however, the development of quantum annealing is an ongoing process, where in the future machines with more qubits and higher connectivity are present. Future research will focus on effective implementations of hybrid quantum annealing and convergence studies to extrapolate to the limit of infinite sample sizes. Concluding, the QA sampling is a novel technique for the characterization of solid electrolytes, which allows the highly efficient prediction of thermophysical properties at low temperatures, and complements classical approaches perfectly. The application of this sampling technique to the microstructure equilibration of LLZO will allow the prediction of thermophysical properties with high efficiency at low temperatures and will be subject of further research. An implementation of the QA sampling in existent QA codes allows the usage of found exited states during the optimization towards the ground state for almost no costs (publication 4).

Bibliography

[1] B.S. Vishnugopi, E. Kazyak, J.A. Lewis, J. Nanda, M.T. McDowell, N.P. Dasgupta, and P.P. Mukherjee. Challenges and Opportunities for Fast Charging of Solid-State Lithium Metal Batteries. *ACS Energy Lett.*, 6:3734–3749, 2021.

[2] Internation Energy Agency (IEA). Executive summary - Global EV Outlook 2023 - Analysis. , 2023. [Online; accessed 26-February-2024].

[3] Reuters. Taiwan battery maker ProLogium signs investment deal with Mercedes-Benz, 27 January 2022. . [Online; accessed 26-February-2024].

[4] Reuters. Toyota, Idemitsu tie up to mass-produce all-solid-state batteries, 12 October 2023. . [Online; accessed 26-February-2024].

[5] M. Brooks. Quantum computers: what are they good for? *Nature*, 617:S1–S3, 2023.

[6] R. Murugan, V. Thangadurai, and W. Weppner. Fast Lithium Ion Conduction in Garnet-Type $Li_7La_3Zr_2O_{12}$. *Angew. Chem. Int. Ed.*, 46:7778–7781, 2007.

[7] M.M. Raju, F. Altayran, M. Johnson, D. Wang, and Q. Zhang. Crystal Structure and Preparation of $Li_7La_3Zr_2O_{12}$ (LLZO) Solid-State Electrolyte and Doping Impacts on the Conductivity: An Overview. *Electrochem*, 2:390–414, 2021.

[8] H. Buschmann, J. Dlle, S. Berendts, A. Kuhn, P. Bottke, M. Wilkening, P. Heitjans, A. Senyshyn, H. Ehrenberg, A. Lotnyk, V. Duppel, L. Kienle, and J. Janek. Structure and dynamics of the fast lithium ion conductor "$Li_7La_3Zr_2O_{12}$". *Phys. Chem. Chem. Phys.*, 13(43):19378–19392, 2011.

[9] Y. Li, J.-T. Han, C.-A. Wang, S.C. Vogel, H. Xie, M. Xu, and J.B. Goodenough. Ionic distribution and conductivity in lithium garnet $Li_7La_3Zr_2O_{12}$. *J. Power Sources*, 209:278–281, 2012.

[10] J.L. Allen, J. Wolfenstine, E. Rangasamy, and J. Sakamoto. Effect of substitution (Ta, Al, Ga) on the conductivity of $Li_7La_3Zr_2O_{12}$. *J. Power Sources*, 206:315–319, 2012.

[11] E. Rangasamy, J. Wolfenstine, and J. Sakamoto. The role of Al and Li concentration on the formation of cubic garnet solid electrolyte of nominal composition $Li_7La_3Zr_2O_{12}$. *Solid State Ion.*, 206:28–32, 2012.

[12] A.A. Hubaud, D.J. Schroeder, B. Key, B.J. Ingram, F. Dogan, and J.T. Vaughey. Low temperature stabilization of cubic $(Li_{7-x}Al_{x/3})La_3Zr_2O_{12}$: role of aluminium during formation. *J. Mater. Chem. A*, 1:8813–8818, 2013.

[13] B. Stanje, D. Rettenwander, S. Breuer, M. Uitz, S. Berendts, M. Lerch, R. Uecker, G. Redhammer, I. Hanzu, and M. Wilkening. Solid Electrolytes: Etremely Fast Charge Carriers in Garnet-Type $Li_6La_3ZrTaO_{12}$ Single Crystal. *Ann. Phys.*, 529:1700140, 2017.

[14] J.F. Nonemacher, C. Hüter, H. Zheng, J. Malzbender, M. Krüger, R. Spatschek, and M. Finsterbusch. Microstructure and properties investigation of garnet structured $Li_7La_3Zr_2O_{12}$ as electrolyte for all-solid-state batteries. *Solid State Ion.*, 321:126–134, 2018.

[15] A.-N. Wang, J.F. Nonemacher, G. Yan, M. Finsterbusch, J. Malzbender, and M. Krüger. Mechanical properties of the solid electrolyte Al-substituted $Li_7La_3Zr_2O_{12}$ (LLZO) by utilizing micro-pillar indentation splitting test. *J. Eur. Ceram. Soc.*, 38:3201–3209, 2018.

[16] G. Han, B. Kinzer, R. Garcia-Mendez, H. Choe, J. Wolfenstine, and J. Sakamoto. Correlating the effect of dopant type (Al, Ga, Ta) on the mechanical and electrical properties of hot-pressed Li-garnet electrolyte. *J. Eur. Ceram. Soc.*, 40:1999–2006, 2020.

[17] B. Andriyevsky, K. Doll, and T. Jacob. Ab initio molecular dynamics study of lithium diffusion in tetragonal $Li_7La_3Zr_2O_{12}$. *Mater. Chem. Phys.*, 185:210–217, 2017.

[18] F.-F. Lu and H.-K. Tian. Dopant-induced modulation of lithium-ion conductivity in cubic garnet solid electrolytes: a first-principles study. *Phys. Chem. Chem. Phys.*, 25:18973–18982, 2023.

[19] S. KC, R.C. Longo, K. Xiong, and K. Cho. Point defects in garnet-type solid electrolyte (c − $Li_7La_3Zr_2O_{12}$) for Li-ion batteries. *Solid State Ion.*, 261:100–105, 2014.

[20] D. Rettenwander, G. Redhammer, F. Preishuber-Pflügl, L. Cheng, L. Miara, R. Wagner, A. Welzl, E. Suard, M.M. Doeff, M. Wilkening, J. Fleigl, and G. Amthauer. Structural and Electrochemical Consequences of Al and Ga Cosubstitution in $Li_7La_3Zr_2O_{12}$ Solid Electrolytes. *Chem. Mater.*, 28(7):2384–2392, 2016.

[21] A. Moradabadi and P. Kaghazchi. Defect chemistry in cubic $Li_{6.26}Al_{0.25}La_3Zr_2O_{12}$ solid electrolyte: A density functional theory study. *Solid State Ion.*, 338:74–79, 2019.

[22] M. Nakayama, M. Kotobuki, H. Munakata, M. Nogami, and K. Kanamura. First-principles density functional calculation of electrochemical stability of fast Li ion conducting garnet-type oxides. *Phys. Chem. Chem. Phys.*, 14:10008–10014, 2012.

[23] Y. Zhu, X. He, and Y. Mo. Origin of Outstanding Stability in the Lithium Solid Electrolyte Materials: Insights from Thermodynamic Analyses Based on First-Principles Calculations. *ACS Appl. Mater. Interfaces*, 7:215–223, 2015.

[24] F. Han, Y. Zhu, X. He, Y. Mo, and C. Wang. Electrochemical Stability of $Li_{10}GeP_2Sr_{12}$ and $Li_7La_3Zr_2O_{12}$ Solid Electrolytes. *Adv. Energy Mater.*, 6:1501590, 2016.

[25] S. Yu, R.D. Schmidt, R. Garcia-Mendez, E. Herbert, N.J. Dudney, J.B. Wolfenstine, J. Sakamoto, and D.J. Siegel. Elastic Properties of the Solid Electrolyte $Li_7La_3Zr_2O_{12}$ (LLZO). *Chem. Mater.*, 28(1):197–206, 2016.

[26] D.O. Shin, K. Oh, K.M. Kim, K.-Y. Park, B. Lee, Y.-G. Lee, and K. Kang. Synergistic multi-doping effects on the $Li_7La_3Zr_2O_{12}$ solid electrolyte for fast lithium ion conduction. *Sci. Rep.*, 5:18053, 2015.

[27] Y. Meesala, Y.-K. Liao, A. Jena, N.-H. Yang, W.K. Pang, S.-F. Hu, H. Chang, C.-E. Liu, S.-C. Liao, J.-M. Chen, X. Guo, and R.-S. Liu. An efficient multi-doping strategy to enhance Li-ion conductivity in the garnet-type solid electrolyte $Li_7La_3Zr_2O_{12}$. *J. Mater. Chem. A*, 7:8589–8601, 2019.

[28] S.-K. Jung, H. Gwon, H. Kim, G. Yoon, D. Shin, J. Hong, C. Jung, and J.-S. Kim. Unlocking the hidden chemical space in cubic-phase garnet solid electrolyte for efficient quasi-all-solid-state lithium batteries. *Nat. Commun.*, 13:7638, 2022.

[29] H.U. Lee, S. Han, D.G. Lee, H. Ko, J. Lee, W.B. Im, T. Song, J. Choi, and S.B. Cho. Isovalent multi-component doping strategy for stabilizing cubic-$Li_7La_3Zr_2O_{12}$ with excellent Li mobility. *Chem. Eng. J.*, 471:144552, 2023.

[30] C.-Z. Zhao, P.-Y. Chen, R. Zhang, X. Chen, B.-Q. Li, X.-Q. Zhang X.-B. Cheng, and Q. Zhang. An ion redistributor for dendrite-free lithium metal anodes. *Sci. Adv.*, 4:eaat3446, 2018.

[31] F. Han, A.S. Westover, J. Yue, X. Fan, F. Wang, M. Chi, D.N. Leonard, N.J. Dudney, H. Wang, and C. Wang. High electronic conductivity as the origin of lithium dendrite formation within solid electrolytes. *Nat. Energy*, 4:187–196, 2019.

[32] J. Sastre, M.H. Futscher, L. Pompizi, A. Aribia, A. Priebe, J. Overbeck, M. Stiefel, and A.N. Tiwari Y.E. Romanyuk. Blocking lithium dendrite growth in solid-state batteries with an ultrathin amorphous Li-La-Zr-O solid electrolyte. *Commun. Mater.*, 2:76, 2021.

[33] C. Zhu, T. Fuchs, S.A.L. Weber, F.H. Richter, G. Glasser, F. Weber, H.-J. Butt, J. Janek, and R. Berger. Understanding the evolution of lithium dendrites at $Li_{6.25}Al_{0.25}La_3Zr_2O_{12}$ grain boundaries via operando microscopy techniques. *Nat. Commun.*, 14:1300, 2023.

[34] J.A. Dawson. Going against the Grain: Atomistic Modeling of Grain Boundaries in Solid Electrolytes for Solid State Batteries. *ACS Mater. Au.*, 4:1–13, 2024.

[35] Z. Qin, Y. Xie, X. Meng, D. Qian, C. Shan, G. He, L. Wan, and Y. Huang. Suppressing lithium dendrite growth enabled by high-performance garnet LLZO for graphite-based full cell solid-state lithium batteries. *J. Phys. Chem. Solids*, 185:111789, 2024.

[36] C.D. Fincher, C.E. Athanasiou, C. Gilgenbach, M. Wang, B.W. Sheldon, W.C. Carter, and Y.-M. Chiang. Controlling dendrite propagation in solid-state batteries with engineered stress. *Joule*, 6(12):2794–2809, 2022.

[37] G. McConohy, X. Xu, T. Cui, E. Barks, S. Wang, E. Kaeli, C. Melamed, X.W. Gu, and W.C. Chueh. Mechanical regulation of lithium intrusion probability in garnet solid electrolytes. *Nat. Energy*, 8:241–250, 2023.

[38] D. Rodney, Y. Le Bouar, and A. Finel. Phase field methods and dislocations. *Acta Mat.*, 51:17–30, 2003.

[39] L. Chen, J. Chen, R.A. Lebensohn, Y.Z. Ji, T.W. Heo, S. Bhattacharyya, K. Chang, S. Mathaudhu, Z.K. Liu, and L.-Q. Chen. An integrated fast Fourier transform-based phase-field and crystal plasticity approach to model recrystallization of three dimensional polycrystals. *Comput. Mehods Appl. Mech. Eng.*, 285:829–848, 2015.

[40] K. Wang, M. Weikamp, M. Lin, C. Zimmermann, R. Schwaiger, U. Prahl, M. Hunkel, and R. Spatschek. Influence of Interface Proximity on Precipitation Thermodynamics. *Metals*, 10:1292, 2020.

[41] R. Spatschek, G. Gobbi, C. Hüter, A. Chakrabarty, U. Aydin, S. Brinckmann, and J. Neugebauer. Scale bridging description of coherent phase equilibria in the presence of surfaces and interfaces. *Phys. Rev. B*, 94:134106, 2016.

[42] A. Karma and W.J. Rappel. Phase-field method for computationally efficient modeling of solidification with arbitrary interface kinetics. *Phys. Rev. E*, 53:R3017(R), 1996.

[43] L.-Q. Chen. Phase-field models for microstructure evolution. *Annu. Rev. Mater. Res.*, 32:113–140, 2002.

[44] A. Finel, Y. Le Bouar, B. Dabas, B. Appolaire, Y. Yamada, and T. Mohri. Sharp phase field method. *Phys. Rev. Lett.*, 121:025501, 2018.

[45] K. Wang, G. Boussinot, C. Hüter, E.A. Brener, and R. Spatschek. Modeling of dendritic growth using a quantitative nondiagonal phase field model. *Phys. Rev. Mater.*, 4:033802, 2020.

[46] D. Yang, Y. Wang, R. Pan, R. Chen, and Z. Chen. A neural network based state-of-health estimation of lithium-ion battery in electric vehicles. *Energy Procedia*, 105:2059–2064, 2017.

[47] K.T. Butler, D.W. Davies, H. Cartwright, O. Isayev, and A. Walsh. Machine learning for molecular and materials science. *Nature*, 559:547–555, 2018.

[48] J. Vandermause, S.B. Torrisi, S. Batzner, Y. Xie, L. Sun, A.M. Kolpak, and B. Kozinsky. On-the-fly active learning of interpretable Bayesian force fields for atomistic rare events. *npj Comput. Mater.*, 6:20, 2020.

[49] B. Celik, R. Sandt, L.C. Pereira dos Santos, and R. Spatschek. Prediction of Battery Cycle Life Using Early-Cycle Data, Machine Learning and Data Management. *Batteries*, 8:266, 2022.

[50] G. Hegde and R.C. Bowen. Machine-learned approximations to Density Functional Theory Hamiltonians. *Sci. Rep.*, 7:42669, 2017.

[51] R. Jinnouchi, J. Lahnsteiner, F. Karsai, G. Kresse, and M. Bokdam. Phase Transitions of Hybrid Perovskites Simulated by Machine-Learning Force Fields Trained on the Fly with Bayesian Inference. *Phys. Rev. Lett.*, 122:225701, 2019.

[52] M. Bogojeski, L. Vogt-Maranto, M.E. Tuckerman, K.-R. Müller, and K. Burke. Quantum chemical accuracy from density functional approximations via machine learning. *Nat. Commun.*, 11:5223, 2020.

[53] M. Hodapp and A. Shapeev. Machine-learning potentials enable predictive and tractable high-throughput screening of random alloys. *Phys. Rev. Materials*, 5:113802, 2021.

[54] L.K. Grover. A fast quantum mechanical algorithm for database search. *Proceedings of the twenty-eighth annual ACM symposium on Theory of Computing*, pages 212–219, 1996.

[55] P.W. Shor. Polynomial-Time Algorithms for Prime Factorization and Discrete Logarithms on a Quantum Computer. *SIAM J. Sci. Statist. Comput.*, 26:1484, 1997.

[56] N. Ofek, A. Petrenko, R. Heeres, P. Reinhold, Z. Leghtas, B. Vlastakis, Y. Liu, L. Frunzio, S.M. Girvin, L. Jiang, M. Mirrahimi, M.H. Devoret, and R.J. Schoelkopf. Extending the lifetime of a quantum bit with error correction in superconducting circuits. *Nature*, 536:441–445, 2016.

[57] A.P. Vepsäläinen, A.H. Karamlou, J.L. Orrell, A.S. Dogra, B. Loer, F. Vasconcelos, D.K. Kim, A.J. Melville, B.M. Niedzielski, J.L. Yoder, S. Gustavsson, J.A. Formaggio, B.A. VanDevender, and W.D. Olivier. Impact of ionizing radiation on superconducting qubit coherence. *Nature*, 584:551–556, 2020.

[58] Y. Kim, A. Eddins, S. Anand, K.X. Wei, E. van den Berg, S. Rosenblatt, H. Nayfeh, Y. Wu, M. Zaletel, K. Temme, and A. Kandala. Evidence for the utility of quantum computing before fault tolerance. *Nature*, 618:500–505, 2023.

[59] Google Quantum AI. Suppressing quantum errors by scaling a surface code logical qubit. *Nature*, 614:676–681, 2023.

[60] S. Pirandola, U.L. Andersen, L. Banchi, M. Berta, D. Bunandar, R. Colbeck, D. Englund, T. Gehring, C. Lupo, C. Ottaviani, J.L. Pereira, M. Razavi, J.S. Shaari, M. Tomamichel, V.C. Usenko, G. Vallone, P. Villoresi, and P. Wallden. Advances in quantum cryptography. *Adv. Opt. Photon*, 12(4):1012–1236, 2020.

[61] G. Xu, J. Mao, E. Sakk, and S.P. Wang. An Overview of Quantum-Safe Approaches: Quantum Key Distribution and Post-Quantum Cryptography. *IEEE 57th Annual Conference on Information Sciences and Systems (CISS)*, 2023.

[62] X. Guo, C.R. Breum, J. Borregaard, S. Izumi, M.V. Larsen, T. Gehring, M. Christandl, J.S. Neergaard-Nielsen, and U.L. Andersen. Distributed quantum sensing in a continuous-variable entangled network. *Nat. Phys.*, 16:281–284, 2020.

[63] S.J. Pauka, K. Das, R. Kalra, A. Moini, Y. Yang, M. Trainer, A. Bousquet, C. Cantaloube, N. Dick, G.C. Gardner, M.J. Manfra, and D.J. Reilly. A cryogenic CMOS chip for generating control signal for multiple qubits. *Nat. Electron.*, 4:64–70, 2021.

[64] D. Bluvstein, S.J. Evered, A.A. Geim, S.H. Li, H. Zhou, T. Manovitz, S. Ebadi, M. Cain, M. Kalinowski, D. Hangleiter, J.P.B. Ataides, N. Maskara, I. Cong, X. Gao, P.S. Rodriguez, T. Karolyshyn, G. Semeghini, M.J. Gullans, M. Greiner, V. Vuletić, and M.D. Lukin. Logical quantum processor based on reconfigurable atom arrays. *Nature*, 626:58–65, 2024.

[65] D. Wilsch, D. Rieger, P. Winkel, M. Willsch, C. Dickel, J. Krause, Y. Ando, R. Lescanne, Z. Leghtas, N.T. Bronn, P. Deb, O. Lanes, Z.K. Minev, B. Dennig, S. Geisert, S. Günzler, S. Ihssen, P. Paluch, T. Reisinger, and ... I.M. Pop. Observation of Josephson harmonics in tunnel junctions. *Nat. Phys.*, 2024.

[66] A.B. Finnila, M.A. Gomez, C. Sebenik, C. Stenson, and J.D. Doll. Quantum annealing: a new method for minimizing multidimensional functions. *Chem. Phys. Lett.*, 219:343–348, 1994.

[67] T. Kadowaki and H. Nishimori. Quantum annealing in the transverse Ising model. *Phys. Rev. E*, 58:5355, 1998.

[68] J. Brooke, D. Bitko, T.F. Rosenbaum, and G. Aeppli. Quantum Annealing of a Disordered Magnet. *Science*, 284:779–781, 1999.

[69] S. Morita and H. Nishimori. Mathematical foundation of quantum annealing. *J. Math. Phys.*, 49:125210, 2008.

[70] A. Rajak, S. Suzuki, A. Dutta, and B.K. Chakrabarti. Quantum annealing: an overview. *Phil. Trans. R. Soc. A*, 381:20210417, 2023.

[71] R. Harris, Y. Sato, A.J. Berkley, M. Reis, F. Altomare, M.H. Amin, K. Boothby, P. Bunyk, C. Deng, C. Enderud, S. Huang, E. Hoskinson, M. W. Johnson, E. Ladizinsky, N. Ladizinsky, T. Lanting, R. Li, T. Medina, R. Molavi, and ... J. Yao. Phase transitions in a programmable quantum spin glass simulator. *Science*, 361:162–165, 2018.

[72] P. Kairys, A.D. King, I. Ozfidan, K. Boothby, J. Raymond, A. Banerjee, and T.S. Humble. Simulating the Shastry-Sutherland Ising Model Using Quantum Annealing. *PRX Quantum*, 1:020320, 2020.

[73] K. Kitai, J. Guo, S. Ju, S. Tanaka, K. Tsuda, J. Shiomi, and R. Tamura. Designing metamaterials with quantum annealing and factorization machines. *Phys. Rev. Res.*, 2:013319, 2020.

[74] K. Utimula, T. Ichibha, G.I. Prayogo, K. Hongo, K. Nakano, and R. Maezono. A quantum annealing approach to ionic diffusion in solids. *Sci. Rep.*, 11:7261, 2021.

[75] B. Camino, J. Buckeridge, P.A. Warburton, V. Kendon, and S.M. Woodley. Quantum computing and materials science: A practical guide to applying quantum annealing to the configurational analysis of materials. *J. Appl. Phys.*, 133:221102, 2023.

[76] H. Sampei, K. Saegusa, K. Chishima, T. Higo, S. Tanaka, Y. Yayama, M. Nakamura, K. Kimura, and Y. Sekine. Quantum Annealing Boosts Prediction of Multimolecular Adsorption on Solid Surfaces Avoiding Combinatorial Explosion. *JACS Au*, 3(4):991–996, 2023.

[77] K. Otsuka and X. Ren. Physical metallurgy of TiNi-based shape memory alloys. *Prog. Mater. Sci.*, 50:511, 2005.

[78] L. Mañosa and A. Planes. Mechanocaloric effects in shape memory alloys. *Phil. Trans. R. Soc. A*, 374:20150310, 2016.

[79] S. Kartha, T. Castán, J.A. Krumhansl, and J.P. Sethna. Spin-Glass Nature of Tweed Precursors in Martensitic Transformations. *Phys. Rev. Lett.*, 67:3630, 1991.

[80] J.P. Sethna, S. Kartha, T. Castán, and J.A. Krumhansl. Tweed in Martensites: A Potential New Spin Glass. *Phys. Scr.*, 1992:214–219, 1992.

[81] D. Sherrington. A simple spin glass perspective on martensitic shape-memory alloys. *J. Phys.: Condens. Matter*, 20:304213, 2008.

[82] R. Vasseur and T. Lookman. Spin Models for Ferroelastics: Towards a Spin Glass Description of Strain Glass. *Solid State Phenom.*, 172-174:1078–1083, 2011.

[83] O. Parekh, J. Wendt, L. Shulenburger, A. Landahl, J. Moussa, and J. Aidun. Benchmarking Adiabatic Quantum Optimization for Complex Network Analysis. https://www.osti.gov/biblio/1459086, 2015.

[84] M. Jünger, E. Lobe, P. Mutzel, G. Reinelt, F. Rendl, G. Rinaldi, and T. Stollenwerk. Quantum Annealing versus Digital Computing: An Experimental Comparison. *ACM J. Exp. Algorithms*, 26(1):1.9, 2021.

[85] B. Yan and N.A. Sinitsyn. Analytical solution for nonadiabatic quantum annealing to arbitrary Ising spin Hamiltonian. *Nat. Commun.*, 13:2212, 2022.

[86] A.D. King, J. Raymond, T. Lanting, R. Harris, A. Zucca, F. Altomare, A.J. Berkley, K. Boothby, S. Ejtemaee, C. Enderud, E. Hoskinson, S. Huang, E. Ladizinsky, A.J.R. MacDonald, G. Marsden, R. Molavi, T. Oh, G. Poulin-Lamarre, M. Reis, and ... M.H. Amin. Quantum critical dynamics in a 5,000-qubit programmable spin glass. *Nature*, 617:61–66, 2023.

[87] A. Perdomo-Ortiz, N. Dickson, M. Drew-Brook, G. Rose, and A. Aspuru-Guzik. Finding low-energy conformations of lattice protein models by quantum annealing. *Sci. Rep.*, 2:571, 2012.

[88] E. Boyda, S. Basu, S. Ganguly, A. Michaelis, S. Mukhopadhyay, and R.R. Nemani. Deploying a quantum annealing processor to detect tree cover in aerial imagery of California. *PLOS ONE*, 12(2), 2017.

[89] F. Neukart, G. Compostella, C. Seidel, D. von Dollen, S. Yarkoni, and B. Parney. Traffic Flow Optimization Using a Quantum Annealer. *Front. ICT*, 4(29), 2017.

[90] R.Y. Li, R. Di Felice, R. Rohs, and D.A. Lidar. Quantum annealing versus classical machine learning applied to a simplified computational biology problem. *npj Quantum Inf.*, 4(14), 2018.

[91] M. Ohzeki, A. Miki, M.J. Miyama, and M. Terabe. Control of Automated Guided Vehicles Without Collision by Qantum Annealer and Digital Devices. *Front. Comput. Sci.*, 1(9), 2019.

[92] A. Irbäck, L. Knuthson, S. Mohanty, and C. Peterson. Folding lattice proteins with quantum annealing. *Phys. Rev. Res.*, 4:043013, 2022.

[93] A. Irbäck, L. Knuthson, S. Mohanty, and C. Peterson. Using quantum annealing to design lattice proteins. *Phys. Rev. Res.*, 6:013162, 2024.

[94] J. Nelson, M. Vuffray, A.Y. Lokhov, T. Albash, and C. Coffrin. High-Quality Thermal Gibbs Sampling with Quantum Annealing Hardware. *Phys. Rev. Appl.*, 17:044046, 2022.

[95] M Vuffray, C. Coffrin, Y.A. Kharkov, and A.Y. Lokhov. Programmable Quantum Annealers as Noisy Gibbs Samplers. *PRX Quantum*, 3:020317, 2022.

[96] S. Mandrà, Z. Zhu, and H. G. Katzgraber. Exponentially Biased Ground-State Sampling of Quantum Annealing Machines with Transverse-Field Driving Hamiltonians. *Phys. Rev. Lett.*, 118:070502, 2017.

[97] M.S. Könz, G. Mazzola, A.J. Ochoa, H.G. Katzgraber, and M. Troyer. Uncertain fate of fair sampling in quantum annealing. *Phys. Rev. A*, 100:030303, 2019.

[98] S. Mukherjee and B.K. Chakrabarti. On the question of ergodicity in quantum spin glass phase and its role in quantum annealing. *J. Phys. Soc. Jpn.*, 88:061004, 2019.

[99] M. Yamamoto, M. Ohzeki, and K. Tanaka. Fair Sampling by Simulated Annealing on Quantum Annealer. *J. Phys. Soc. Jpn.*, 89:025002, 2020.

[100] G. Kresse and J. Furthmüller. Efficient iterative schemes for *ab initio* total-energy calculations using a plane-wave basis set. *Phys. Rev. B*, 54(16):11169, 1996.

[101] M.J. Lain, J. Brandon, and E. Kendrick. Design Strategies for High Power vs. High Energy Lithium Ion Cells. *Batteries*, 5:64, 2019.

[102] P.M. Attia, A. Bills, F.B. Planella, P. Dechent, G. dos Reis, M. Dubarry, P. Gasper, R. Gilchrist, S. Greenbank, D. Howey, O. Liu, E. Khoo, Y. Preger, A. Soni, S. Sripad, A.G. Stefanopoulou, and V. Sulzer. Review - "Knees" in Lithium-Ion Battery Aging Trajectories. *J. Electrochem. Soc.*, 169:060517, 2022.

[103] J.B. Goodenough and Y. Kim. Challenges for Rechargeable Li Batteries. *Chem. Mater.*, 22:587–603, 2010.

[104] X. Lin, K. Khosravinia, X. Hu, J. Li, and W. Lu. Lithium Plating Mechanism, Detection, and Mitigation in Lithium-Ion Batteries. *Prog. Energy Combust. Sci.*, 87:100953, 2021.

[105] H. Adenusi, G.A. Chass, S. Passerini, K.V. Tian, and G. Chen. Lithium Batteries and the Solid Electrolyte Interphase (SEI) - Progress and Outlook. *Adv. Energy Mater.*, 13:2203307, 2023.

[106] S. Kim, J.-S. Kim, L. Miara, Y. Wang, S.-K. Jung, S.Y. Park, Z. Song, H. Kim, M. Badding, J. Chang, V. Roev, G. Yoon, R. Kim, J.-H. Kim, K. Yoon, D. Im, and K. Kang. High-energy and durable lithium metal batteries using garnet-type solid electrolytes with tailored lithium-metal compatibility. *Nat. Commun.*, 13:1883, 2022.

[107] Q. Liu, L. Jiang, P. Zheng, J. Sun, C. Liu, J. Chai, X. Li, Y. Zheng, and Z. Liu. Recent Advantages in Stability Issues of Inorganic Solid Electrolytes and Composite Solid Electrolytes for All-Solid-State Batteries. *Chem. Rec.*, 22:e202200116, 2022.

[108] C. Wang, K. Fu, S.P. Kammampata, D.W. McOwen, A.J. Samson, L. Zhang, G.T. Hitz, A.M. Nolan, E.D. Wachsman, Y. Mo, V. Thangadurai, and L. Hu. Garnet-Type Solid-State Electrolytes: Materials, Interfaces, and Batteries. *Chem. Rev.*, 120:4257–4300, 2020.

[109] J.-M. Tarascon and M. Armand. Issues and challenges facing rechargeable lithium batteries. *Nature*, 414:359–367, 2001.

[110] D. Lin, Y. Liu, and Y. Cui. Reviving the lithium metal anode for high-energy batteries. *Nature Nanotech*, 12:194–206, 2017.

[111] R. Koerver, W. Zhang, L. de Biasi, S. Schweidler, A.O. Kondrakov, S. Kolling, T. Brezesinski, P. Hartmann, W.G. Zeier, and J. Janek. Chemo-mechanical expansion of lithium electrode materials - on the route to mechanically optimized all-solid-state batteries. *Energy Environ. Sci.*, 11:2142–2158, 2018.

[112] S. Kalnaus, N.J. Dudney, A.S. Westover, E. Herbert, and S. Hackney. Solid-state batteries: The critical role of mechanics. *Science*, 381:1300, 2023.

[113] E. Enkhbayar and J.H. Kim. Study of Codoping Effects of Ta^{5+} and Ga^{3+} on Garnet $Li_7La_3Zr_2O_{12}$. *ACS Omega*, 7(50):47265–47273, 2022.

[114] L.J. Miara, S.P. Ong, Y. Mo, W.D. Richards, Y. Park, J.-M. Lee, H.S. Lee, and G. Ceder. Effect of Rb and Ta Doping on the Ionic Conductivity and Stability of the Garnet Li_{7+2x-y} $(La_{3-x}$ $Rb_x)$ $(Zr_{2-y}$ $Ta_y)$ O_{12} $(0 \leq x \leq 0.375, 0 \leq y \leq 1)$ Superionic Conductor: A First Principles Investigation. *Chem. Mater.*, 25:3048–3055, 2013.

[115] A. Kuhn, J.-Y. Choi, L. Robben, F. Tietz, M. Wilkening, and P. Heitjans. Li Ion Dynamics in Al-Doped Garnet-Type $Li_7La_3Zr_2O_{12}$ Crystallizing with Cubic Symmetry. *Z. Phys. Chem.*, 226:525–537, 2012.

[116] Y. Wang and W. Lai. High Ionic Conductivity Lithium Garnet Oxides of $Li_{7-x}La_3Zr_{2-x}Ta_xO_{12}$ Compositions. *Electrochem. Solid-State Lett.*, 15(5):A68, 2012.

[117] A.G. Khachaturyan. *Theory of Structural Transformations in Solids.* Dover Publications, Inc., Mineola, New York, 2008.

[118] L.D. Landau and E.M. Lifshitz. *Theory of Elasticity: Volume 7.* Pergamon Press, U.K., 1970.

[119] R.W. Balluffi. *Introduction to Elasticity Theory for Crystal Defects.* Cambridge University Press, Cambridge, UK, 2012.

[120] H. Reiner. Eigenspannungen und Eigenspannungsquellen. *Z. Angew. Math. Mech.*, 11(1):1–8, 1931.

[121] T. Mura. *Micromechanics of Defects in Solids, Second, revised edition.* Kluwer Academic Publishers, Dordrecht, Netherlands, 1987.

[122] J.D. Eshelby. The determination of the elastic field of an ellipsoidal inclusion, and related problems. *Proc. R. Soc. A*, 241(1226):376–396, 1957.

[123] J.D. Eshelby. Elastic inclusions and inhomogeneities. *Prog. Solid Mech.*, 2:525–535, 1961.

[124] P. Fratzl, O. Penrose, and J.L. Lebowitz. Modeling of Phase Separation in Alloys with Coherent Elastic Misfit. *J. Stat. Phys.*, 95:1429–1503, 1999.

[125] M. Born and R. Oppenheimer. Zur Quantentheorie der Molekeln. *Ann. Phys.*, 4(84):457–484, 1927.

[126] J.G. Lee. *Computational Materials Science - An Introduction*. CRC Press, Boca Raton, Florida, 2017.

[127] P. Hohenberg and W. Kohn. Inhomogeneous electron gas. *Phys. Rev.*, 136(B864), 1964.

[128] W. Kohn and L.J. Sham. Self-consistent equations including exchange and correlation effects. *Phys. Rev.*, 140(A1133), 1965.

[129] J.P. Perdew, K. Burke, and M. Ernzerhof. Generalized Gradient Approximation Made Simple. *Phys. Rev. Lett.*, 77(18):3865, 1996.

[130] F. Bloch. Über die Quantenmechanik der Elektronen in Kristallgittern. *Z. Phys.*, 52(7-8):555–600, 1929.

[131] M. Nielsen and I.L. Chuang. *Quantum Computation and Quantum Information*. Cambridge University Press, Cambridge, 2010.

[132] M.W. Johnson, M.H. Amin, S. Gildert, T. Lanting, F. Hamze, N. Dickson, R. Harris, A.J. Berkley, J. Johansson, P. Bunyk, E.M. Chapple, C. Enderud, J.P. Hilton, K. Karimi, E. Ladizinsky, N. Ladizinsky, T. Oh, I. Perminov, C. Rich, and ... G. Rose. Quantum annealing with manufactured spins. *Nature*, 473:194–198, 2011.

[133] S. Boixo, T.F. Rønnow, S.V. Isakov, Z. Wang, D. Wecker, D.A. Lidar, J.M. Martinis, and M. Troyer. Evidence for quantum annealing with more than one hundred qubits. *Nat. Phys.*, 10:218–224, 2014.

[134] T.F. Rønnow, Z. Wang, J. Job, S. Boixo, S.V. Isakov, D. Wecker, J.M. Martinis, D.A. Lidar, and M. Troyer. Defining and detecting quantum speedup. *Science*, 345:420–423, 2014.

[135] R.H. Warren. Mathematical methods for a quantum annealing computer. *J. Adv. Appl. Math.*, 3(3):82–90, 2018.

[136] J.J. Berwald. The Mathematics of Quantum-Enabled Applications on the D-Wave Quantum Computer. *Notices Am. Math. Soc.*, 66(6):832–841, 2019.

[137] T. Kadowaki and M. Ohzeki. Experimental and Theoretical Study of Thermodynamic Effects in a Quantum Annealer. *J. Phys. Soc. Jpn.*, 88:061008, 2019.

[138] D-Wave. D-Wave Systems Inc. Performance advantage in quantum Boltzmann sampling [Whitepaper]. `https://www.dwavesys.com/resources/white-paper/performance-advantage-in-quantum-boltzmann-sampling`, 2017.

[139] J. Golden and D. O'Malley. Reverse annealing for nonnegative/binary matrix factorization. *PLoS ONE*, 16(1):e0244026, 2021.

[140] A. Lucas. Ising formulations of many NP problems. *Front. Phys.*, 2(5), 2014.

[141] T. Lanting, A.J Przybysz, A.Y. Smirnov, F.M. Spedalieri, M.H. Amin, A.J. Berkley, R. Harris, F. Altomare, S. Boixo, P. Bunyk, N. Dickson, C. Enderud, J.P. Hilton, E. Hoskinson, M.W. Johnson, E. Ladizinsky, N. Ladizinsky, R. Neufeld, T. Oh, and ... G. Rose. Entanglement in a Quantum Annealing Processor. *Phys. Rev. X*, 4:021041, 2014.

[142] E. Pelofske, G. Hahn, and H. Djidjev. Optimizing the Spin Reversal Transform on the D-Wave 2000Q. In *2019 IEEE International Conference on Rebooting Computing (ICRC)*, pages 1–8, 2019.

[143] J. Raymond, R. Stevanovic, W. Bernoudy, K. Boothby, C.C. McGeoch, A.J. Berkley, P. Farré, and A.D. King. Hybrid quantum annealing for larger-than-QPU lattice-structured problems. *ACM Trans. Quantum Comput.*, 2023.

[144] V. Choi. Minor-embedding in adiabatic quantum computation: II. Minor-universal graph design. *Quantum Inf. Process.*, 10:343–353, 2011.

[145] S. Kirkpatrick, C. D. Gelatt, and M.P. Vecchi. Optimization by Simulated Annealing. *Science*, 220(4598):671–680, 1983.

[146] Y. Nourani and B. Andresen. A comparison of simulated annealing cooling strategies. *J. Phys. A: Math. Gen.*, 31:8373–8385, 1998.

[147] R. Sandt and R. Spatschek. Efficient low temperature Monte Carlo sampling using quantum annealing. *Sci. Rep.*, 13:6754, 2023.

[148] N. Metropolis, A.W. Rosenbluth, M.N. Rosenbluth, and A.H. Teller. Equation of State Calculations by Fast Computing Machines. *J. Chem. Phys.*, 21(6):1087–1092, 1953.

[149] O.I. Abiodun, A. Jantan, A.E. Omolara, K.V. Dada, N.A. Mohamed, and H. Arshad. State-of-the-art in artificial neural network applications: A survey. *Heliyon*, 4(11):e00938, 2018.

[150] F. Rosenblatt. The perceptron - A perceiving and recognizing automaton. *Cornell Aeronautical Laboratory*, 85-460-1, 1957.

[151] M. Deru and A. Ndiaye. *Deep Learning mit TensorFlow, Keras und TensorFlow.js*. Rheinwerk Verlag, Bonn, 2020.

Solid State Ionics 402 (2023) 116364

Contents lists available at ScienceDirect

Solid State Ionics

journal homepage: www.elsevier.com/locate/ssi

Investigation of mechanical properties of garnet structured $Li_7La_3Zr_2O_{12}$ under Al^{3+} and Ta^{5+} co-substitutions

Roland Sandt [a,*], Yaxue Wang [a], Robert Spatschek [a,b]

[a] Structure and Function of Materials, Institute of Energy and Climate Research (IEK-2), Forschungszentrum Jülich GmbH, 52425 Jülich, Germany
[b] JARA-ENERGY, 52425 Jülich, Germany

ARTICLE INFO

Keywords:
Solid state battery
Electrolyte
Mechanical properties
Density functional theory
Machine learning
Pores

ABSTRACT

The influence of co-substitutions on the structural and mechanical properties of garnet structured $Li_7La_3Zr_2O_{12}$ (LLZO) is investigated. Ab initio simulations of the cubic phase under Al and Ta substitutions are performed for an analysis of substitution dependencies on lattice constants, elastic moduli and hardness. The use of the differential effective medium theory methods enables a scale bridging description towards porous LLZO, with a 27% decay of Young's modulus for a porosity of 10%, compared to dense LLZO.

1. Introduction

Li-based all solid state batteries (ASSBs) are promising next generation batteries due to their high energy densities, high cycle life, low self-discharge rate and their improved safety behaviour [1–5]. The absence of liquid electrolytes prevents the cell from leakage and allows an effective usage as a modern battery in electric vehicles and other battery power driven products. However, downsides are still present like the disadvantageous volume expansion of solid battery components during usage and production [3,4,6]. Arising stresses and deformations can lead to instabilities and limitation of lifetime, what makes the knowledge of the mechanical behaviour a crucial part of actual research. Another important problem is the Li metal dendrite growth or rather intrusion [3,7–9] inside the electrolyte and therefore occuring short circuits, which can lead to premature and sudden degradation. A recent study by Fincher et al. showed that the dendrite propagation in solid-state batteries can be controlled and deflected by an imposed stress, where a critical stress of around 150 MPa can prevent short circuits [10]. McConohy et al. found out that the main reason for lithium intrusions are localized microstructural defects and cracks within the electrolyte, whose propagation direction can also be controlled mechanically [7]. Therefore, the knowledge of the solid electrolyte's mechanical properties is crucial for an effective usage and production. However, the choice of a suitable solid electrolyte, which determines the performance of the battery, is also important, where $Li_7La_3Zr_2O_{12}$ (LLZO) is a promising candidate. LLZO is an oxide with high Li-ion conductivity and chemical stability in combination with lithium metal [1,4,11]. A thermodynamically stable tetragonal phase with poor Li-ion conductivity [12,13] exists, whereas the highly conductive cubic phase is desired, which is unstable at ambient temperature [12,14]. Here, substitutions of different aliovalent elements are an effective way to stabilize the desired cubic phase, where substitutions with Al^{3+}, Ta^{5+} and Ga^{3+} show good results [13–16]. Experimentally, combined substitutions with Ta^{5+} and Ga^{3+} lead to higher ionic conductivity [13]. Nonemacher et al. [17] investigated experimentally and theoretically single substitutions of Al and Ta in LLZO and their influence on microstructure and mechanical properties.

In this work, we stabilize the cubic phase via combined substitutions of Al and Ta, where benefits of both dopants are exploited and the mechanical behaviour is investigated. Both dopants tantalum (Ta) and aluminium (Al) stabilize the cubic phase, however Al blocks lithium pathways [18], what compensates the increased ionic conductivity, while for Ta substitutions beneficial ionic conductivities are found [19], but the material's costs are also increased [17]. Shin et al. showed the fast stabilization of the cubic phase in co-substituted LLZO and the overcoming of the mentioned blocking effect [20].

Here, the determination of the mechanical properties occurs via density functional theory (DFT) simulations, where a good agreement between experiments and simulations was found for single substitutions in LLZO [17]. Research was also done in respect to the computation of elastic properties of LLZO with Al and Ta single substitutions via DFT

* Corresponding author.
E-mail address: r.sandt@fz-juelich.de (R. Sandt).

https://doi.org/10.1016/j.ssi.2023.116364
Received 5 July 2023; Received in revised form 21 September 2023; Accepted 23 September 2023
Available online 8 October 2023

simulations [21].

However, DFT calculations of LLZO lead to a high computational demand due to the large number of atoms inside the unit cell (around 190 atoms), a large number of possible substitution sites and the required high precision simulation parameters, in particular energy cutoff and the stopping criteria for electronic and ionic self-consistency loop. Therefore, an acceleration is strongly desired to increase the efficiency and to lower the necessary number of DFT runs and in the end to save energy and computing time. Apart from prescreening techniques for the identification of most favorable lattice site occupations based on an estimation of the electrostatic interaction energy [17], we present here additionally machine learning techniques for obtaining optimized predictions for the ion positions. In general, artificial intelligence, especially machine learning (ML) represents an important part in research, where data sets are analyzed efficiently and workflows and calculations are accelerated drastically. In the field of battery research, ML approaches and models are widely used for example for the prediction of battery lifetime [22]. A common ML method are artificial neural networks (ANNs), which are based on layers and nodes as "neurons" to mimic the human brain and are used to solve prediction, classification and recognition tasks [22–25]. The optimization via ML methods inside ab initio DFT simulation workflows is a current topic and studies focused on the automatically generation of force fields [26], the improvement of chemical accuracy [27] or the prediction of further physical quantities and properties [28–30].

LLZO used for battery applications is typically polycrystalline and porous, which has influence on the elastic and mechanical properties [17,31,32]. Experiments on LLZO have shown that the results of indentation tests are influenced by the porosity regarding different indentation depths and corresponding loads [17], indicating the multi-scale nature of the material. Thus, it is crucial to extend the electronic structure modeling level to the microstructure scale for a parameter free prediction of the coarse-grained mechanical properties.

2. Methods

2.1. Calculation of the mechanical properties

For all simulations density functional theory (DFT) is used, as implemented in the Vienna ab initio simulation package (VASP) [33] with plane wave basis set and the projector augmented wave (PAW) method [34,35]. The exchange-correlation energy is determined via the Perdew-Burke-Ernzerhof (PBE) generalized gradient approximation (GGA) [36] using for Li and Zr the softer pseudopotential variants which treat *p* and *s* semi-core states as valence states. Pure lithium lanthanum zirconate $Li_7La_3Zr_2O_{12}$ (LLZO) is substituted with different amounts of Al (x = 0.125, 0.25, 0.375, 0.5, 0.625 and 0.75) and Ta (y = 0.125, 0.25, 0.375, 0.5, 0.625 and 0.75), where the co-substituted LLZO results in $Li_{7-3x-y}Al_xLa_3Zr_{2-y}Ta_yO_{12}$ (Al_xTa_y:LLZO). The substitution of Li with Al creates a 3+ oxidation state, which leads to two more Li vacancies to achieve electrically neutral structures. However, the substitution of Li with Ta do not lead to more Li vacancies, but a Zr atom is replaced in the sense of electroneutrality. Due to the large set of possible substitution sites, preliminary screening calculations as explained in Ref. [17] are performed to reduce the configuration space drastically (see Fig. 1). We note that these four prescreening steps are optional, but improve efficiency and precision of the following calculations drastically. This electronic model is based on the calculation of the electrostatic energy via Ewald summation [37] and the pymatgen library [38], which provides various materials analysis features. Based on these estimates, ionic substitutions are made on sites which have the highest electrostatic energy, under consideration of the assigned oxidation states Li^{1+}, La^{3+}, Zr^{4+}, O^{2-}, Al^{3+} and Ta^{5+}.

The acceleration of the equilibrium atomic coordinates' determination can be beneficial for the reduction of the computational effort. Therefore, ML methods can replace the determination of the equilibrium structure in the calculation workflow. In this work we have developed an approach which takes guessed atomic coordinates as input values. As output, the trained ML algorithm delivers directly suggested equilibrium coordinates of the ions. To this end, we construct an artificial neural network (ANN), where the atomic Cartesian coordinates of each structure with different volumes are processed as input values (with maximum substitution level of Al $x = 0.5$ and Ta $y = 0.375$). Further details of the developed machine learning model will be presented elsewhere.

Additional preliminary ab initio simulations at the Γ point are performed for the five most energetically preferable configurations, selected via the described electronic model. Here, the energy cutoff is 550 eV and the stopping criteria for the electronic self-consistency loop is at 10^{-6} eV, while the ionic relaxation is stopped for forces smaller than 0.05 eV/Å. We note that all simulations are performed for fixed cell volume and cell shape but variable ionic positions, hence the ionic positions inside the cubic unit cell can relax during the DFT calculations for given volumes and deformations states of the cell.

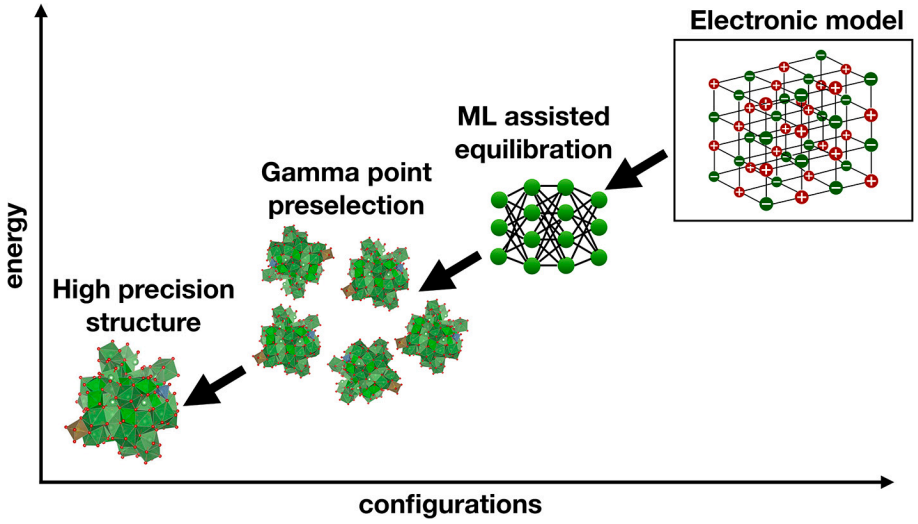

Fig. 1. Illustration of the prescreening workflow. The large set of possible substitution sites is reduced via the electronic prescreening model to only five energetically favorable configurations, which can be pre-equilibrated via ML methods. Preliminary Γ point calculations determine the configuration with the lowest energy among the five structures. We note that this configuration is used for all following productive calculations, which include in particular a full k-point sampling.

The configuration with the lowest energy among the preliminary Γ point simulations is chosen for the productive calculations of the mechanical properties. The simulation parameters are unchanged for the productive runs, except for the chosen energy cutoff of 700 eV and the $2 \times 2 \times 2$ mesh for the Brillouin zone, sampled using the Monkhorst-Pack scheme [39].

For the determination of mechanical properties, i.e. the elastic moduli in a cubic system, the knowledge of three elastic constants is required, and these elastic constants are calculated following the approach of Söderlind et al. [40]. First, the volume of the structures is varied isotropically for volume changes of up to ±3% and the resulting energy-volume curves are fitted with the Birch-Murnaghan equation of state [41–43] to determine the equilibrium volume and the bulk modulus of each structure. Next, the energy as function of a shear strain ε determines the three elastic constants in a cubic system, therefore the structures are deformed according to two deformation matrices [40]

$$\mathbf{D}_1 = \begin{pmatrix} 1+\varepsilon & 0 & 0 \\ 0 & 1+\varepsilon & 0 \\ 0 & 0 & 1/(1+\varepsilon)^2 \end{pmatrix}, \tag{1}$$

$$\mathbf{D}_2 = \begin{pmatrix} 1 & \varepsilon & 0 \\ \varepsilon & 1 & 0 \\ 0 & 0 & 1/(1-\varepsilon^2) \end{pmatrix}, \tag{2}$$

where fitting allows to calculate the elastic constants via the tetragonal shear constant C' and bulk modulus B [40],

$$C' = \frac{1}{2}(C_{11} - C_{12}), \tag{3}$$

$$B = \frac{1}{3}(C_{11} + 2C_{12}). \tag{4}$$

With the knowledge of the elastic constants, i.e. C_{11}, C_{12} and C_{44}, we calculate the directional Young's modulus [21]

$$\begin{aligned} E_{[100]} &= \frac{(C_{11} - C_{12})(C_{11} + 2C_{12})}{(C_{11} + C_{12})}, \\ E_{[110]} &= \frac{4(C_{11} - C_{12})(C_{11} + 2C_{12})C_{44}}{2C_{11}C_{44} + (C_{11} - C_{12})(C_{11} + 2C_{12})}, \\ E_{[111]} &= \frac{3(C_{11} + 2C_{12})C_{44}}{C_{11} + 2C_{12} + C_{44}}, \end{aligned} \tag{5}$$

and the shear modulus

$$\begin{aligned} G_{[100]} &= C_{44}, \\ G_{[110]} &= \frac{2(C_{11} - C_{12})C_{44}}{C_{11} - C_{12} + 2C_{44}}, \\ G_{[111]} &= \frac{3(C_{11} - C_{12})C_{44}}{C_{11} - C_{12} + 4C_{44}}. \end{aligned} \tag{6}$$

The comparison of these directional properties permits the evaluation of anisotropy of co-substituted LLZO. Additionally, we quantify the anisotropy of a cubic system via the Zener ratio [21]

$$A = \frac{2C_{44}}{C_{11} - C_{12}}. \tag{7}$$

As for most battery related applications, polycrystalline LLZO with random grain orientations is used, we use homogenization models for the estimation of the isotropic material properties on the representative volume element scale. Therefore, the isotropic Voigt's shear modulus is used as upper bound [44,45]

$$G_V = \frac{1}{5}(C_{11} - C_{12} + 3C_{44}) \tag{8}$$

and the Voigt-Reuss-Hill averaging scheme involving upper and lower bound contributions [21]

$$G_{VRH} = \frac{1}{2}\left(\frac{C_{11} - C_{12} + 3C_{44}}{5} + \frac{5C_{44}(C_{11} - C_{12})}{4C_{44} + 3(C_{11} - C_{12})}\right). \tag{9}$$

These two estimates allow to get an impression of the range of elastic constants' variations within polycrystalline LLZO using different homogenization approaches. As will be shown below, the values are rather close to each other, and therefore the consideration of more sophisticated Hashin-Shtrikman bounds [46,47] is not required.

Next, for an effectively isotropic polycrystalline material Young's modulus is estimated as [44,45]

$$E = \frac{9BG_V}{3B + G_V}. \tag{10}$$

Afterwards, we determine Vicker's hardness via the following Eq. [48]

$$H_V = 2\left(k^2 G_V\right)^{0.585} - 3, \tag{11}$$

with $k = G_V/B$ being the ratio of shear and bulk modulus. This semi-empirical model is based on Pugh's modulus ratio k and correlations between shear and bulk modulus and hardness, leading to an expression for $H_V = Ck^m G^n$, where the parameters C, m and n were previously determined by analyzing experimental data [48]. A good agreement between this theoretical model and experiments on LLZO was shown in [17].

The DFT calculations determine the elastic quantities at 0 K, where an extrapolation of the values to room temperature (298 K) leads to more accurate comparisons with experiments. As proposed in [21] for increasing temperatures the elastic moduli of oxides decrease and a reduction by 5% to mimic this decrease at 298 K can be applied.

We note that all results for the mechanical properties base on these described DFT calculations.

2.2. Differential effective medium theory

The pores appear on a scale which is larger than the electronic structure scale, therefore a scale bridging description is required. We employ a differential effective medium theory approach [49,50] to capture the influence of pores on LLZO. As the polycrystalline material is effectively isotropic, also a random distribution of spherical pores does not influence the symmetry, and therefore we can describe the elastic response through e.g. Young's modulus and Poisson ratio alone. Specifically, the effective Young's modulus calculated via the differential effective medium theory is given by [31]

$$\frac{E_{\text{eff}}}{E} = \frac{3(c-1)^3[c(8\nu - 2)(c^2 - 3c + 3) - 3(1+\nu)]}{(\nu+1)[c(4\nu - 1)(c^2 - 3c + 3) - 3]^2}, \tag{12}$$

which is expressed here in terms of the void concentration c and the Poisson ratio of the dense phase

$$\nu = \frac{3B - 2G_V}{6B + 2G_V}, \tag{13}$$

using the upper bound of Voigt's shear modulus G_V.

3. Results

3.1. Mechanical properties

Following the steps described above, we calculate the elastic constants for different co-substituted LLZO structures via DFT simulations and determine the corresponding mechanical properties under the influence of high amounts of co-substitutions.

The mechanical properties of LLZO are determined via the calculation of the elastic constants. First, the comparison of the different values for the directional properties of Young's modulus and shear modulus,

see eqs. (5) and (6), allows the evaluation of the co-substituted LLZO's anisotropy. The direction [111] shows the highest values of Young's modulus for all substitutions, whereas $E_{[100]}$ is lowest. The ratio between these directional contributions ranges from 1.13 to 1.36 for the different co-substituted configurations. The directional properties of the shear modulus exhibit similar ratios between 1.13 and 1.29, whereas the highest contribution belongs now to the [100] direction and the smallest to the direction [111]. The Zener anisotropy, see Eq. (7), allows the quantification of anisotropy in cubic systems, where a value of $A = 1$ indicates isotropy. The highest value $A = 1.44$ is found in the single substituted $Al_{0.125}$:LLZO system, while the lowest value $A = 1.19$ results for the co-substituted $Al_{0.625}Ta_{0.75}$:LLZO structure. Overall, a decrease with increasing substitution level is visible, where the values for the Zener anisotropy range in the magnitude of other isotropic oxides like NiO ($A = 1.45$) or MnO ($A = 1.54$) [21]. Therefore, we expect that in polycristalline LLZO with random grain orientation, which is isotropic, the elastic properties will not deviate much from the averaged values. This is confirmed via a comparison of the upper bound of Voigt's shear modulus (Eq. (8)) and the Voigt-Reuss-Hill averaging scheme (Eq. (9)), where the deviations between both quantities are small. The highest difference $(G_V - G_{VRH})/G_{VRH} = 0.015$ between upper bound and average shear modulus is found for $Al_{0.125}Ta_{0.125}$:LLZO, while the lowest difference is $(G_V - G_{VRH})/G_{VRH} = 0.002$ for $Al_{0.625}Ta_{0.625}$:LLZO.

Fig. 2(a) shows the resulting Young's moduli as a function of Al content. The values of the co-substituted structures are smaller than the unsubstituted structure, except for $Al_{0.125}Ta_{0.25}$:LLZO and $Al_{0.375}Ta_{0.25}$:LLZO. For increasing Al level, the curves decrease slightly, however the variation of values for Young's modulus is small. We note in passing that the cubic and tetragonal phase have comparable Young's moduli, with a slighly higher value for the tetragonal phase, which is consistently found in experiments and simulation, see [17].

The 3D representation in Fig. 3(a) shows the resulting bulk moduli as a function of Ta and Al level. General, we expect a correlation between the lattice constants and elastic moduli, where smaller/higher bulk moduli lead to higher/smaller lattice constants due to weaker/stronger interatomic bonding, respectively [17]. This relationship is visible in our data, however the variation of data is again not very pronounced. Fig. 3 (c) shows the resulting Young's modulus and confirms the previous finding, i.e. the decrease with increasing Al level.

Fig. 2(b) illustrates the resulting lattice constants as a function of substituted Ta content. It is clearly visible that the substitution of Ta has a higher influence on the lattice constant than Al substitutions. For low amounts of Ta the resulting lattice constant lies in the regime of the unsubstituted structure, whereas for increasing Ta level the corresponding lattice constants decrease. The decrease of the lattice constants of structures with high Ta level is expected due to the smaller ionic radius of Ta compared to the substituted Zr [19]. We note that single substituted Al and Ta structures are calculated for benchmarking and the later comparison to the experimental data. For the single substituted Al_x:LLZO structures a higher lattice constant than for the unsubstituted structure is found, while for the Ta_x:LLZO structures smaller lattice constants are determined. This confirms the observed influence of Ta on the microstructural properties of co-substituted systems. These findings are also supported by the results of the theoretical and experimental investigation with single substitutions [17]. Overall, the variation of the lattice constants between the different co-substituted configurations is small and less than 0.1 Å. The 3D representation of the resulting mechanical properties in Fig. 3(b) reveals the same findings for the lattice constants, i.e. the decrease with increasing Ta level.

Finally, the calculated hardness, as illustrated in Fig. 3(d), shows again only a weak substitution dependence. All values are close to the unsubstituted structure.

3.2. Porous materials

LLZO used for typical battery applications is a porous material, whose pores have an influence on the mechanical properties. However, these effects cannot be captured via DFT calculations and therefore the differential effective medium theory is used as a scale bridging description. Generally, this approximation method shows a good agreement with the true effective elastic constants for low pore concentrations. For LLZO, the porosity is typically of the order of 10% [17], and therefore a sufficient accuracy of the predictions can be anticipated. Table 1 shows the resulting effective Young's modulus compared with corresponding experimental values and measured porosity data reported in [17]. We note that we extrapolate the simulated results to 298 K for a realistic comparison to the experiments. For dense, tetragonal LLZO without substitution, the computed and measured Young's moduli match. The unsubstituted, cubic structure results in a slightly smaller value for Young's modulus than the tetragonal counterpart.

As only for selected Ta content experimental elastic constants of pure cubic phase LLZO are available both for dense and porous samples, we restrict the comparisons to these cases. Here it should be mentioned that due to system size constraints, only specific Ta concentrations can be realized in the simulations, and we picked them to be as close as possible to the experimental compositions. The computed and extrapolated dense phase Young's moduli are similar to the experimental values with a deviation of the order of a few GPa, where only $Ta_{0.4}$:LLZO^{exp} is an outlier. For a porosity of around 10% we find a comparable drop of the effective Young's modulus both in simulations and experiments.

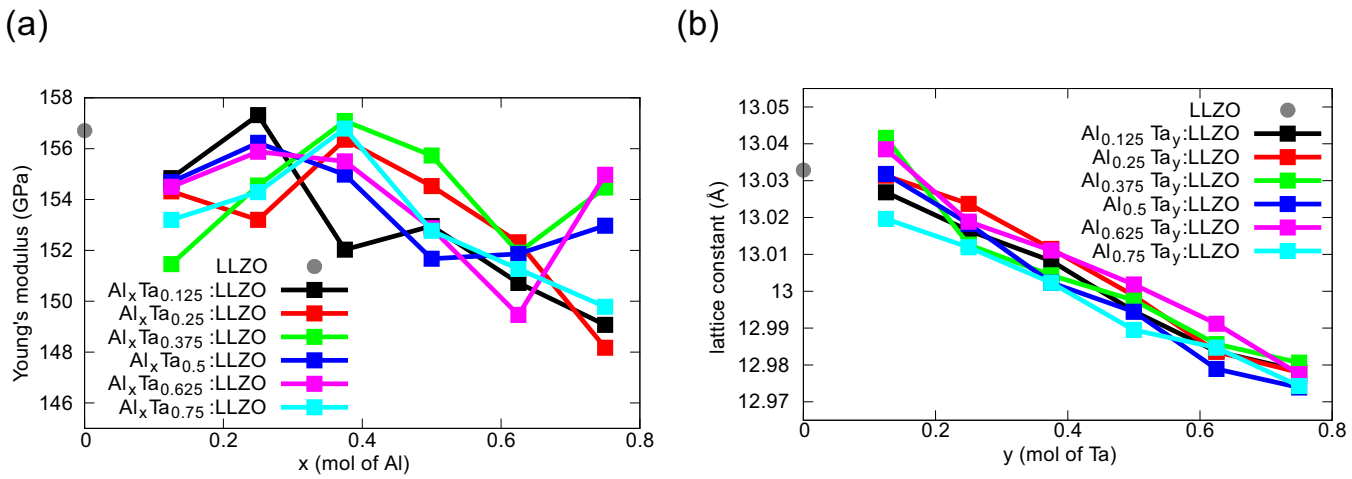

Fig. 2. DFT calculated **(a)** Young's modulus and **(b)** lattice constant for different dopant configurations with **(a)** fixed Al and **(b)** fixed Ta concentrations. The grey point indicates the corresponding value for the unsubstituted structure in each plot. We note that this cubic structure is unstable at ambient temperatures.

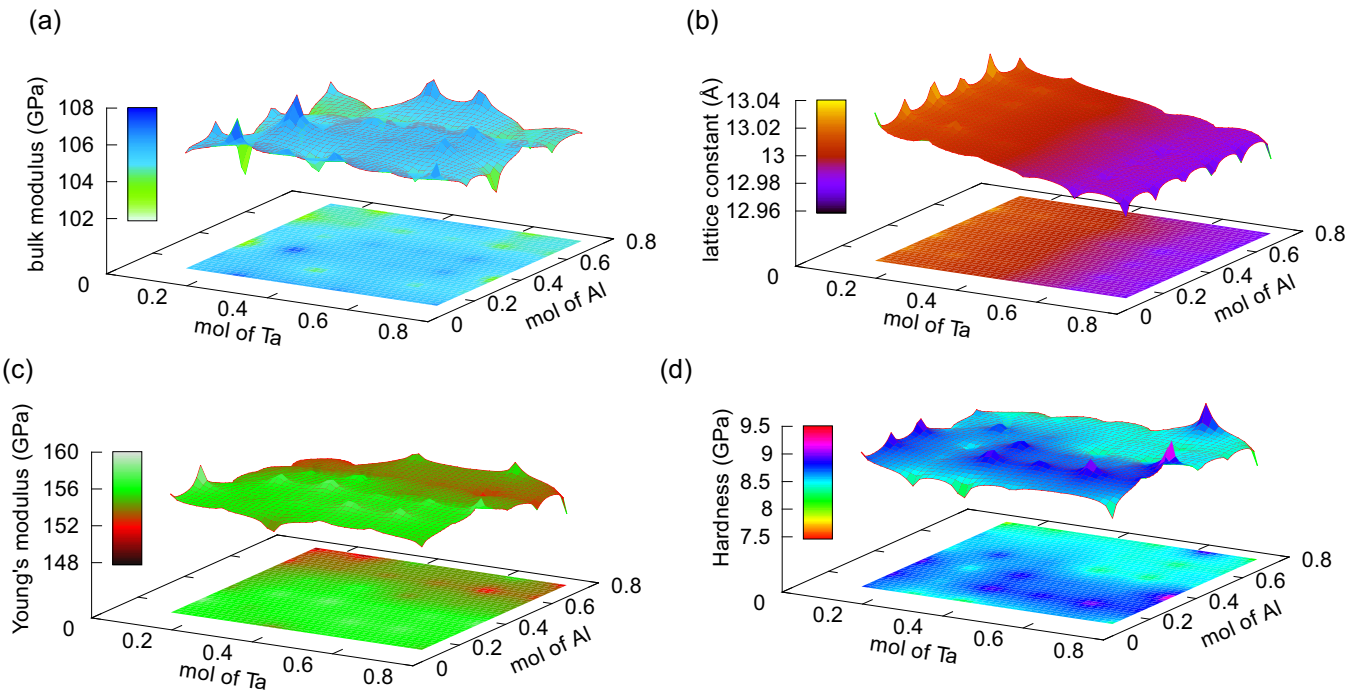

Fig. 3. DFT calculated **(a)** bulk modulus, **(b)** lattice constant, **(c)** Young's modulus and **(d)** hardness for different dopant configurations in a 3D representation. The plots show that the mechanical properties of LLZO are preserved under substitutions with Al and Ta.

Table 1
Verification and comparison of the simulated, extrapolated results (superscript "sim") and experimental quantities (superscript "exp"), which are taken from [17], for single phase materials. All structures are cubic, except two tetragonal, unsubstituted configurations (prefix "t"). For the unsubstituted, tetragonal structure t-LLZO^{sim} the literature value $E = 163.5$ GPa (0 K) from [51] is used. All simulated values are extrapolated to 298 K (reduction of 5%), including the simulation literature value.

Substitution	Porosity	Young's modulus E	effective Young's modulus E_{eff}
in [mol%]	in [%]	in [GPa]	in [GPa]
Un-substituted			
t-LLZO^{exp}	23	156 ± 9	71 ± 3
t-LLZO^{sim}	23	155.3	71.1
LLZO^{sim}	23	148.9	68.1
Ta-substituted			
$Ta_{0.125}$:LLZO^{sim}	8	142.9	112.3
$Ta_{0.2}$:LLZO^{exp}	8	141 ± 2	117 ± 6
$Ta_{0.25}$:LLZO^{sim}	8	144.9	112.8
$Ta_{0.375}$:LLZO^{sim}	9	143.8	108.4
$Ta_{0.4}$:LLZO^{exp}	9	124 ± 3	82 ± 10

Fig. 4 shows the decrease of the ratio E_{eff}/E as function of the void concentration. Different values of the Poisson ratio ν do not affect the behaviour of the elastic modulus decrease. Therefore, the expected LLZO porosity of around 10% leads to a decay by 27% of Young's modulus.

4. Conclusions

Ab initio DFT simulations of garnet structured $Li_7La_3Zr_2O_{12}$ with co-substitutions of Al and Ta are performed and elastic constants and further structural and mechanical properties are calculated.

LLZO shows a pronounced dependence on the Ta substitution level due to the smaller ionic radius of Ta. Also, for the Young's modulus a slight dependency on the Al content is found, while the values for the resulting hardness range in the order of magnitude of the unsubstituted structure. The co-substitutions preserve the structural and mechanical properties, which is important regarding the fabrication of batteries using LLZO.

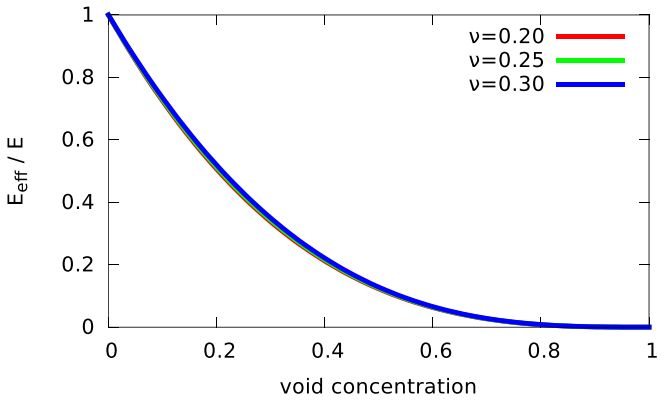

Fig. 4. The decrease of the effective Young's modulus. The resulting ratio of the effective Young's modulus as function of the void concentration for different values of Poisson ratio ν, showing a very weak dependence on ν. We note that for an experimental expected porosity of 10% a decrease of 27% in the elastic quantities is expected.

The differential effective medium theory allows the inclusion of pores and bridges the gap towards application relevant materials. Benchmarking and validation of our simulation results with single substituted experimental values shows a good agreement and allows the usage of our model for consistency checks of experimental and theoretical results. The porosity of LLZO lies at around 10 % and this leads to an expected decay of 27 % for Young's modulus.

Overall, the presented scale bridging calculations lead to reliable predictions of the mechanical properties of doped LLZO. The obtained results can be useful for the optimization of the mechanical behaviour of the solid electrolyte as well as a beneficial mechanical matching to the electrodes to potentially improve electrical contacting and to contribute

to the suppression of dendrite formation.

CRediT authorship contribution statement

Roland Sandt: Conceptualization, Methodology, Software, Validation, Formal analysis, Investigation, Visualization, Writing – original draft, Writing – review & editing. **Yaxue Wang:** Formal analysis, Investigation, Data curation. **Robert Spatschek:** Conceptualization, Writing – review & editing, Supervision, Project administration, Funding acquisition.

Declaration of Competing Interest

The authors declare no competing financial or non-financial interests.

Data availability

Data will be made available on request.

Acknowledgements

This research was funded by the German Federal Ministry of Education and Research (BMBF) via the project Meet HiEnD 3 and the Helmholtz project ZeDaBase. The authors gratefully acknowledge the computing time granted by the JARA Vergabegremium and provided on the JARA Partition part of the supercomputer JURECA at Forschungszentrum Jülich [52].

References

[1] J.-F. Wu, W.K. Pang, V.K. Peterson, L. Wei, X. Guo, Garnet-type fast Li-ion conductors with high ionic conductivities for all-solid-state batteries, ACS Appl. Mater. Interfaces 9 (2017) 12461–12468, https://doi.org/10.1021/acsami.7b00614.

[2] J. Janek, W.G. Zeier, A solid future for battery development, Nat. Energy 1 (2016) 16141, https://doi.org/10.1038/nenergy.2016.141.

[3] Q. Liu, L. Jiang, P. Zheng, J. Sun, C. Liu, J. Chai, X. Li, Y. Zheng, Z. Liu, Recent advantages in stability issues of inorganic solid electrolytes and composite solid electrolytes for all-solid-state batteries, Chem. Rec. 22 (2022), e202200116, https://doi.org/10.1002/tcr.202200116.

[4] C. Wang, K. Fu, S.P. Kammampata, D.W. McOwen, A.J. Samson, L. Zhang, G. T. Hitz, A.M. Nolan, E.D. Wachsman, Y. Mo, V. Thangadurai, L. Hu, Garnet-type solid-state electrolytes: materials, interfaces, and batteries, Chem. Rev. 120 (2020) 4257–4300, https://doi.org/10.1021/acs.chemrev.9b00427.

[5] S. Kim, J.-S. Kim, L. Miara, Y. Wang, S.-K. Jung, S.Y. Park, Z. Song, H. Kim, M. Badding, J. Chang, V. Roev, G. Yoon, R. Kim, J.-H. Kim, K. Yoon, D. Im, K. Kang, High-energy and durable lithium metal batteries using garnet-type solid electrolytes with tailored lithium-metal compatibility, Nat. Commun. 13 (2022) 1883, https://doi.org/10.1038/s41467-022-29531-x.

[6] R. Koerver, W. Zhang, L. de Biasi, S. Schweidler, A.O. Kondrakov, S. Kolling, T. Brezesinski, P. Hartmann, W.G. Zeier, J. Janek, Chemo-mechanical expansion of lithium electrode materials - on the route to mechanically optimized all-solid-state batteries, Energy Environ. Sci. 11 (2018) 2142, https://doi.org/10.1039/C8EE00907D.

[7] G. McConohy, X. Xu, T. Cui, E. Barks, S. Wang, E. Kaeli, C. Melamed, X.W. Gu, W. C. Chueh, Mechanical regulation of lithium intrusion probability in garnet solid electrolytes, Nat. Energy (2023), https://doi.org/10.1038/s41560-022-01186-4.

[8] Y. Chen, Y. Jiang, S.-S. Chi, H.J. Woo, K. Yu, J. Ma, J. Wang, C. Wang, Y. Deng, Understanding the lithium dendrites growth in garnet-based solid-state lithium metal batteries, J. Power Sources 521 (2022) 230921, https://doi.org/10.1016/j.jpowsour.2021.230921.

[9] S. Fu, Y. Arinicheva, C. Hüter, M. Finsterbusch, R. Spatschek, Grain boundary characterization and potential percolation of the solid electrolyte LLZO, Batteries 9 (2023) 222, https://doi.org/10.3390/batteries9040222.

[10] C.D. Fincher, C.E. Athanasiou, C. Gilgenbach, M. Wang, B.W. Sheldon, W.C. Carter, Y.-M. Chiang, Controlling dendrite propagation in solid-state batteries with engineered stress, Joule 6 (2022) 2794–2809, https://doi.org/10.1016/j.joule.2022.10.011.

[11] R. Murugan, V. Thangadurai, W. Weppner, Fast Lithium ion conduction in garnet-type $Li_7La_3Zr_2O_{12}$, Angew. Chem. Int. Ed. 46 (2007) 7778–7781, https://doi.org/10.1002/anie.200701144.

[12] C.A. Geiger, E. Alekseev, B. Lazic, M. Fisch, T. Armbruster, R. Langner, M. Fechtelkord, N. Kim, T. Pettke, W. Weppner, Crystal chemistry and stability of "$Li_7La_3Zr_2O_{12}$" garnet: afast Lithium-ion conductor, Inorg. Chem. 50 (2011) 1089–1097, https://doi.org/10.1021/ic101914e.

[13] E. Enkhbayar, J.H. Kim, Study of Codoping effects of Ta^{5+} and Ga^{3+} on garnet $Li_7La_3Zr_2O_{12}$, ACS Omega 7 (2022) 47265–47273, https://doi.org/10.1021/acsomega.2c06544.

[14] L.J. Miara, S.P. Ong, Y. Mo, W.D. Richards, Y. Park, J.-M. Lee, H.S. Lee, G. Ceder, Effect of Rb and Tadoping on the ionic conductivity and stability of the garnet Li_{7+2x-y} $(La_{3-x}Rb_x)$ $(Zr_{2-y}Ta_y)$ O_{12} $(0 \leq x \leq 0.375, 0 \leq y \leq 1)$ superionic conductor: afirst principles investigation, Chem. Mater. 25 (2013) 3048–3055, https://doi.org/10.1021/cm401232r.

[15] H. Buschmann, J. Dölle, S. Berendts, A. Kuhn, P. Bottke, M. Wilkening, P. Heitjans, A. Senyshyn, H. Ehrenberg, A. Lotnyk, V. Duppel, L. Kienle, J. Janek, Structure and dynamics of the fast lithium ion conductor "$Li_7La_3Zr_2O_{12}$", Phys. Chem. Chem. Phys. 13 (2011) 19378–19392, https://doi.org/10.1039/C1CP22108F.

[16] A.-N. Wang, J.F. Nonemacher, G. Yan, M. Finsterbusch, J. Malzbender, M. Krüger, Mechanical properties of the solid electrolyte Al-substituted $Li_7La_3Zr_2O_{12}$ (LLZO) by utilizing micro-pillar indentation splitting test, J. Eur. Ceram. Soc. 38 (2018) 3201–3209, https://doi.org/10.1016/j.jeurceramsoc.2018.02.032.

[17] J.F. Nonemacher, C. Hüter, H. Zheng, J. Malzbender, M. Krüger, R. Spatschek, M. Finsterbusch, Microstructure and properties investigation of garnet structured $Li_7La_3Zr_2O_{12}$ as electrolyte for all-solid-state batteries, Solid State Ionics 321 (2018) 126–134, https://doi.org/10.1016/j.ssi.2018.04.016.

[18] A. Kuhn, J.-Y. Choi, L. Robben, F. Tietz, M. Wilkening, P. Heitjans, Li ion dynamics in Al-doped garnet-type $Li_7La_3Zr_2O_{12}$crystallizing with cubic symmetry, Z. Phys. Chem. 226 (2012) 525–537, https://doi.org/10.1524/zpch.2012.0250.

[19] Y. Wang, W. Lai, High ionic conductivity Lithium garnet oxides of $Li_{7-x}La_3Zr_{2-x}Ta_xO_{12}$compositions, Electrochem. Solid-State Lett. 15 (2012) A68, https://doi.org/10.1149/2.024205esl.

[20] D.O. Shin, K. Oh, K.M. Kim, K.-Y. Park, B. Lee, Y.-G. Lee, K. Kang, Synergistic multi-doping effects on the $Li_7La_3Zr_2O_{12}$ solid electrolyte for fast lithium ion conduction, Sci. Rep. 5 (2015) 18053, https://doi.org/10.1038/srep18053.

[21] S. Yu, R.D. Schmidt, R. Garcia-Mendez, E. Herbert, N.J. Dudney, J.B. Wolfenstine, J. Sakamoto, D.J. Siegel, Elastic properties of the solid electrolyte $Li_7La_3Zr_2O_{12}$ (LLZO), Chem. Mater. 28 (2016) 197–206, https://doi.org/10.1021/acs.chemmater.5b03854.

[22] B. Celik, R. Sandt, L.C. Pereira dos Santos, R. Spatschek, Prediction of battery cycle life using early-cycle data, machine learning and data management, Batteries 8 (2022) 266, https://doi.org/10.3390/batteries8120266.

[23] O.I. Abiodun, A. Jantan, A.E. Omolara, K.V. Dada, N.A. Mohamed, H. Arshad, State-of-the-art in artificial neural network applications: a survey, Heliyon 4 (2018), e00938, https://doi.org/10.1016/j.heliyon.2018.e00938.

[24] D. Yang, Y. Wang, R. Pan, R. Chen, Z. Chen, A neural network based state-of-health estimation of lithium-ion battery in electric vehicles, Energy Procedia 105 (2017) 2059–2064, https://doi.org/10.1016/j.egypro.2017.03.583.

[25] H. Wen, C. Huang, S. Guo, The application of convolutional neural networks (CNNs) to recognize defects in 3D-printed parts, Materials 14 (2021) 2575, https://doi.org/10.3390/ma14102575.

[26] R. Jinnouchi, J. Lahnsteiner, F. Karsai, G. Kresse, M. Bokdam, Phase transitions of hybrid perovskites simulated by machine-learning force fields trained on the Fly with Bayesian inference, Phys. Rev. Lett. 122 (2019) 225701, https://doi.org/10.1103/PhysRevLett.122.225701.

[27] M. Bogojeski, L. Vogt-Maranto, M.E. Tuckerman, K.-R. Müller, K. Burke, Quantum chemical accuracy from density functional approximations via machine learning, Nat. Commun. 11 (2020) 5223, https://doi.org/10.1038/s41467-020-19093-1.

[28] G. Hegde, R.C. Bowen, Machine-learned approximations to density functional theory Hamiltonians, Sci. Rep. 7 (2017) 42669, https://doi.org/10.1038/srep42669.

[29] M. Fronzi, R.D. Amos, R. Kobayashi, N. Matsumura, K. Watanabe, R.K. Morizawa, Evaluation of machine learning interatomic potentials for the properties of gold nanoparticles, Nanomaterials 12 (2022) 3891, https://doi.org/10.3390/nano12213891.

[30] M. Hodapp, A. Shapeev, Machine-learning potentials enable predictive and tractable high-throughput screening of random alloys, Phys. Rev. Mater. 5 (2021) 113802, https://doi.org/10.1103/PhysRevMaterials.5.113802.

[31] R. Spatschek, C. Gugenberger, E.A. Brener, Effective elastic moduli in solids with high density of cracks, Phys. Rev. B 80 (2009) 144106, https://doi.org/10.1103/PhysRevB.80.144106.

[32] A.R. Day, K.A. Snyder, E.J. Garboczi, M.F. Thorpe, The elastic moduli of a sheet containing circular holes, J. Mech. Phys. Solids 40 (1992) 1031–1051, https://doi.org/10.1016/0022-5096(92)90061-6.

[33] G. Kresse, J. Furthmüller, Efficient iterative schemes for *ab initio* total-energy calculations using a plane-wave basis set, Phys. Rev. B 54 (1996) 11169, https://doi.org/10.1103/PhysRevB.54.11169.

[34] P.E. Blöchl, Projector augmented-wave method, Phys. Rev. B 50 (1994) 17953, https://doi.org/10.1103/PhysRevB.50.17953.

[35] G. Kresse, D. Joubert, From ultrasoft pseudopotentials to the projector augmented-wave method, Phys. Rev. B 59 (1999) 1758, https://doi.org/10.1103/PhysRevB.59.1758.

[36] J.P. Perdew, K. Burke, M. Ernzerhof, Generalized gradient approximation made simple, Phys. Rev. Lett. 77 (1996) 3865, https://doi.org/10.1103/PhysRevLett.77.3865.

[37] P.P. Ewald, Die Berechnung optischer und elektrostatischer Gitterpotentiale, Ann. Phys. 369 (1921) 253–287, https://doi.org/10.1002/andp.19213690304.

[38] S.P. Ong, W.D. Richards, A. Jain, G. Hautier, M. Kocher, S. Cholia, D. Gunter, V. L. Chevrier, K.A. Persson, G. Ceder, Python materials genomics (pymatgen): a robust, open-source python library for materials analysis, Comput. Mater. Sci. 68 (2012) 314–319, https://doi.org/10.1016/j.commatsci.2012.10.028.

[39] H.J. Monkhorst, J.D. Pack, Special points for Brillouin-zone integrations, Phys. Rev. B 13 (1976) 5188, https://doi.org/10.1103/PhysRevB.13.5188.
[40] P. Söderlind, O. Eriksson, J.M. Wills, A.M. Boring, Theory of elastic constants of cubic transition metals and alloys, Phys. Rev. B 48 (1993) 5844–5851, https://doi.org/10.1103/PhysRevB.48.5844.
[41] F.D. Murnaghan, The compressibility of media under extreme pressures, Proc. Natl. Acad. Sci. U. S. A. 30 (1944) 244–247, https://doi.org/10.1073/pnas.30.9.244.
[42] F. Birch, Finite elastic strain of cubic crystals, Phys. Rev. 71 (1947) 809–824, https://doi.org/10.1103/PhysRev.71.809.
[43] C. Hüter, M. Friák, M. Weikamp, J. Neugebauer, N. Goldenfeld, B. Svendsen, R. Spatschek, Nonlinear elastic effects in phase field crystal and amplitude equations: comparison to *ab initio* simulations of bcc metals and graphene, Phys. Rev. B 93 (2016) 214105, https://doi.org/10.1103/PhysRevB.93.214105.
[44] X. Li, J. Zhao, J. Xu, Mechanical properties of bcc Fe-Cr alloys by first-principles simulations, Front. Phys. 7 (2012) 360–365, https://doi.org/10.1007/s11467-011-0193-0.
[45] M. Jamal, S. Jalalil Asadabadi, I. Ahmad, H.A. Rahnamaye Aliabad, Elastic constants of cubic crystals, Comput. Mater. Sci. 95 (2014) 592–599, https://doi.org/10.1016/j.commatsci.2014.08.027.
[46] Z. Hashin, S. Shtrikman, A variational approach to the theory of the elastic behaviour of polycrystals, J. Mech. Phys. Solids 10 (1962) 343–352, https://doi.org/10.1016/0022-5096(62)90005-4.
[47] Z. Hashin, S. Shtrikman, A variational approach to the theory of the elastic behaviour of multiphase materials, J. Mech. Phys. Solids 11 (1963) 127–140, https://doi.org/10.1016/0022-5096(63)90060-7.
[48] X.-Q. Chen, H. Niu, D. Li, Y. Li, Modeling hardness of polycrystalline materials and bulk metallic glasses, Intermetallics 19 (2011) 1275–1281, https://doi.org/10.1016/j.intermet.2011.03.026.
[49] D.A.G. Bruggeman, Berechnung verschiedener physikalischer Konstanten von heterogenen Substanzen. I. Dielektrizitätskonstanten und Leitfähigkeiten der Mischkörper aus isotropen Substanzen, Ann. Phys. 416 (1935) 636–664, https://doi.org/10.1002/andp.19354160705.
[50] S. Nemat-Nasser, M. Hori, Micromechanics: Overall Properties of Heterogeneous Materials, 2nd ed., North-Holland, Amsterdam, 1998.
[51] R. Maphoto, M. Masedi, P. Ngoepe, R. Ledwaba, First-principles study on structural, mechanical and electronic properties of $Li_7La_3Zr_2O_{12}$ solid electrolyte, Suid-Afrikaans Tydskrif vir Natuurwetenskap en Tegnologie South African J. Sci. Technol. 40 (2022) 12–15, https://doi.org/10.36303/SATNT.2021cosaami.03.
[52] Jülich Supercomputing Centre, JURECA: Data Centric and Booster Modules implementing the Modular Supercomputing Architecture at Jülich Supercomputing Centre, J. Large-scale Res. Facilit. 7 (2018) A182, https://doi.org/10.17815/jlsrf-7-182.

scientific reports

Check for updates

OPEN

Quantum annealing for microstructure equilibration with long-range elastic interactions

Roland Sandt[1]✉, Yann Le Bouar[2] & Robert Spatschek[1,3]

We demonstrate the use and benefits of quantum annealing approaches for the determination of equilibrated microstructures in shape memory alloys and other materials with long-range elastic interaction between coherent grains and their different martensite variants and phases. After a one dimensional illustration of the general approach, which requires to formulate the energy of the system in terms of an Ising Hamiltonian, we use distant dependent elastic interactions between grains to predict the variant selection for different transformation eigenstrains. The results and performance of the computations are compared to classical algorithms, demonstrating that the new approach can lead to a significant acceleration of the simulations. Beyond a discretization using simple cuboidal elements, also a direct representation of arbitrary microstructures is possible, allowing fast simulations with currently up to several thousand grains.

The modeling of microstructures is an important approach to the understanding, improvement and development of new materials for various applications. However, as mechanisms at different length and time scales are intimately linked, such descriptions and model implementations are typically challenging and require massive computational resources. Although phase field simulation approaches – the most prominent method for predicting microstructure evolution – strongly benefit from developments like the thin interface limit[1,2], nondiagonal phase field models[3,4] and sharp phase field approaches[5], simulations containing large microstructural domains to obtain predictions with a certain statistical significance are rare, strongly limited by the available (super-) computer resources and their associated costs and energy consumption. Despite the enormous progress in this research field and the extended use of parallel computers and graphics cards for the simulations, limitations of the computational techniques remain a serious thread to the basic scientific progress and applied research.

One of the striking questions, which arises at the horizon of materials science modeling is how quantum computing will potentially change the simulation landscape in the future. However, at present a general-purpose quantum computer of sufficient size is not yet available. In the meantime, a technology known as quantum annealing (QA)[6–10] has emerged and is available on several sites worldwide. The use of such machines differs significantly from traditional gate based computers and therefore currently only specific problems can be handled by quantum annealers[11]. The concept of a quantum annealer is that its qubits are initialized in a well defined state which is described by a Hamiltonian with a unique ground state[12]. During the operation at cryogenic temperatures, this Hamiltonian is changed adiabatically such that the ground state converts into the one of the final, desired Hamiltonian[12,13], and therefore allows to perform global energy minimization computations efficiently. The structure of these Hamiltonians is a binary quadratic model, which can be expressed in terms of a quadratic unconstrained binary optimization or equivalently through an Ising model[11]. Due to this specific structure, so far, materials science related applications of this technology are still rare. Instead, actual research focuses mainly on the benchmarking and performance tests of quantum annealing compared to classical approaches[14–16].

Some first applications in the field of biology and traffic research in the sense of optimization problems have been developed recently. Here, quantum annealing enables the efficient analysis of transcription factors in gene expression with combined machine learning algorithms[17], identification of conformations of lattice protein models[18] and their folding[19], detection of tree cover in aerial images[20], real-world traffic flow optimization problems[21] or control of automated guided vehicles[22]. However, the usage of quantum annealing in materials science is not widespread and few publications correspond to phase transitions in the transverse field Ising model[23], the investigation of critical phenomena in frustrated magnets via the Shastry-Sutherland Ising model[24], Monte-Carlo sampling[25] and the automated materials design of metamaterials[26]. The purpose of the present paper

[1]Structure and Function of Materials, Institute of Energy and Climate Research, Forschungszentrum Jülich GmbH, 52425 Jülich, Germany. [2]Université Paris-Saclay, ONERA, CNRS, Laboratoire d'Etude des Microstructures, 92320 Châtillon, France. [3]JARA-ENERGY, 52425 Jülich, Germany. ✉email: r.sandt@fz-juelich.de

is therefore to demonstrate that this novel technology can indeed lead to completely new possibilities beyond the existing and commonly used descriptions for the modeling of microstructures.

In order to be as explicit and illustrative as possible, we demonstrate here the case of coherent solid state transformations involving austenitic and martensitic phases, where the latter are allowed to appear in different variants. Such transitions play a role for shape memory alloys like NiTi, which can be deformed easily at low temperatures, but heating to higher temperatures lets the material return to its previous, trained shape[27]. The modelling and mapping of shape memory alloys to spin glass systems was previously established in several studies[28–31] and can here be exploited for QA applications. In the following we will mainly stick to the terminology of the shape memory alloys but emphasize that similar approaches can be used to model e.g. the transformation and deformation behavior in steels, ferroelastic materials, as well as phase changes in solid electrolytes for rechargeable batteries. The particular aspect that plays a central role here are the anisotropic long-range elastic interactions, which are common for solid state transformations[32], and therefore the ground state configuration does not only depend on phase concentrations and fractions, but also on the detailed microstructural arrangement of phases and grains. In a typical phase field simulation[33], the microstructural evolution is solved together with the relaxation of the mechanical deformations in the spirit of a continuum description, which leads to very long simulation times. Here, we show that the separation of the discrete degrees of freedom for the variant distribution of martensitic phases from the continuous development of the microstructure and the QA treatment allow to drastically increase the performance of the computations and therefore to simulate significantly larger, application relevant systems compared to existing approaches.

Results

One-dimensional model. For a simplified 1D model we consider only a "martensitic" phase which is assumed to exist in two different variants. Hence the microstructure consists of a line of grains of these variants, as depicted in the inset of Fig. 1a. To be explicit, we assume that both variants have a stress free strain (eigenstrain), which leads to a shear deformation relative to the austenitic mother phase, and denote these variants by state variables $s_i = \pm 1$. As in the end we will map the description to a one-dimensional Ising model, we also use here the terminology of "spins" with two possible alignments in the spirit of a magnetic model. As each of the variants leads to a shearing of the cell, we get an overall stress free deformation of this line (compared to the shear strain free austenite), depending on the spin configuration. We assume that all grains have the same height d, the same elastic constants, and opposite shear eigenstrain $\pm\varepsilon_0$. As one can readily see from the inset of Fig. 1a, the stress free equilibrium position of the top grain x_0 depends only on the number of variants N_+ with orientation $s_i = +1$ and N_- with $s_i = -1$, but not on the individual arrangement, which is a particularity of the simplified 1D model and the chosen eigenstrain. Hence, for a fixed number $N = N_+ + N_-$ spins in a row, the macroscopic stress free strain is $\bar{\varepsilon} = (N_+ - N_-)\varepsilon_0/N$, which leads to $x_0 = Nd\bar{\varepsilon}$. If an external deformation is enforced, i.e. $x \neq x_0$ the elastic energy is $F_{el} = \mu_{\text{eff}}(x - x_0)^2$ with an effective shear modulus μ_{eff}. Obviously, the elastic energy is minimized if the spin configuration is such that $x = x_0$, which implies $(N_+ - N_-)_{\min} = x/\varepsilon_0 d$, up to the point of saturation, where all spins are aligned. This expression serves as reference for the comparison with the numerical minimization approaches below. We note that we neglected at this stage the discrete nature of the variants, which means that the integer value $N_+ - N_-$ should be as close as possible to the continuum value $(N_+ - N_-)_{\min}$ above. Although the energy in the simple 1D model does not

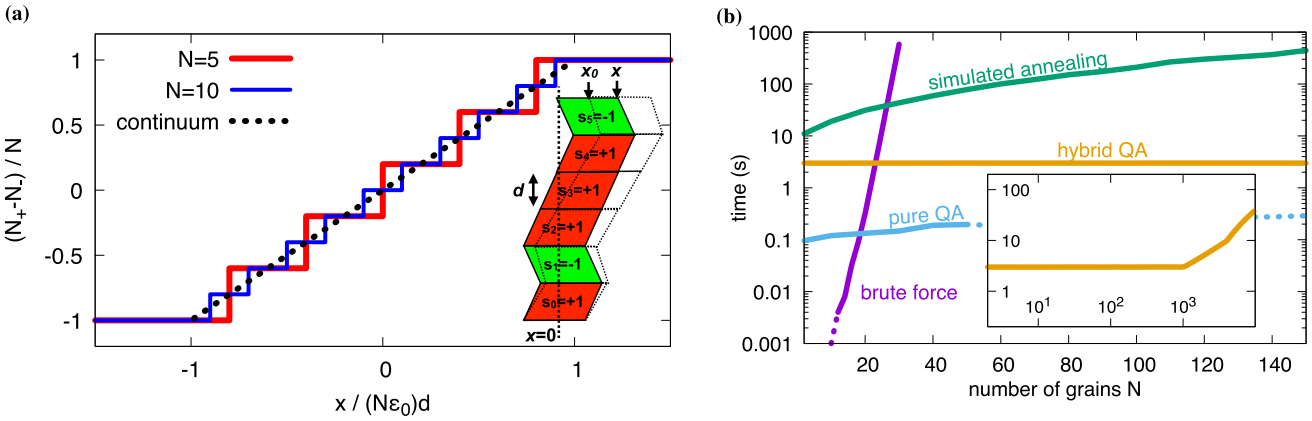

Figure 1. Results of the one-dimensional model comparing different numerical and analytical methods. (**a**) Mean variant orientation $(N_+ - N_-)/N$ as function of the displacement $x/dN\varepsilon_0$. Comparison between the results obtained by numerical minimization (solid lines) versus the analytical theory for an infinite and continuous system (dashed line). For large displacement, all "spins" are aligned and therefore the "magnetization" saturates. The inset shows a sketch of the one-dimensional arrangement of martensite variants $s_i = +1$ (red) and $s_i = -1$ (green). The bottom row is fixed to position $x = 0$, whereas the top grain has a mean position x_0 in the stress free state. If an additional external stress or strain is applied, the top layer is moved to position x, and the entire microstructure is sheared to the dashed configuration. (**b**) Elapsed computation time as a function of the number of grains. Different methods and algorithms are compared. Dashed parts of the QA curve belong to the regime of chain breaks. For large system sizes, only the hybrid quantum annealing approach remains feasible, showing an almost constant computing time need for less than 1000 spin variables (inset).

depend on the arrangement of the variants but only on the total numbers N_+ and $N_- = N - N_+$, we formulate the model here on the level of the individual "spins" s_i for the later extension towards higher dimensions and the use of the quantum annealer. Hence we get $N_+ - N_- = \sum_i s_i$. Inserting this into the elastic energy expression yields $F_{\mathrm{el}} = \mu_{\mathrm{eff}}\varepsilon_0^2 d^2 \sum_{i,j} s_i s_j - 2\mu_{\mathrm{eff}} x\varepsilon_0 d \sum_i s_i + \mu_{\mathrm{eff}} x^2$, where the summations run over all spins. For the implementation on a quantum annealer, we need to bring this to the Ising form of a Hamiltonian H with

$$H = \sum_i h_i s_i + \sum_{i<j} J_{ij} s_i s_j + H_0, \tag{1}$$

where the first term corresponds to the interaction with an external magnetic field h_i and the second term to a spin-spin interaction, which favors ferromagnetic (antiferromagnetic) ordering in case that the coupling constant J_{ij} is negative (positive). The last, spin-independent term H_0 is only an irrelevant additive constant. From the comparison of the two above expressions we identify $h_i = -2\mu_{\mathrm{eff}} x\varepsilon_0 d$ and $J_{ij} = 2\mu_{\mathrm{eff}}\varepsilon_0^2 d^2$. First, we note that the external deformation is here analogous to the magnetic field in the Ising description. Second, the spin-spin interaction term J_{ij} is positive, hence favoring "antiferromagnetic ordering". Also, this term is independent of the spin numbers i, j, which means that this interaction does not depend on the distance between the grains. In other words, the elastic interaction depends only on the averaged "magnetization" $N_+ - N_-$, which implies a mean field interaction.

The goal of the formulation is to minimize the elastic energy and to find the optimal spin or variant configuration $\{s_i\}$. To this end, we use three different numerical approaches (see methods section), and the results are compared to the analytical solution above: First, a brute force approach iterates over all spin configurations to find the energetic minimum exactly, second we use simulated annealing as probabilistic ground state finder, and finally the quantum annealing approach. Fig. 1a shows the resulting "magnetization" $(N_+ - N_-)/N$, i.e. the average variant orientation, as function of applied displacement $x/dN\varepsilon_0$, which corresponds to the magnetic field in the Ising model.

As expected, the results agree with the analytical theory up to the aforementioned discretization effect, which becomes less pronounced for large grain numbers. For high displacements saturation sets in when all variants are de-twinned, which means that all spins are either in the state $+1$ or -1. We note that for the investigated number of spins all used algorithms lead to the same energy minimum, which confirms that also the probabilistic approaches indeed find the global minimum states.

Fig. 1b shows the required computation time for the different methods and algorithms as a function of the number of grains N. All conventional algorithm implementations are based on single core computations without parallelization and are mainly shown for a qualitative comparison, as the focus of the investigations is on the quantum annealing approach. For the latter, we use quantum processing unit (QPU) implementations up to the highest possible number of spins (typically $N \approx 170$ for the Pegasus architecture[34] of a D-Wave machine). The brute force approach, where iterations over all spin configurations are run, has the highest computation time. Even at small spin systems of around $N \approx 40$ the elapsed user time was too large for practical applications due to the simulation time scaling $\sim \mathcal{O}(2^N)$. The pure quantum annealing method produces the fastest results and ends up with an almost constant elapsed QPU access time. Overall, the computations for $N \approx 150$ are roughly three orders of magnitude faster than for the other classical approaches. Beyond around $N \approx 50$ spins, so called chain breaks[35] occur occasionally. They result from the need to encode strongly coupled spins as a single logical spin. Ideally, these spins should represent the same state as the individual spins, but in practise this identity can be violated. To avoid this issue and to simulate even larger systems, which are essential for higher dimensional modeling in the following sections, hybrid classical and quantum annealing approaches can be used, which combine pure QA with conventional minimization approaches[36]. The numerical results in Fig. 1b show an increase of the computation time of the hybrid solver compared to the pure QA, but the relative acceleration compared to the classical algorithms becomes even more striking. For the hybrid solver, the elapsed computation time is essentially independent of the number of spin variables and increases only beyond 10^3 grains to several seconds. Altogether, the hybrid QA is clearly the fastest approach for large grain numbers and is therefore used in the following two-dimensional simulations.

Transformations in higher dimensions. For the determination of the linear elastic energy beyond one dimension, we consider coherent precipitates of different variants which form inside the matrix. In this way, the entire material can be considered to consist of small entities (in the following denoted as grains), which can be in one of the different martensitic states. The simplest possible (cartesian) discretization is to use small cuboidal grains with edge length a. All grains are assumed to be coherent (the elastic displacements and tractions are continuous at the interfaces between the grains), and we use homogeneous elasticity, i.e. we ignore differences in the elastic constants between the different phases or variants. This has the consequence that the elastic energy reduces to combinations of pairwise interactions between all grains[37].

For demonstrational purposes we perform here two-dimensional simulations in a plane strain setup, but a transfer to three dimensions is straightforward. In particular, the annealer part does not depend on the dimensionality of the description. The qualitatively new aspect beyond 1D is the appearance of distance and orientation dependent "spin-spin" interactions, which decay only slowly with the distance between the grains, and therefore leads to fully populated matrices J_{ij}. As it turns out that an accurate determination of the elastic interaction energy is essential for a precise prediction of the equilibrium microstructure, we use Fourier transformation approaches with periodic boundary conditions as outlined in the methods section. As boundary conditions, we use either vanishing average stress in the periodic volume V, $\langle\sigma_{ij}\rangle = \frac{1}{V}\int \sigma_{ij}(\mathbf{r})\, d\mathbf{r} = 0$, or, similarly to the 1D description, a given average strain $\langle\varepsilon_{ij}\rangle$. We employ in the following for simplicity isotropic elasticity, which is e.g. described by the Lamé coefficient λ and the shear modulus μ, i.e. the stress-strain relationship reads

$\sigma_{ij} = 2\mu(\varepsilon_{ij} - \varepsilon_{ij}^{(0)}) + \lambda\delta_{ij}(\varepsilon_{kk} - \varepsilon_{kk}^{(0)})$, where implicit summation over repeated indices is used. The position dependent eigenstrain $\varepsilon_{ij}^{(0)}(\mathbf{r})$ is known for a given microstructure with fixed phase dependent stress free strains (relative to the austenitic mother phase), $\varepsilon_{ij}^{(0)}(\mathbf{r}) = \theta(\mathbf{r})\varepsilon_{ij}^{0}$, where the indicator function θ is zero in the austenite and either $+1$ or -1 in the two considered martensite variants. For a given microstructure, the elastic energy can then be computed in reciprocal space, as shown in the methods section. For the formulation as Ising model we discretize our microstructure using small non-overlapping cuboidal grains as discussed above and assign a "spin" s_i to each of them like before, such that the indicator field becomes a superposition $\theta(\mathbf{r}) = \sum_i s_i\theta_i(\mathbf{r})$, where θ_i equals one inside the corresponding square and is zero outside. Therefore, the elastic energy decomposes into pairwise interactions (for $i \neq j$) and self-energy terms (for $i = j$)

$$E_{i,j} = s_i s_j \frac{1}{2V} \int d\mathbf{r} \int d\mathbf{r}' B(\mathbf{r} - \mathbf{r}')\theta_i(\mathbf{r})\theta_j(\mathbf{r}'), \tag{2}$$

where the integral kernel $B(\mathbf{r})$ is defined through the inverse of the elastic Green's function. Hence, it is sufficient to perform the Fourier transform energy calculations for all pairs of the same martensite variant $s_i = s_j = 1$ on the discrete lattice sites in the volume V; for periodic boundary conditions and identical grain shapes, it is sufficient to calculate the elastic interaction energy between a reference grain and all the other grains, due to translation invariance. In case of fixed average strain boundary conditions, an additional homogeneous term appears (see methods section), contributing both to the spin-spin interaction J_{ij} as well as to the magnetic field term h_i, which is absent for zero average stress boundary conditions. The resulting fully populated matrix of coupling constants with both positive and negative entries has similarities to spin glass systems with random couplings, which have been investigated in the literature with conventional approaches, see e.g.[38].

For the simplest case that the eigenstrain is purely dilatational and isotropic the Bitter-Crum theorem applies and the total energy depends only on the volume fraction of the martensite variant, where no interaction between the grains is present and only a self energy term remains[39].

For a nontrivial elastic interaction and the link to the previous 1D description, we consider a shear transformation strain with $\varepsilon_{xy}^{0} = \varepsilon_{yx}^{0} = \varepsilon_0$, where all other components vanish. In this case, we obtain a distance and orientation dependent interaction as depicted in Fig. 2a, which is computed here for the case of vanishing average stress, $\langle\sigma_{ik}\rangle = 0$. Here and in the following parts the Poisson ratio is chosen as $\nu = 1/4$ (i.e. $\lambda = \mu$).

The interaction energy is obtained by subtracting the elastic self energies E_{self} for each of the two (isolated) martensite grains inside the austenitic matrix from the total elastic energy E_{el} of the two-grain arrangement, i.e. $E_{\text{int}} = E_{\text{el}} - 2E_{\text{self}}$, to normalize the interaction energy such that it decays to zero for large grain separations. For short distances, a transition between attraction and repulsion is found for the $\langle 100\rangle$ direction, whereas a purely repulsive interaction results for the diagonal $\langle 110\rangle$ directions. Due to the periodic boundary conditions, the result depends on the system size $V = L_x \times L_y$, as the grains also interact with their periodic images, hence $r \ll L_x, L_y$ is required to observe the decay of the interaction.

We note that in two dimensions the interaction energy decays asymptotically as r^{-2}, whereas in three dimensions it scales as r^{-3} in large systems, which follows from the elastic Green's function[40]. For the quantum annealer implementation, the interaction energies are needed only for the discrete lattice points (symbols on the curves). Although the decay of the elastic interaction may suggest to cut it off beyond a certain distance in real space, it turns out that such an approach is inappropriate, as it leads in the end to invalid equilibrium microstructures, and it is therefore essential to keep all interaction terms J_{ij} with high precision to avoid spurious effects. We note that the formulation on the quantum annealer does not depend on the dimensionality, therefore the scaling plot in Fig. 1b applies here as well.

Based on the calculation of the elastic interactions, we obtain from the Ising model implementation on the quantum annealer with hybrid solver stripe patterns in $\langle 100\rangle$ direction as equilibrium structures. These patterns

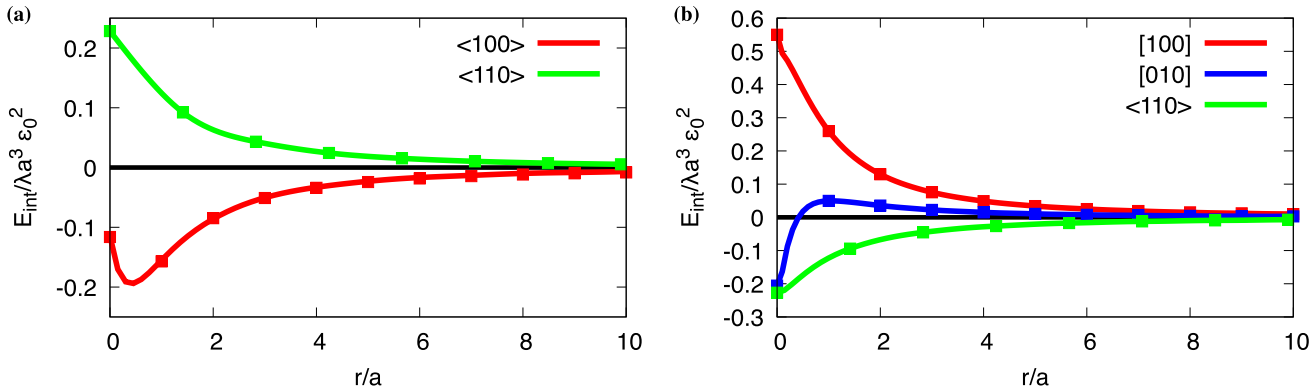

Figure 2. Interaction energies of two grains of equal variant type ($\mathbf{s_i} = \mathbf{s_j}$). Interaction energies in the case of (**a**) shear eigenstrain and vanishing average stress and (**b**) tetragonal eigenstrain. The interaction energy per length is given in units of $\lambda a^3 \varepsilon_0^2$, and the computations were done using a system size of $L_x/a = L_y/a = 50$, where a is the edge length of the grains. At distance $r/a = 0$ the grains touch each other. The symbols on the continuous curves indicate the information for the interaction at discrete lattice sites, which is actually used in the annealer simulations.

are irregular in the sense that the widths of the stripes are not uniform. This is in analogy to the 1D model, which was discussed above, where we found that the arrangement of the two variants is not determined. This coincidence, which is physically expected, is nontrivial from the model formulation, as (i) in the 1D model we had a distance independent interaction in the discretized model, where here the interaction is significantly more complex, but adds up to the same effective descriptions for the periodic arrangement; (ii) a rotation of the pattern by 90 degree is possible and sometimes obtained from the optimal configuration due to the discrete rotational symmetry; (iii) the fixing of the average stress compared to the given average strain in the 1D formulation can lead to unequal distributions of the different variants. In particular, for the presently considered absence of an external strain (implying a vanishing magnetic field in the Ising terminology), there is no constraint of the sort $\langle s_i \rangle = 0$ for the average spin alignment. All stripe configurations are energetically equivalent, which includes the possibility of a single variant configuration. These results therefore confirm simultaneously the accuracy of the elastic interaction calculation with the pairwise decomposition as well as the ability of the quantum annealer to identify the true ground state configurations.

As next example, we use a tetragonal eigenstrain with the only nonvanishing components $\varepsilon^0_{xx} = -\varepsilon^0_{yy} = \varepsilon^0_{zz} = \varepsilon_0$. First, we consider again the situation with vanishing average stress, $\langle \sigma_{ij} \rangle = 0$. The corresponding interaction energy is shown in Fig. 2b for $\nu = 1/4$. In this case, the equilibrium microstructure is trivial and consists of a single variant, as in this case the elastic energy is zero for the periodic system. Therefore, the situation differs from the previous shear transformation, where also lamellar arrangements with both variants lead to stress free situations. The reason is that any interface between two variants leads to a mismatch between adjacent variants for the tetragonal transformation, and therefore such a situation is energetically unfavorable here. A change of boundary conditions to vanishing average strain, $\langle \varepsilon_{ij} \rangle = 0$, alters the situation, since then arrangements with equal amounts of both variants are preferred, as this lowers the volumic part of the elastic energy. In this case, we find regular inclined stripes as equilibrium pattern, as shown in Fig. 3a.

Again, the solution is not unique; in particular, due to translation invariance, the annealer returns also configurations where the stripes are shifted. Also, a switch of the sign of the inclination angle ϕ (see definition in the figure) leads to energetically equivalent solutions. However, we do not find ground state configurations which lead to different (absolute) inclination angles or strip widths or even irregular variations of the latter, contrary to the shear transformation case before.

The reason for the observed ground state morphologies is a combination of continuum elasticity effects, the granular structure of the material and constraints induced by periodic boundary conditions. Figure 3b shows the computed elastic energy for different numbers of regular arrangements of stripes in the periodic system as function of the inclination angle ϕ. Here we see a pronounced influence of the grain size, as the elastic energy of configurations with regular stripe pairs with a discretization by 50×50 grains (squares in the figure) is higher than for corresponding cases with very fine grains, where discretization effects do not play a role anymore (smooth curves). The oscillating nature is due to the periodic boundary conditions, as improper choices of the inclination angle lead to discontinuities of the stripe patterns at the boundaries, which is energetically unfavorable.

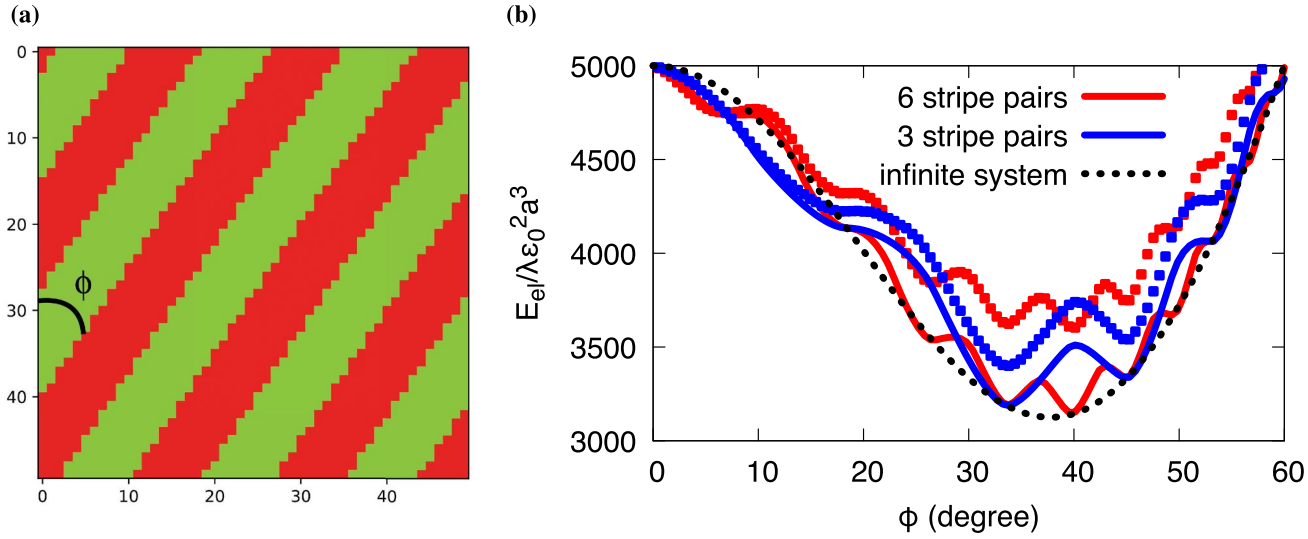

Figure 3. Resulting stripe patterns for tetragonal eigenstrain. (**a**) Equilibrium structure with three stripe pairs (counted along the horizontal axis) in a system consisting of 50×50 cuboidal grains. A vanishing mean strain, $\langle \varepsilon_{ij} \rangle = 0$, is imposed. The width of the stripes is uniform, consisting of grains with configuration $s_i = +1$ (red) and $s_i = -1$ (green). (**b**) Elastic energy of stripe patterns with different inclination angles ϕ. The solid curves correspond to smooth stripes (the grain size $a/L_x, a/L_y \ll 1$ is negligible) and show a pronounced stationary point for inclinations for which the pattern repeats periodically without kinks at the boundaries. The squares correspond to situations with the same number of stripes, where the system is discretized by 50×50 quadratic grains, leading to pronounced aliasing effects, and the resulting elastic energy is higher than for the smooth stripes. This shifts the energetic minimum for 6 stripe pairs at $\phi \approx 40°$ to a lower angle $\phi \approx 33°$ with 3 stripe pairs. The infinite system size limit for smooth stripes is depicted as black dotted curve.

Therefore, continuous patterns correspond to the stationary points of the curves. For specific angles, the curves for three and six stripe pairs meet at local minima, which is a consequence of the scale invariance of linear elasticity. From the smooth, continuum limit curves one would conclude that an angle of about $\phi \approx 40°$ should lead to the energetically lowest configuration (absolute minimum of the smooth red curve). Moreover, in the limit of infinite systems, where periodic boundary conditions do not play a role anymore, an analytical treatment is possible, leading to the energy expression $E_{\mathrm{el}}^{\infty} = VB(n)/2$ for equal volume fraction of the two variants with

$$B(n) = \frac{4\mu}{\lambda + 2\mu}\varepsilon_0^2 \left[(3\lambda + 2\mu) - 2(3\lambda + 2\mu)n^2 + 4(\lambda + \mu)n^4\right]$$

with $n = \cos\phi$. Energy minimization gives the optimal angle $\phi = \cos^{-1}\sqrt{5/8} \approx 37.8°$, see Fig. 3b (minimum of the black dotted curve).

However, these predictions disagree with the finding from the quantum annealer, which favors a configuration with three stripe pairs at a lower angle of $\phi \approx 33°$. This observation can be understood by consideration of the granular structure of the patterns investigated here, as the microstructure in the annealer simulations consists of 50×50 square grains. First, the explicit appearance of the length scale a breaks the scale invariance of the periodic pattern, and therefore the minima of the energy curves belonging to the discrete microstructures (squares in Fig. 3b) do not coincide anymore at the local minima. Additionally, with increasing inclination antialiasing effects of the patterns become more relevant, and therefore the energy curves show an increasing disagreement with the continuum limit curves. As a result, the energetic minimum in the discrete microstructure indeed shifts toward a configuration with three stripe pairs at $\phi \approx 33°$ (absolute minimum of the blue squares in Fig. 3b), which is in agreement with the prediction of the quantum annealer. Consequently, details of the granular structure can change the energetics compared to a full continuum approximation, especially since many local minima of the elastic energy are located close to each other.

Variant selection in realistic microstructures. The approach presented above is not limited to mutually interacting cuboidal grains, but can also be applied to realistic microstructures. To illustrate the procedures, we have generated a microstructure consisting of $N = 400$ grains using a Voronoi tesselation[41]. Each grain is allowed to take one out of two martensite variants with the tetragonal eigenstrain tensor, and we pre-compute all mutual elastic interactions between them. We note that contrary to the case with the cuboidal grains in a periodic array here we cannot exploit translational invarince due to the different shapes of the grains, and hence these elastic interaction energy calculations scale here as $\mathcal{O}(N^2)$ instead of $\mathcal{O}(N)$ before, although we still use periodic boundary conditions. Additionally, we consider now arbitrary given external strains $\langle\varepsilon_{ij}\rangle$, which leads to the appearance of a "magnetic" term like in the one dimensional description. With that, we can predict the equilibrium variant distribution within the microstructure using the hybrid quantum annealer, and this step is typically executed within a few seconds of runtime.

Examples for the equilibrium microstructures are shown in Fig. 4 as function of the externally applied strain $\langle\varepsilon_{xx}\rangle$, whereas the other average strain components vanish.

The observed microstructures are indeed similar to what we have found before using the square discretization, although here the band widths and orientation deviate from the previous case due to microstructural details and the smaller number of grains, and these effects can be explained using an analysis similar to the one done for Fig. 3b. We note that in these microstructures all grains have the same orientation, and therefore the application of a tensile strain strongly favors the selection of the grain variant $s_i = +1$ (for a compressive situation we observe the opposite behavior), and we find a full alignment of all variants in the last snapshot.

Additionally, we have performed the same analysis for grains with uniformly distributed random orientation, which implies a rotation of the local transformation strain tensor, see Fig. 5 for the grain orientations and for the variant selection.

Here, also the equilibrated spatial distribution of the variants appears to be irregular. Application of a tensile strain again favors the "alignment" of the variant, but this time even for high strains not all grains select the same variant, which is due to the local rotation. In fact, a grain, which is rotated by 90° with respect to the straining direction has a preference to be in variant state $s_i = -1$, as then the direction of expansion is aligned with the external tensile strain. This can be clearly seen e.g. in Fig. 5(c) for the highest tensile strain in x direction, where the remaining patches with "spin" $s_i = -1$ correspond to the grains with orientation close to $\pi/2$ (or $3\pi/2$). We emphasize that for a given microstructure (shapes of all grains) the mutual elastic grain-grain interactions have to be computed only once. As mentioned before, this step has to be done with high precision, and consequently this is the step which demands the highest amount of computing time. After that, all changes of the external boundary conditions affect only the $k = 0$ mode contributing to the interactions J_{ij} and h_i, and these terms can be calculated analytically (see methods section). As each hybrid quantum annealing calculation typically requires only a few seconds, the entire microstructural change during mechanical loading can be calculated extremely fast.

Discussion

The central result of the present paper is the shown optimization of microstructures via quantum annealing, exhibiting a clear performance advantage of the novel approach compared to conventional energy minimization strategies. The brute force approach is not recommended, whereas optimized simulated annealing algorithms produce good results. However, quantum annealing represents the by far fastest method for optimization problems, particularly for systems with high numbers of grains (spins) and non-vanishing coupling constants and biases, and allows the determination of ground state configurations for system sizes, which are not accessible for the classical algorithms on reasonable computing timescales.

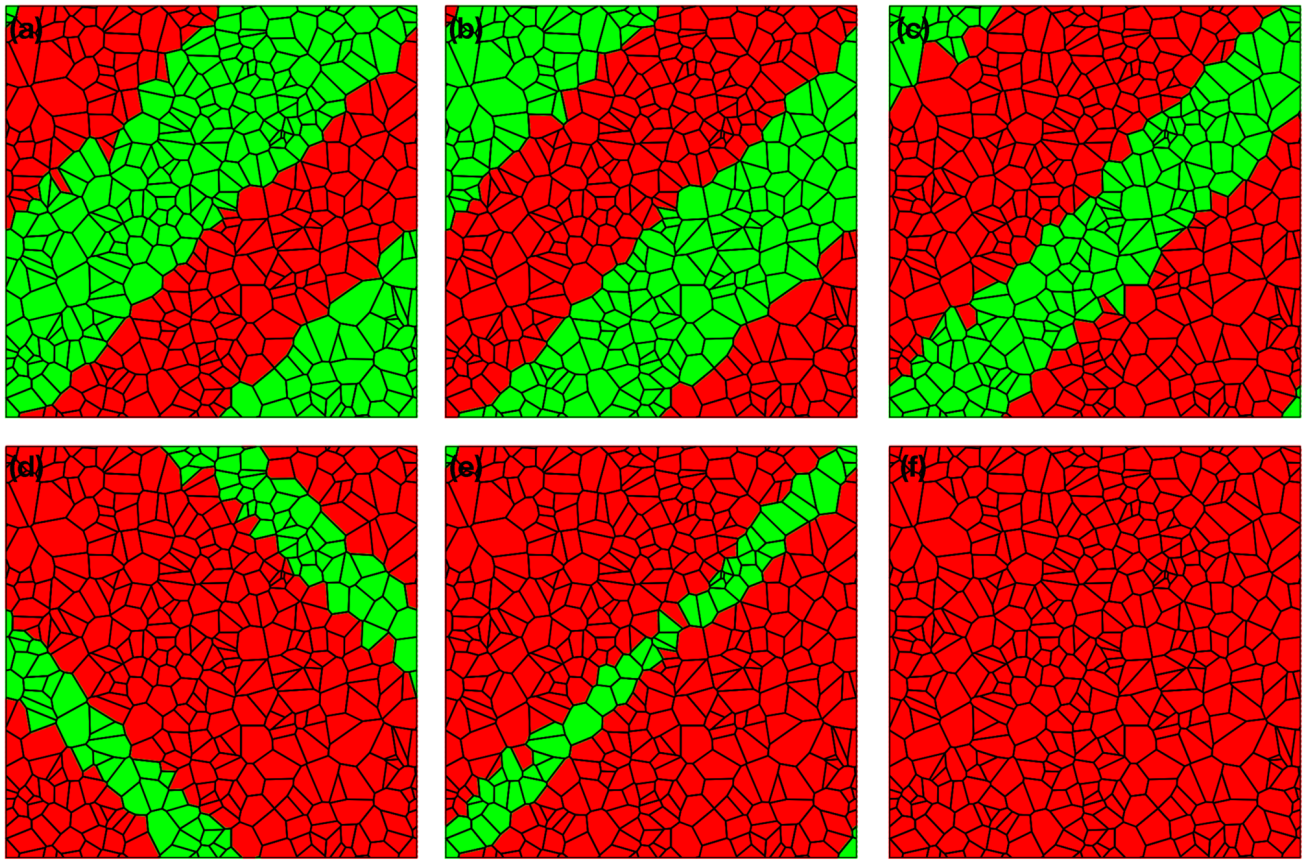

Figure 4. Resulting equilibrium variant distribution with uniform grain orientation. The microstructures consist of 400 grains and tensile strain is applied in horizontal (x) direction. Red (green) grains correspond to variant $s_i = +1$ ($s_i = -1$). The tensile strain is (**a**) $\langle \varepsilon_{xx} \rangle / \varepsilon_0 = 0$, (**b**) $\langle \varepsilon_{xx} \rangle / \varepsilon_0 = 0.1$, (**c**) $\langle \varepsilon_{xx} \rangle / \varepsilon_0 = 0.5$, (**d**) $\langle \varepsilon_{xx} \rangle / \varepsilon_0 = 0.9$, (**e**) $\langle \varepsilon_{xx} \rangle / \varepsilon_0 = 1.1$ and (**f**) $\langle \varepsilon_{xx} \rangle / \varepsilon_0 = 1.3$.

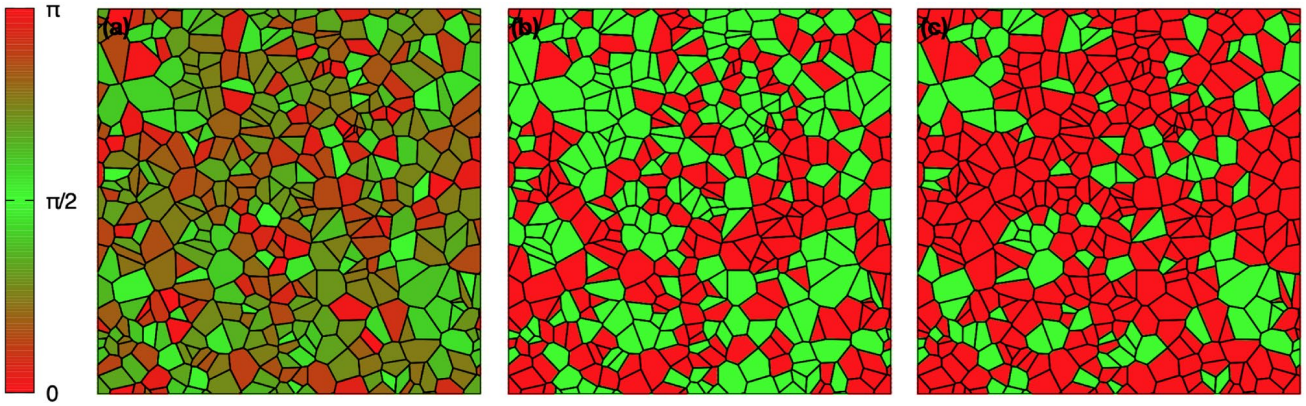

Figure 5. Resulting equilibrium variant distribution with random grain orientation. (**a**) Grain orientation map corresponding to the microstructures. In the color bar the grain rotation angle is given in radian (modulo π due to symmetry). The rotation axis is along the [001] direction. The microstructures consist of 400 grains and tensile strain is applied in horizontal (x) direction. The grains have a random orientation, which is the same for all cases, based on a uniform distribution. The tensile strain in horizontal direction is (**b**) $\langle \varepsilon_{xx} \rangle / \varepsilon_0 = 0$ and (**c**) $\langle \varepsilon_{xx} \rangle / \varepsilon_0 = 2.1$. Red (green) grains correspond to variant $s_i = +1$ ($s_i = -1$).

For a system consisting of N grains, we need to compute $\mathcal{O}(N^2)$ spin-spin interactions. These elastic energy calculations have to be done with high accuracy, and therefore they dominate the overall computing time. After that, $\mathcal{O}(2^N)$ spin configurations need to be compared to identify the equilibrium configuration. For the conventional algorithm, this combinatorial step dominates the total computational effort already for low values of N. In contrast, with the quantum annealer or its hybrid variant the computation time for the minimization of the Ising energy expression is completely negligible compared to the elastic interaction energy computations. Hence, we

have demonstrated that QA is able to drastically optimize the search for microstructural equilibrium states in solid phases with long-range elastic interactions. Already today, the usage of hybrid quantum annealing enables the computation of microstructures with several thousand grains which all interact with each other, which is essential for a realistic modeling of microstructures inside various materials.

For many application relevant investigations, it is critical to understand whether and how models can be formulated that they are suitable for quantum computing. We have demonstrated this here for the particular case of long-range elastic interactions. Extensions towards the consideration of interfacial energy, multiple martensite variants, anisotropic elasticity, orientation relationships between grains and phases, and different spatial dimensions are obvious, as they do not conceptually influence the presented strategy of formulating the problem in terms of an Ising model. Inhomogeneous elasticity and the proximity to free surfaces can effectively lead to many-body interactions, for which perturbative extensions or the introduction of product spin variables are promising directions[37,42]. Beyond the purely elastic effects, further potential applications comprise phase changes in multi-phase solid state batteries, phase transformations in high strength steels or other materials like ferroelectrics. Overall, the separation of continuous and discrete degrees of freedom and the quantum treatment of the latter may also be beneficial for hybrid phase field and quantum annealing descriptions which combine a variant selection with a grain morphology evolution in an efficient way to drastically reduce computing time demands of existing approaches for application relevant sample sizes.

Methods

Quantum annealing. Like general purpose quantum computers, a quantum annealer is built from qubits, which here store and process information using superconducting loops. A clockwise or anticlockwise circulating current in such a loop represents different spin states[12]. In each qubit superconducting loops interact with external flux biases, which allows to construct an energy landscape, where the fluxes influence barrier height and energy difference[12]. At the start of the computation, the system is initialized in the ground state of a known Hamiltonian $H_0 \sim -\sum_i \sigma_i^x$ with Pauli matrices σ_i, i.e. a strong transverse magnetic field[13,43]. During the annealing process, the Hamiltonian is turned into the desired one based on an Ising model[11] $H_p = \sum_i h_i s_i + \sum_{i<j} J_{ij} s_i s_j$ with spin states $s_i = \pm 1$, bias h_i and coupling strength J_{ij} between qubits i and j, for which an energetic minimum is sought, $\min_{\{s_i=\pm 1\}} H_p$. Both Hamiltonians do not commute[11], and the time of the initial Hamiltonian to adopt the low energy state is sufficiently large to ensure the validity of the adiabatic theorem of quantum mechanics[44], which states that a system remains in its eigenstate, if changes occur adiabatically. Notice that the quantum annealing employs tunneling to leave metastable regions, contrary to the simulated annealing[6]. Another important quantum mechanical principle in quantum annealing is the entanglement and the usage of entangled states inside quantum annealing processors (QPU)[45].

As in practise this approach does not always deliver the lowest energy state, especially if energetically close low energy states exist, a suitable number of repetitions is made and the configuration with the lowest detected energy is taken. If the Ising problems do not match the architecture of the QPU, a subgraph of coupled qubits, know as chains, cover one variable of the problem in the so called minor embedding[36,46]. Additionally, for huge systems hybrid quantum annealing exploits classical algorithms and the interplay with quantum annealing in areas of high computational demands using a QPU coprocessor working with generic parameters for up to 11616 spin variables on the D-Wave Advantage system[36,47]. In practise, the D-Wave framework Leap[48] allows a direct formulation in terms of a problem Ising Hamiltonian.

Brute force minimization. For N spins we compute the energy of all 2^N possible configurations to determine the minimum. This deterministic approach delivers the true ground state energy but has a high computational effort.

Simulated annealing. For this probabilistic approach[49] a random initial configuration is chosen. A new candidate configuration, which we generate here by a single spin flip, is accepted if its energy is lower than the previous value. If the energy is higher by an amount ΔE, the configuration is accepted with a probability given by the Boltzmann factor $\exp(-\Delta E/T)$, in order not to get stuck in local energy minima. During the simulation, the temperature T is reduced according to a specific cooling strategy, in order to converge towards an energetic minimum at the end of the simulation. As our main goal is not to maximize the performance of the (classical) algorithms but rather to demonstrate the general scaling behavior, we refrain from a detailed discussion of the parameter optimization of the probabilistic simulated annealing approach. This includes in particular the use of suitable stopping criteria when no further reduction of the energy occur, as well as the use of problem adapted cooling strategies. For the simulated annealing approach we use single spin flips trials in each iteration, and the temperature T is decreased each time by $\Delta T/\mu_{\text{eff}}\varepsilon_0^2 d^2 = 10^{-6}$, which delivers a good performance for large system sizes. The simulations are stopped after a fixed number of 10^7 steps, which is optimized for the largest considered spin system with $N = 150$ in Fig. 1b, leading to a scaling of the computation time $\sim N^2$ due to the calculation of the interaction energy.

Elasticity. We solve the elastic problem of a multi-grain setup with homogeneous linear elasticity, i.e. all variants and phases are assumed to have the same elastic constants. Also, coherent interfaces are assumed, which means continuity of displacements at the interfaces. The martensite variants have different stress free strains (or eigenstrains) compared to the mother austenite phase, hence the stress-strain relation reads for general linear elasticity $\sigma_{ij} = \lambda_{ijkl}(\varepsilon_{kl} - \varepsilon_{kl}^{(0)})$, where $\varepsilon_{kl}^{(0)}(\mathbf{r})$ is the local stress free strain tensor and λ_{ijkl} the elastic tensor. We determine the elastic equilibrium configuration, which obeys the condition $\partial\sigma_{ij}/\partial x_j = 0$ in bulk domains and

the continuity of normal stresses at interfaces, using Fourier transformation approaches[32]. From that, the elastic energy can be computed in reciprocal space as[32]

$$E_{\mathrm{el}} = \frac{V}{2} \sum_{\mathbf{k} \neq 0} B(\mathbf{n}) |\hat{\theta}(\mathbf{k})|^2 \tag{3}$$

for a periodic system with vanishing average stress as boundary condition, where $\hat{\theta}(\mathbf{k})$ is the Fourier transform of the indicator field $\theta(\mathbf{r})$ and $B(\mathbf{n})$ with $\mathbf{n} = \mathbf{k}/k$ equals $B(\mathbf{n}) = \sigma^0_{ij}\varepsilon^0_{ij} - n_i\sigma^0_{ij}\Omega_{jk}\sigma^0_{kl}n_l$ with $\sigma^0_{ij} = \lambda_{ijkl}\varepsilon^0_{kl}$. Here, $\Omega_{ij}(\mathbf{n})$ is the normalized Green tensor for displacements, which is defined through its inverse as $\Omega^{-1}_{ik} = \lambda_{ijkl}n_j n_l$. The summation in Eq. (3) is over discrete vectors due to the periodic boundary conditions in real space. The summation is in principle infinite, and can be efficiently computed using the decoration technique[50]. For average strain boundary conditions, i.e. a prescribed value of $\langle\varepsilon_{ij}\rangle$, an additional homogeneous ($\mathbf{k} = 0$) contribution appears in Eq. (3), which reads $E_{\mathrm{hom}} = V\lambda_{ijkl}(\langle\varepsilon_{ij}\rangle - \langle\varepsilon^{(0)}_{ij}\rangle)(\langle\varepsilon_{kl}\rangle - \langle\varepsilon^{(0)}_{kl}\rangle)/2$, which can be calculated analytically.

Data availability

Data that was obtained during this project will be made available by the corresponding author upon request.

Received: 24 January 2023; Accepted: 10 April 2023
Published online: 13 April 2023

References

1. Karma, A. & Rappel, W. J. Phase-field method for computationally efficient modeling of solidification with arbitrary interface kinetics. *Phys. Rev. E* **53**, R3017(R) (1996).
2. Karma, A. & Rappel, W. J. Quantitative phase-field modeling of dendritic growth in two and three dimension. *Phys. Rev. E* **57**, 4323 (1998).
3. Boussinot, G. & Brener, E. A. Achieving realistic interface kinetics in phase-field models with a diffusional contrast. *Phys. Rev. E* **89**, 060402(R) (2014).
4. Wang, K., Boussinot, G., Hüter, C., Brener, E. A. & Spatschek, R. Modeling of dendritic growth using a quantitative nondiagonal phase field model. *Phys. Rev. Mater.* **4**, 033802 (2020).
5. Finel, A. *et al.* Sharp phase field method. *Phys. Rev. Lett.* **121**, 025501 (2018).
6. Finnila, A., Gomez, M., Sebenik, C., Stenson, C. & Doll, J. Quantum annealing: A new method for minimizing multidimensional functions. *Chem. Phys. Lett.* **219**, 343–348 (1994).
7. Brooke, J., Bitko, D., Rosenbaum, T. & Aeppli, G. Quantum annealing of a disordered magnet. *Science* **284**, 779–781 (1999).
8. Kadowaki, T. & Nishimori, H. Quantum annealing in the transverse Ising model. *Phys. Rev. E* **58**, 5355–5363 (1998).
9. Morita, S. & Nishimori, H. Mathematical foundation of quantum annealing. *J. Math. Phys.* **49**, 125210. https://doi.org/10.1063/1.2995837 (2008).
10. Rajak, A., Suzuki, S., Dutta, A. & Chakrabarti, B. Quantum annealing: An overview. *Phil. Trans. R. Soc. A* **381**, 20210417. https://doi.org/10.1098/rsta.2021.0417 (2023).
11. Warren, R. Mathematical methods for a quantum annealing computer. *J. Adv. Appl. Math.* **3**, 82–90 (2018).
12. Johnson, M. *et al.* Quantum annealing with manufactured spins. *Nature* **473**, 194–198 (2011).
13. Boixo, S. *et al.* Evidence for quantum annealing with more than one hundred qubits. *Nat. Phys.* **10**, 218–224 (2014).
14. Jünger, M. *et al.* Quantum annealing versus digital computing: An experimental comparison. *ACM J. Exp. Algorithms* **26**, 1.9 (2021).
15. Parekh, O. *et al.* Benchmarking adiabatic quantum optimization for complex network analysis. https://arxiv.org/abs/1604.00319 (2016).
16. Yan, B. & Sinitsyn, N. Analytical solution for nonadiabatic quantum annealing to arbitrary Ising spin Hamiltonian. *Nat. Commun.* **13**, 2212 (2022).
17. Li, R., Di Felice, R., Rohs, R. & Lidar, D. Quantum annealing versus classical machine learning applied to a simplified computational biology problem. *npj Quantum Inf.* **4**, 14 (2018).
18. Perdomo-Ortiz, A., Dickson, N., Drew-Brook, M., Rose, G. & Aspuru-Guzik, A. Finding low-energy conformations of lattice protein models by quantum annealing. *Sci. Rep.* **2**, 1–7 (2012).
19. Irbäck, A., Knuthson, L., Mohanty, S. & Peterson, C. Folding lattice proteins with quantum annealing. *Phys. Rev. Res.* **4**, 043013 (2022).
20. Boyda, E. *et al.* Deploying a quantum annealing processor to detect tree cover in aerial imagery of California. *PLOS ONE* **12**, e0172505 (2017).
21. Neukart, F. *et al.* Traffic flow optimization using a quantum annealer. *Front. ICT* **4**, 29 (2017).
22. Ohzeki, M., Miki, A., Miyama, M. & Terabe, M. Control of automated guided vehicles without collision by qantum annealer and digital devices. *Front. Comput. Sci.* **1**, 9 (2019).
23. Harris, R. *et al.* Phase transitions in a programmable quantum spin glass simulator. *Science* **361**, 162–165 (2018).
24. Kairys, P. *et al.* Simulating the Shastry–Sutherland ising model using quantum annealing. *PRX Quantum* **1**, 020320 (2020).
25. Sandt, R. & Spatschek, R. Efficient low temperature Monte Carlo sampling using quantum annealing. *Preprint* https://doi.org/10.21203/rs.3.rs-2624280/v1 (2023).
26. Kitai, K. *et al.* Designing metamaterials with quantum annealing and factorization machines. *Phys. Rev. Res.* **2**, 013319 (2020).
27. Otsuka, K. & Ren, X. Physical metallurgy of Ti-Ni-based shape memory alloys. *Progress Mater. Sci.* **50**, 511 (2005).
28. Sherrington, D. A simple spin glass perspective on martensitic shape-memory alloys. *J. Phys.: Condens. Matter* **20**, 304213. https://doi.org/10.1088/0953-8984/20/30/304213 (2008).
29. Kartha, S., Castán, T., Krumhansl, J. & Sethna, J. Spin-glass nature of tweed precursors in martensitic transformations. *Phys. Rev. Lett.* **67**, 3630. https://doi.org/10.1103/PhysRevLett.67.3630 (1991).
30. Sethna, J., Kartha, S., Castán, T. & Krumhansl, J. Tweed in martensites: A potential new spin glass. *Phys. Scripta* **214–219**, 1992. https://doi.org/10.1088/0031-8949/1992/T42/034 (1992).
31. Vasseur, R. & Lookman, T. Spin models for ferroelastics: Towards a spin glass description of strain glass. *Solid State Phenom.* **172–174**, 1078–1083. https://doi.org/10.4028/www.scientific.net/SSP.172-174.1078 (2011).
32. Khachaturyan, A. *Theory of Structural Transformations in Solids* (Dover Publications Inc, Mineola, New York, 2008).
33. Chen, L.-Q. Phase-field models for microstructure evolution. *Annu. Rev. Mater. Res.* **32**, 113–140 (2002).
34. Boothby, K., Bunyk, P., Raymond, J. & Roy, A. Next-generation topology of D-wave quantum processors. https://arxiv.org/abs/2003.00133 (2020).

35. Grant, E. & Humble, T. Benchmarking embedded chain breaking in quantum annealing. *Quantum Sci. Technol.* **7**, 025029 (2022).
36. Raymond, J. *et al.* Hybrid quantum annealing for larger-than-QPU lattice-structured problems. *ACM Trans. Quantum Comput.*https://doi.org/10.1145/3579368 *(2023).*
37. Johnson, W. & Voorhees, P. Elastic interactions and stability of misfitting cuboidal inhomogeneities. *J. Appl. Phys.* **61**, 1610 (1987).
38. Ray, P., Chakrabarti, B. & Chakrabarti, A. Sherrington–Kirkpatrick model in a transverse field: Absence of replica symmetry breaking due to quantum fluctuations. *Phys. Rev. B* **39**, 11828. https://doi.org/10.1103/PhysRevB.39.11828 (1989).
39. Fratzl, P., Penrose, O. & Lebowitz, J. Modeling of phase separation in alloys with coherent elastic misfit. *J. Stat. Phys.* **95**, 1429–1503 (1999).
40. Landau, L. & Lifshitz, E. *Theory of Elasticity* Vol. 7 (Pergamon Press, Oxford, 1970).
41. Rycroft, C. Voro++: A three-dimensional voronoi cell library in c++. *Chaos* **19**, 041111 (2009).
42. Spatschek, R. *et al.* Scale bridging description of coherent phase equilibria in the presence of surfaces and interfaces. *Phys. Rev. B* **94**, 134106 (2016).
43. Rønnow, T. *et al.* Defining and detecting quantum speedup. *Science* **345**, 420–423 (2014).
44. Lucas, A. Ising formulations of many NP problems. *Front. Phys.* **2**, 5 (2014).
45. Lanting, T. *et al.* Entanglement in a quantum annealing processor. *Phys. Rev. X* **4**, 021041 (2014).
46. Choi, V. Minor-embedding in adiabatic quantum computation: II. Minor-universal graph design. *Quant. Inf. Process.* **10**, 343–353 (2011).
47. Berwald, J. The mathematics of quantum-enabled applications on the D-wave quantum computer. *Notices Am. Math. Soc.* **66**, 832–841 (2019).
48. D-Wave Leap quantum cloud service. https://cloud.dwavesys.com. [Online; accessed 23-December-2022].
49. Kirkpatrick, S., Gelatt, C. & Vecchi, M. Optimization by simulated annealing. *Science* **220**, 671–680 (1983).
50. Rodney, D., Le Bouar, Y. & Finel, A. Phase field methods and dislocations. *Acta Mat.* **51**, 17–30 (2003).

Acknowledgements

This research was funded by the German Federal Ministry of Education and Research (BMBF) via the project Meet HiEnD 3 and the Helmholtz project ZeDaBase. Open access was funded by the Deutsche Forschungsgemeinschaft (DFG, German Research Foundation) - 491111487. The authors gratefully acknowledge the Jülich Supercomputing Centre (https://www.fz-juelich.de/ias/jsc) for funding this project by providing computing time on the D-Wave Advantage™ System JUPSI through the Jülich UNified Infrastructure for Quantum computing (JUNIQ).

Author contributions

R.Sa., Y.L.B. and R.Sp. contributed to analytical and numerical calculations, methodology, visualization and analysis. All authors contributed to the writing of the manuscript.

Funding

Open Access funding enabled and organized by Projekt DEAL.

Competing Interests

The authors declare no competing interests.

Additional information

Correspondence and requests for materials should be addressed to R.S.

Reprints and permissions information is available at www.nature.com/reprints.

Publisher's note Springer Nature remains neutral with regard to jurisdictional claims in published maps and institutional affiliations.

Microstructure equilibration with consideration of elastic and interfacial interactions via quantum annealing with application to the solid electrolyte LLZO

Roland Sandt,[1] Yann Le Bouar,[2] and Robert Spatschek[1,3]
[1]*Structure and Function of Materials, Institute of Energy and Climate Research IEK-2, Forschungszentrum Jülich GmbH, 52425 Jülich, Germany*
[2]*Université Paris-Saclay, ONERA, CNRS, Laboratoire d'Etude des Microstructures, 92320 Châtillon, France*
[3]*JARA-ENERGY, 52425 Jülich, Germany*

(Received 3 May 2024; accepted 5 June 2024; published 10 July 2024)

We present a detailed derivation of the elastic energy of a homogeneous, isotropic linear elastic medium consisting of different coherent martensite variants or phases and its mapping to an Ising model, as required for an efficient quantum annealing determination of the equilibrium microstructure. The approach is demonstrated for a sample with a large number of grains with a tetragonal eigenstrain. Furthermore, we illustrate how the elastic effects may lead to the formation of ion conducting channels in the doped solid electrolyte $Li_7La_3Zr_2O_{12}$ (LLZO). Apart from bulk elastic and chemical effect we demonstrate how to include interfacial effects into the quantum annealing approach and emphasize the importance of high precision elastic calculations.

DOI: 10.1103/PhysRevResearch.6.033047

I. INTRODUCTION

The properties of many materials are strongly influenced by the microstructure, which can ideally be tailored to lead to the desired behavior as needed for the intended application. Here, mechanical effects can trigger solid state transformations, which could be used to create the desired microstructure. Such a processing technology needs to come along with powerful simulation techniques, which are able to quantitatively predict equilibrated microstructures in large and application relevant systems, to ensure a long term stability of the adjusted phase arrangement. Whereas phase-field approaches [1–4] are strong and established approaches to simulate the kinetics of microstructure evolution, the long-term behavior involving thermochemical, interfacial but also mechanical effects is hard to address due to large simulation times.

Recently, we established a new simulation technique which is based on quantum annealing (QA), and which allows to directly determine the thermodynamic ground state for a martensitic microstructure with elastic interactions in a very efficient way [5,6]. QA itself is a specific case of adiabatic quantum computing, which has become very powerful during recent years [7–11]. Nowadays such machines with several thousand qubits and couplers are available on the market. To use this technique, it is necessary to express the problem of interest as a discrete optimization problem, as described through an Ising model or equivalently through a quadratic unconstrained binary optimization problem [12–14]. Despite the fact that quantum annealers allow highly efficient global energy minimizations, applications of this technology in the field of materials science and related disciplines [5,15–25] are still rare due to this specific problem structure. The main part of actual research concentrates on performance test and benchmarking of quantum annealing versus classical algorithms [26–29]. Indeed, the solution of optimization problems via quantum annealing plays recently a role in other research fields [30–35].

The problem and solution approach proposed in Refs. [5,6] is based on the concept that a grain structure of the material of interest is known, and that for each grain by the selection of a martensite variant (or more generally a phase) is driven by the minimization of energy. Such transformations are important for example for shape memory alloys, which undergo reversible, structural phase transitions between martensitic and austenitic phases, depending on temperature and the trained, previous shape [36,37]. If the grains are coherently connected, then interfaces between different phases lead to internal stresses and therefore raise the elastic energy. The approach expresses the energy minimization as a discrete optimization process by mapping it to a spin glass problem [38–41]. Although this is a significant simplification of the entire microstructure optimization process, the problem size grows exponentially with the number of grains and is therefore hard to solve with conventional computing methods. We have demonstrated in Ref. [5] that QA leads to a remarkable acceleration of the computations, therefore allowing for large scale simulations.

The purpose of the the present paper is fourfold:

First, it describes the entire methodology in more detail than in Ref. [5]. This includes in particular the derivation of the coefficients of the underlying spin glass model through a Fourier space representation of the elastic energy stored in the microstructure (Sec. II). In this way, one obtains explicit

expressions for the coefficients of the Ising model, as used by the quantum annealer. This approach has the advantage of delivering accurate expressions for the elastic interactions between the grains. As we demonstrate explicitly in this paper, this is a necessary condition for obtaining the correct equilibrium microstructures using QA (Sec. III D).

Second, we demonstrate the application to large systems with up to several thousand grains, which is important for generating representative volume elements of the entire microstructure and their response to external mechanical loads (Sec. III A).

Third, we apply the general approach to the ceramic solid electrolyte $Li_7La_3Zr_2O_{12}$ (LLZO), therefore going beyond the aforementioned shape memory alloys. LLZO has a thermodynamically stable tetragonal phase with poor Li-ion conductivity [42,43]. However, for battery applications the highly conductive and at ambient temperatures unstable cubic phases [42,44] is desired. The cubic phase can be stabilized via substitutions of different aliovalent elements like Al^{3+}, Ta^{5+}, and Ga^{3+} [43–45]. Several studies investigated the resulting mechanical and structural properties of pure and substituted tetragonal and cubic phases [46–48]. Here we investigate to which extent percolating, highly conducting ion channels may form as a result from a self-organization process driven by elastic coherency stresses (Sec. III B).

Finally, we demonstrate how the approach can be extended to incorporate also interfacial effects and discuss their influence on the microstructure selection (Sec. III C).

II. METHODS

A. Elastic energy in reciprocal space

In this section an expression for the elastic energy of the system, based on the solution of the underlying elastic problem in reciprocal space, is presented. Although the use of Fourier methods is beneficial and allows to obtain the quantum annealer coefficients with sufficient accuracy, in principle any other elastic solver can be used as well, as discussed in Ref. [6]. For our specific application, we assume that the eigenstrain is constant within each grain (and related to the martensite variant), and that the grains are coherently connected. This means on the level of continuum elasticity that at the interfaces between adjacent grains not only the normal and shear stresses are continuous (by force balance) but also the displacements. For simplicity, we assume isotropic elasticity. As external boundary cases we consider the two important cases of either a vanishing mean stress in a periodic system or a given mean strain $\langle\epsilon_{\alpha\beta}\rangle$. Whereas the formalism works both in two and three dimensions, we use for the applications below specifically a two dimensional plane strain setup, i.e., the displacement component vanishes, $u_z \equiv 0$, and u_x, u_y depend only on x and y. From the obtained expression of the elastic energy we generate a formulation as Ising model, which can then be implemented on the quantum annealer. As we assume the elastic constants to be the same everywhere (homogeneous elasticity), the interactions between grains decompose into pairwise terms [49], which is necessary for the annealer formulation.

The starting point is the elastic energy for isotropic materials

$$E_{\mathrm{el}} = \int_V \left(\frac{\lambda}{2}\left(\epsilon_{\alpha\alpha}(\mathbf{r}) - \epsilon^{(0)}_{\alpha\alpha}(\mathbf{r})\right)^2 + \mu\left(\epsilon_{\alpha\beta}(\mathbf{r}) - \epsilon^{(0)}_{\alpha\beta}(\mathbf{r})\right)^2\right) d\mathbf{r}, \tag{1}$$

with Lamé coefficient λ and shear modulus μ (we employ Einstein's sum convention). $\epsilon^{(0)}_{\alpha\beta}(\mathbf{r})$ is the position-dependent eigenstrain, which is known for a given microstructure. After solution of the elastic problem, the elastic energy of the system reads in reciprocal space

$$\begin{aligned} E_{\mathrm{el}} = {} & \frac{V}{2}\sum_{\mathbf{k}\neq 0}\left[\hat{\sigma}^{(0)*}_{\alpha\beta}(\mathbf{k})\hat{\epsilon}^{(0)}_{\alpha\beta}(\mathbf{k}) - \hat{\sigma}^{(0)}_{\alpha\delta}(\mathbf{k})k_\alpha G_{\delta\beta}k_\gamma\hat{\sigma}^{(0)*}_{\beta\gamma}(\mathbf{k})\right] \\ & + \frac{\lambda V}{2}\left(\langle\epsilon_{\alpha\alpha}\rangle - \hat{\epsilon}^{(0)}_{\alpha\alpha}(\mathbf{k}=0)\right)^2 \\ & + \mu V\left(\langle\epsilon_{\alpha\beta}\rangle - \hat{\epsilon}^{(0)}_{\alpha\beta}(\mathbf{k}=0)\right)^2. \end{aligned} \tag{2}$$

For a derivation of this energy expression and explanation of the involved terms we refer to the Appendix. In particular, the hat symbol ($\hat{}$) denotes Fourier transformation with reciprocal lattice vector $\mathbf{k}$, and $\sigma^{(0)}_{\alpha\beta} = \lambda\delta_{\alpha\beta}\epsilon^{(0)}_{\gamma\gamma} + 2\mu\epsilon^{(0)}_{\alpha\beta}$ is the eigenstress. The isotropic elastic Green tensor is defined through its inverse, $G^{-1}_{\beta\delta} = \lambda k_\beta k_\delta + \mu k_\alpha k_\alpha \delta_{\beta\delta} + \mu k_\beta k_\delta$. The expression (2) holds for given average strain boundary conditions [case (ii)]. For a stress free system [case (i)], where the average stress vanishes, the last two terms vanish, as by mechanical equilibrium conditions one obtains in particular for the homogeneous strain $\langle\epsilon_{\alpha\beta}\rangle = \hat{\epsilon}^{(0)}_{\alpha\beta}(\mathbf{k}=0)$.

B. Ising formulation

We assume the entire system to be decomposed into N grains. At this point, we do not make assumptions about the grain structure, so they can be, e.g., regular cuboids or random structures, e.g., taken from electron backscatter diffraction (EBSD) images or a Voronoi tesselation. In agreement with the preceding analysis, the grains are assumed to be coherent from the point of view of elasticity. The grains are enumerated by n and characterized by an indicator function

$$\theta_n(\mathbf{r}) = \begin{cases} 1 & \text{inside grain } n, \\ 0 & \text{otherwise}, \end{cases} \tag{3}$$

which satisfies the condition $\sum_i \theta_i(\mathbf{r}) = 1$. The eigenstrain therefore reads

$$\begin{aligned} \epsilon^{(0)}_{\alpha\beta}(\mathbf{r}) &= \sum_{n=1}^{N}\theta_n(\mathbf{r})\sum_{k=1}^{K}\left(s_{n,k}\epsilon^{(0,n,k)}_{\alpha\beta} + \epsilon^{(0,n,0)}_{\alpha\beta}\right) \\ &= \sum_{n,k} s_{n,k}\epsilon^{(0,n,k)}_{\alpha\beta}(\mathbf{r}) + \sum_n \epsilon^{(0,n,0)}_{\alpha\beta}(\mathbf{r}), \end{aligned} \tag{4}$$

where $s_{n,k} = \pm 1$ are the spin values to distinguish the different variants. We consider here a generalized case to describe more than two variants, therefore extending the previous simplification in Ref. [5] with only two variants with opposite

eigenstrain. Therefore, an additional summation over K spins per grain is needed, to encode up to 2^K different variants, see also [6]. (We note that running roman indices like k enumerate spins and variants, which have to be distinguished from reciprocal lattice vectors $\mathbf{k}$, which are displayed in bold, with components k_α. Greek letters are used for spatial components.) In many situations it is beneficial to consider also an offset $\epsilon^{(0,n,0)}_{\alpha\beta}$, as will be illustrated below in Sec. III B. We note that the eigenstrain contributions can differ from grain to grain, to capture different phases or grain orientations. From the spatially constant eigenstrain contributions within each grain in the first line of Eq. (4), in the second line a shorter notation is defined using position dependent eigenstrain contributions, which have a nonvanishing value only inside one grain.

Similarly, we write for the Fourier transformation of $\epsilon^{(0)}_{\alpha\beta}(\mathbf{r})$

$$\hat{\epsilon}^{(0)}_{\alpha\beta}(\mathbf{k}) = \sum_{n,k} s_{n,k}\hat{\epsilon}^{(0,n,k)}_{\alpha\beta}(\mathbf{k}) + \sum_{n}\hat{\epsilon}^{(0,n,0)}_{\alpha\beta}(\mathbf{k}). \tag{5}$$

Consequently, the eigenstress field $\sigma^{(0)}_{\alpha\beta}(\mathbf{r})$ [see Eq. (A15)] has in reciprocal space the form

$$\begin{aligned}\hat{\sigma}^{(0)}_{\alpha\beta}(\mathbf{k}) &= \lambda\delta_{\alpha\beta}\hat{\epsilon}^{(0)}_{\gamma\gamma}(\mathbf{k}) + 2\mu\hat{\epsilon}^{(0)}_{\alpha\beta}(\mathbf{k}) \\ &= \sum_{n,k} s_{n,k}\hat{\sigma}^{(0,n,k)}_{\alpha\beta}(\mathbf{k}) + \sum_{n}\hat{\sigma}^{(0,n,0)}_{\alpha\beta}(\mathbf{k}).\end{aligned} \tag{6}$$

By insertion into the energy expression (2) we obtain the Ising formulation, which is necessary for the quantum annealer. We use here the fixed strain case (ii) with the knowledge that it differs from the free stress case (i) only by the $\mathbf{k} = 0$ terms. Therefore, we need to bring the energy to the form

$$E_{\mathrm{el}} = E_0 + \sum_{i<j} J_{ij}s_i s_j + \sum_i h_i s_i, \tag{7}$$

where i and j are a shorthand notation for the combined grain and variant index, e.g., $i = (n, k)$. With this we get the final elastic energy expression

$$\begin{aligned}E_{\mathrm{el}} = \frac{V}{2}\Bigg\{ &\sum_{\mathbf{k}\neq 0}\sum_{n,m}\left(\hat{\sigma}^{(0,n,0)*}_{\alpha\beta}(\mathbf{k})\hat{\epsilon}^{(0,m,0)}_{\alpha\beta}(\mathbf{k}) - k_\alpha G_{\gamma\beta}k_\delta\hat{\sigma}^{(0,n,0)}_{\alpha\gamma}(\mathbf{k})\hat{\sigma}^{(0,m,0)*}_{\beta\delta}(\mathbf{k})\right) + \lambda\left(\bar{\epsilon}_{\alpha\alpha} - \sum_n\hat{\epsilon}^{(0,n,0)}_{\alpha\alpha}(\mathbf{k}=0)\right)^2 \\ &+ 2\mu\left(\bar{\epsilon}_{\alpha\beta} - \sum_n\hat{\epsilon}^{(0,n,0)}_{\alpha\beta}(\mathbf{k}=0)\right)^2 + \sum_{\mathbf{k}\neq 0}\sum_{n,k}\sum_{m,v}\Big[\hat{\sigma}^{(0,n,k)*}_{\alpha\beta}(\mathbf{k})\hat{\epsilon}^{(0,m,v)}_{\alpha\beta}(\mathbf{k}) - k_\alpha G_{\gamma\beta}k_\delta\hat{\sigma}^{(0,n,k)}_{\alpha\gamma}(\mathbf{k})\hat{\sigma}^{(0,m,v)*}_{\beta\delta}(\mathbf{k}) \\ &+ \lambda\hat{\epsilon}^{(0,n,k)}_{\alpha\alpha}(\mathbf{k}=0)\hat{\epsilon}^{(0,m,v)}_{\alpha\alpha}(\mathbf{k}=0) + 2\mu\hat{\epsilon}^{(0,n,k)}_{\alpha\beta}(\mathbf{k}=0)\hat{\epsilon}^{(0,m,v)}_{\alpha\beta}(\mathbf{k}=0)\Big]s_{n,k}s_{m,v} \\ &+ \sum_{\mathbf{k}\neq 0}\sum_{n,k}\sum_{m}\Big[\hat{\sigma}^{(0,n,k)*}_{\alpha\beta}(\mathbf{k})\hat{\epsilon}^{(0,m,0)}_{\alpha\beta}(\mathbf{k}) + \hat{\sigma}^{(0,m,0)*}_{\alpha\beta}(\mathbf{k})\hat{\epsilon}^{(0,n,k)}_{\alpha\beta}(\mathbf{k}) - k_\alpha G_{\gamma\beta}k_\delta\left(\hat{\sigma}^{(0,n,k)}_{\alpha\gamma}(\mathbf{k})\hat{\sigma}^{(0,m,0)*}_{\beta\delta}(\mathbf{k}) + \hat{\sigma}^{(0,m,0)}_{\alpha\gamma}(\mathbf{k})\hat{\sigma}^{(0,n,k)*}_{\beta\delta}(\mathbf{k})\right) \\ &+ 2\lambda\left(\hat{\epsilon}^{(0,n,k)}_{\alpha\alpha}(\mathbf{k}=0)\hat{\epsilon}^{(0,m,0)}_{\beta\beta}(\mathbf{k}=0) - \bar{\epsilon}_{\alpha\alpha}\hat{\epsilon}^{(0,n,k)}_{\beta\beta}(\mathbf{k}=0)\right) + 4\mu\left(\hat{\epsilon}^{(0,n,k)}_{\alpha\beta}(\mathbf{k}=0)\hat{\epsilon}^{(0,m,0)}_{\alpha\beta}(\mathbf{k}=0) - \bar{\epsilon}_{\alpha\beta}\hat{\epsilon}^{(0,n,k)}_{\alpha\beta}(\mathbf{k}=0)\right)\Big]s_{n,k}\Bigg\},\end{aligned} \tag{8}$$

where $\bar{\epsilon}_{\alpha\beta}$ is the given mean strain. This expression shows explicitly that the elastic energy in a given microstructure with homogeneous elasticity and coherent interfaces between grains, variants or phases leads to an Ising representation, and the values of the coefficients in Eq. (7) can be directly determined.

C. Description of the underlying workflow

As explained above, we describe the material of interest to be decomposed into "grains", where each of them is entirely in one of the "martensite" states, hence we can describe the entire microstructure through a set of spin variables $\{s_i\}$. We emphasize that the notation as grains does not necessarily require them to be physical grains, but can also be considered as numerical "discretization" unit and also different phases instead of martensite variants can be considered. A simple discretization in this sense is to use little equilateral cuboidal elements, as illustrated for two dimensions in Fig. 1. However, also more complex discretizations are possible and will be discussed in the following. In either way, the elastic energy reduces to combinations of pairwaise interactions between all grains, which follows from the Fourier representation (8) above, which contains only terms up quadratic order in the spin variables s_i; see also Ref. [49]. For the cuboidal discretization in the system with periodic boundary conditions, the advantage is that for both the linear and quadratic Ising coefficients in the representation (7) translation invariance can be employed. This reduces the computational effort drastically, as only one "self energy" for an arbitrary grain has to be computed, as well as the "interaction energy" of one grain with all other grains. For all other grains, one obviously gets the same values. The result of such a calculation is illustrated as heat map in Fig. 2, where the color coding shows the strength of the interaction, i.e., the magnitude of the Ising coefficients J_{ij} for two grains enumerated by i and j. Here, one of the grains is placed in the center of the system, and the interaction energy with all grains is shown. Therefore, the computational effort for calculating the Ising coefficients scales as N, where N is the number of cuboidal grains. This figure shows that besides the translational invariance, also discrete symmetries may be employed, depending on the type of transformation strain.

In contrast, an irregular discretization as in Fig. 3 requires the computation of all interaction energies between all pairs of grains, hence we have a scaling of the effort as N^2. Such a

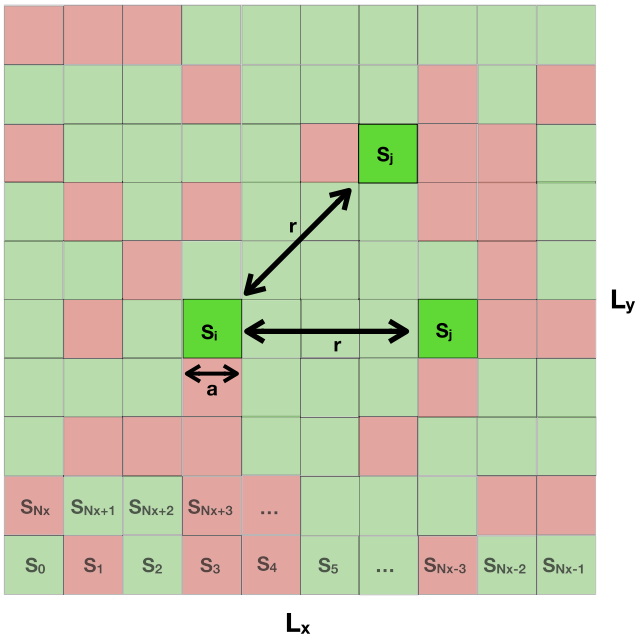

FIG. 1. Two-dimensional discretization of the system using cuboidal "grains."

microstructure could, e.g., be imported from an EBSD mapping of a material of interest. To mimic a realistic microstructure, also a Voronoi tesselation can be used. Here, we use the open source software library voro++ for this purpose [50,51]. We mention in passing that although we use isotropic elasticity, still the eigenstrain can depend on grain orientation. Therefore, we can assign a (random) orientation to each grain in the stage of the Voronoi tesselation, which can then be used for a tensor rotation of the eigenstrain.

For the computation of the Ising coefficients, the derived formula (8) can be used directly. Alternatively, it can be easier to use the strategy described in Ref. [6]. The idea is that one uses explicit settings of the spins by assigning to them values 0 and 1. Then, it is sufficient to perform calculations with (i) all spins being equal to zero, (ii) one single spin being equal to ± 1, whereas all other vanish, and (iii) for calculation of the interaction energies J_{ij} additionally computations with two nonvanishing spins $s_i = s_j = 1$, whereas all other vanish, are needed, see Refs. [5,6] for details.

Additionally, it makes sense to separate the terms with $\mathbf{k} \neq 0$ from the one with $\mathbf{k} = 0$, as the latter is related to a given external strain. These latter terms can be calculated analytically, which has the advantage that a change of the external boundary conditions does not require a (numerically expensive) recomputation of the Ising coefficients.

After calculation of the Ising coefficients J_{ij} and h_i, the problem is ready for implementation on a quantum annealer. Due to the probabilistic nature of the quantum annealing process also higher energy states are found, specially if close low energy states are present. Therefore, a suitable number of repetitions of the process is made and the solution with the lowest detected energy is chosen. In the case that the Ising problems do not match the QPU's architecture, so called chains, i.e., subgraphs of coupled qubits, cover one problem variable through the minor embedding [52,53]. In addition, for large problem sizes hybrid quantum annealing takes additional advantage of combining QPU computations with classical algorithms, allowing for up to 11616 spin variables on the D-Wave Advantage system [52,54,55]. Finally, the resulting spin configuration obtained by the quantum annealing process is visualized according to the generated Voronoi grains.

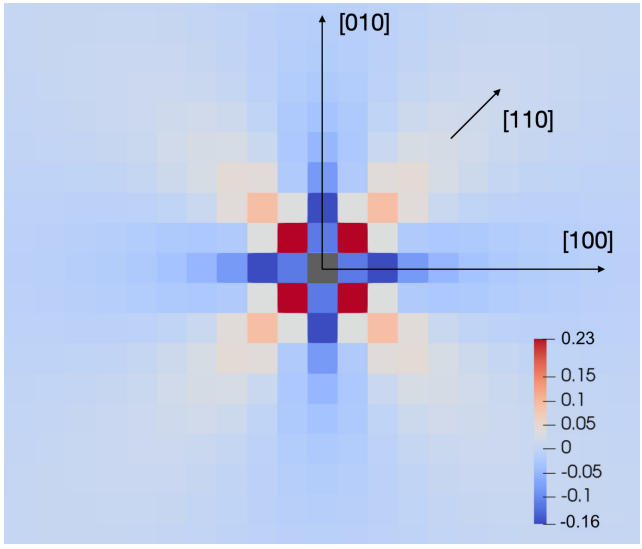

FIG. 2. Each grain can be in the states $s_i = \pm 1$. Interaction energies of two grains of equal variant type ($s_i = s_j$) in the case of a shear eigenstrain, as described by Eq. (14), and vanishing average stress. The interaction energy per length is given in units of $\lambda a^3 \epsilon_0^2$, and the computations were done using a system size of $L_x/a = L_y/a = 50$ with a Poisson ratio of $\nu = 1/4$.

III. RESULTS

In this section we discuss several aspects, applications and extensions of the presented method. First, in Sec. III A we show that even systems with a rather high number of grains can be simulated efficiently with quantum annealing. The second example in Sec. III B investigates possible self organization processes in solid electrolytes for battery applications. In Sec. III C we illustrate how apart from volumetric effects also interfacial energy contributions can be included. Finally, in Sec. III D we emphasize the importance of high precision elasticity calculations and the influence of possible real space interaction cutoffs.

A. Large-scale simulation of equilibrium microstructures

In contrast to microstructure evolution simulation approaches, the present approach aims at determining directly (constrained) equilibrium patterns. Here, the energy can be minimized by properly selecting the variants (or phases) for each grain, depending on the external mechanical load. We show that for quantum annealing simulations with several thousand grains are easily feasible. We note that the total time for determining the ground state configurations for simulations with $N = 2500$ grains, as depicted in Fig. 3, do not

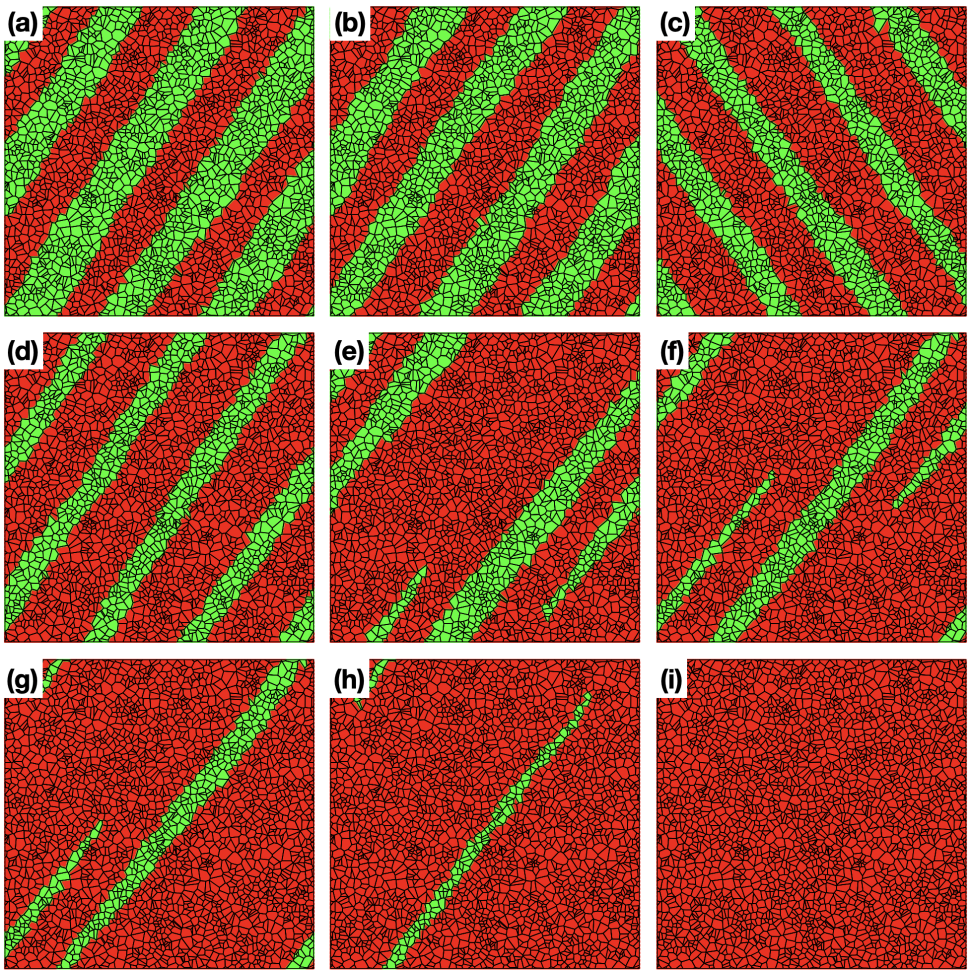

FIG. 3. Equilibrium variant distribution in a microstructure with uniform grain orientation. The microstructures consist of 2500 coherent grains, and a tensile strain is applied in horizontal (x) direction. Red (green) grains correspond to variant $s_i = +1$ ($s_i = -1$), as described through the eigenstrain tensor (9). The tensile strain is (a) $\langle\epsilon_{xx}\rangle/\epsilon_0 = 0$, (b) $\langle\epsilon_{xx}\rangle/\epsilon_0 = 0.165$, (c) $\langle\epsilon_{xx}\rangle/\epsilon_0 = 0.495$, (d) $\langle\epsilon_{xx}\rangle/\epsilon_0 = 0.66$, (e) $\langle\epsilon_{xx}\rangle/\epsilon_0 = 0.825$, (f) $\langle\epsilon_{xx}\rangle/\epsilon_0 = 0.99$, (g) $\langle\epsilon_{xx}\rangle/\epsilon_0 = 1.155$, (h) $\langle\epsilon_{xx}\rangle/\epsilon_0 = 1.305$, and (i) $\langle\epsilon_{xx}\rangle/\epsilon_0 = 1.32$. The Poisson ratio is $\nu = 1/4$.

require more than roughly one minute on a D-Wave quantum annealer if a hybrid solver is used (the system is too big for a pure quantum annealer solution); in fact, the pure QPA access time is significantly lower. However, one has to keep in mind that the Ising coefficients need to be precomputed, and this becomes then the computationally expensive part, as $\sim N^2$ interactions need to be calculated with high precision.

In the presented case, we distinguish between two martensite variants, hence one spin variable per grain is required. The eigenstrain is given as

$$\epsilon^{(0)}_{\alpha\beta} = s_i \begin{pmatrix} \epsilon_0 & 0 & 0 \\ 0 & -\epsilon_0 & 0 \\ 0 & 0 & \epsilon_0 \end{pmatrix} \tag{9}$$

in each grain, relative to the austenitic phase, without consideration of a grain rotation. The strength of the transformation is controlled by the parameter ϵ_0, and additionally a varying tensile strain is applied in lateral (x) direction. Figure 3 shows the resulting variant distribution of equally orientated grains for different strain strengths. For a vanishing tensile strain, stripe patterns arise, which are discussed in more detail in Ref. [5]. For increasing strain, the stripes are getting thinner, until they are not connecting anymore. A criticial strain of about $\langle\epsilon_{xx}\rangle/\epsilon_0 \approx 1.32$ [see panel (i)] leads to a uniform microstructure, i.e., only red grains with $s_i = +1$ remain.

The result shows that even with a straightforward generalization to 3D structures it is possible to have sufficiently large number of grains in each spatial direction, and therefore the approach is well suited to generate strain dependent microstructures for representative volume elements.

B. Solid electrolyte $Li_7La_3Zr_2O_{12}$ (LLZO)

$Li_7La_3Zr_2O_{12}$ (LLZO) is a promising ceramic material which can be used as electrolyte in all-solid-state batteries. It has a high-ionic conductivity and can be used with lithium as anode material, hence allowing for a high-energy density and stability against failure. However, the room temperature equilibrium phase of LLZO is a tetragonal phase, which has a much lower Li ion conductivity than the metastable cubic phase. The latter can be stabilized by alloying, e.g., with Ta at increased costs. Therefore, it is desirable to perform such dopings only to a minimum amount. From a thermodynamic perspective, the doping level determines the phase fractions of

the cubic and tetragonal phases, but does not make predictions for their spatial alignment, as the (bulk) chemistry depends only on the overall volume fractions but not the arrangement.

In this section we aim to investigate to which extent elastic effects, which arise due to the misfit between tetragonal and cubic grains, can affect their equilibrium arrangement by minimization of the elastic energy. This may in the future enable a "grain engineering" by enabling a self-organization process, if "channels" of the cubic phase inside a tetragonal matrix could lead to increased ionic conductivity through percolation. To stay in the framework of the presented theoretical approach, we make a number of simplifying assumptions to keep the description simple and to rather sketch a possible way for future optimized electrolyte fabrication. In detail, the assumptions are: (i) We assume all grains to be equally oriented. (ii) The grains are coherently connected and we use the same (isotropic) elastic constants for both phases. (iii) We consider for simplicity apart from the cubic phase (spin -1) only one tetragonal variant (spin $+1$). (iv) The description is two-dimensional with a plane strain setup.

Points (i) and (ii) are probably the most serious restrictions of the current description, and therefore we expect the predictions to be rather qualitative and setting an upper bound to the possible influence of elastic effects. The assumptions (iii) and (iv) are only technical simplifications, and a generalization to a full three-dimensional description with more variants is in the spirit of the general approach described above and mainly increases the computational effort.

Concerning the description of the mechanical properties of LLZO, we refer to the previous work [47,48,56]. The lattice parameters for tetragonal LLZO, which is stable at ambient temperature, are given as $a_{\mathrm{tet}} = 13.1846\,\text{Å}$ and $c_{\mathrm{tet}} = 12.6390\,\text{Å}$. In the desired cubic case the lattice parameter is given as $a_{\mathrm{cub}} = 13.03286\,\text{Å}$. We employ the previous definition of the eigenstrain [Eq. (4)] with two variants, $K = 1$, and N grains. Then, the resulting eigenstrain reads

$$\epsilon^{(0)}_{\alpha\beta}(\mathbf{r}) = \sum_{n}^{N} \theta_n(\mathbf{r})\left(s_1^{(n)}\epsilon^{(0,n,1)}_{\alpha\beta} + \epsilon^{(0,n,0)}_{\alpha\beta}\right), \tag{10}$$

with eigenstrain tensor components $\epsilon^{(0,n,1)}_{\alpha\beta}$ and constant eigenstrain offset $\epsilon^{(0,n,0)}_{\alpha\beta}$. We use the cubic phase ($s = -1$) as reference state, hence $\epsilon^{(0)}_{\alpha\beta} = 0$ in such a grain, whereas in a tetragonal grain we have

$$\begin{aligned}\epsilon^{(0)}_{\alpha\beta} &= \begin{pmatrix} \frac{a_{\mathrm{tet}}-a_{\mathrm{cub}}}{a_{\mathrm{cub}}} & 0 & 0 \\ 0 & \frac{c_{\mathrm{tet}}-a_{\mathrm{cub}}}{a_{\mathrm{cub}}} & 0 \\ 0 & 0 & \frac{a_{\mathrm{tet}}-a_{\mathrm{cub}}}{a_{\mathrm{cub}}} \end{pmatrix} \\ &= \begin{pmatrix} 0.011643 & 0 & 0 \\ 0 & -0.030221 & 0 \\ 0 & 0 & 0.011643 \end{pmatrix}. \end{aligned} \tag{11}$$

These relations allow to uniquely determine $\epsilon^{(0,n,1)}_{\alpha\beta}$ and $\epsilon^{(0,n,0)}_{\alpha\beta}$. The elastic properties are—in isotropic approximation—described to good accuracy with a Poisson ratio $\nu = 1/4$ as before.

Besides the mechanical component, which is responsible for the spatial arrangement of the phases, also a chemical component is important, as it fixes the volume fraction of the phases. Such a perspective is based on the picture that the chemical energy is higher than the elastic energy. However, in general also chemomechanical couplings can play a role if both energy contributions are of a comparable order of magnitude. In this case, it is also possible that strong mechanical misfits affect the phase fractions, as a reduction of the elastic energy can be stronger than a deviation from the equilibrium partitioning from a purely chemical perspective. To qualitatively study such transitions, we add a description of the chemical contribution to the free energy and treat the coefficients in this energy term as adjustable parameters.

To lowest order, a deviation of the chemical free energy from a situation with equilibrium phase fractions is quadratic in the volume fraction deviation. Hence, this energy contribution can be written as

$$\begin{aligned}\Delta E &= V\gamma\left(\sum_{i=1}^{N} f_i s_i - f\right)^2 \\ &= 2V\gamma\sum_{i<j}^{N} f_i f_j s_i s_j - 2V\gamma f\sum_{i}^{N} f_i s_i + \text{const.} \end{aligned} \tag{12}$$

Here, f is a parameter quantifying the expected equilibrium volume fraction of the two phases, which is controlled by the alloying, as described above. It ranges between -1 for a purely cubic and $+1$ for a tetragonal system. Therefore, in particular $f = 0$ corresponds to equal volume fractions of the two phases. The parameter f_i is the volume fraction of grain i, hence $\sum_i^N f_i = 1$ holds. Finally, γ controls the strength of the chemical energy contribution. It relates the curvature of the composition dependent chemical free energy curves to the elastic contribution, and can therefore be used to tune between a chemically and a mechanically dominated system. As the chemical energy expression (12) is quadratic in the spin variable s_i, it can directly be implemented on the quantum annealer, together with the elastic contribution. The quantum annealing calculations are then performed via hybrid computations, which allow to reliably find the ground state even for larger systems.

Figure 4 shows the resulting equilibrium variant distribution. In all panels the same Voronoi tesselated microstructure with 100 grains is used. Furthermore, all grains have the same orientation, hence the same eigenstrain (11) is used for all of them. As mechanical boundary conditions we use vanishing average strain, $\langle\epsilon_{\alpha\beta}\rangle = 0$. In horizontal direction the weighting parameter γ and in vertical direction phase fraction parameter f is varied. Here, green (red) grains correspond to the cubic (tetragonal) phase. The patterns in Figs. 4(a)– 4(d) consist only of the cubic grains due the choice $f = -1$ in the chemical energy. We note that in this state the system is stress free due to the chosen mechanical boundary condition $\langle\epsilon_{\alpha\beta}\rangle = 0$. All pictures in the right column [Figs. 4(d), 4(h), 4(l), and 4(p)] correspond to $\gamma = 0$, which means that the chemical energy contribution is absent. As then the energy consists only of the elastic contribution, the system becomes completely cubic in this case due to the chosen reference of vanishing eigenstrain in the cubic phase. In contrast, the

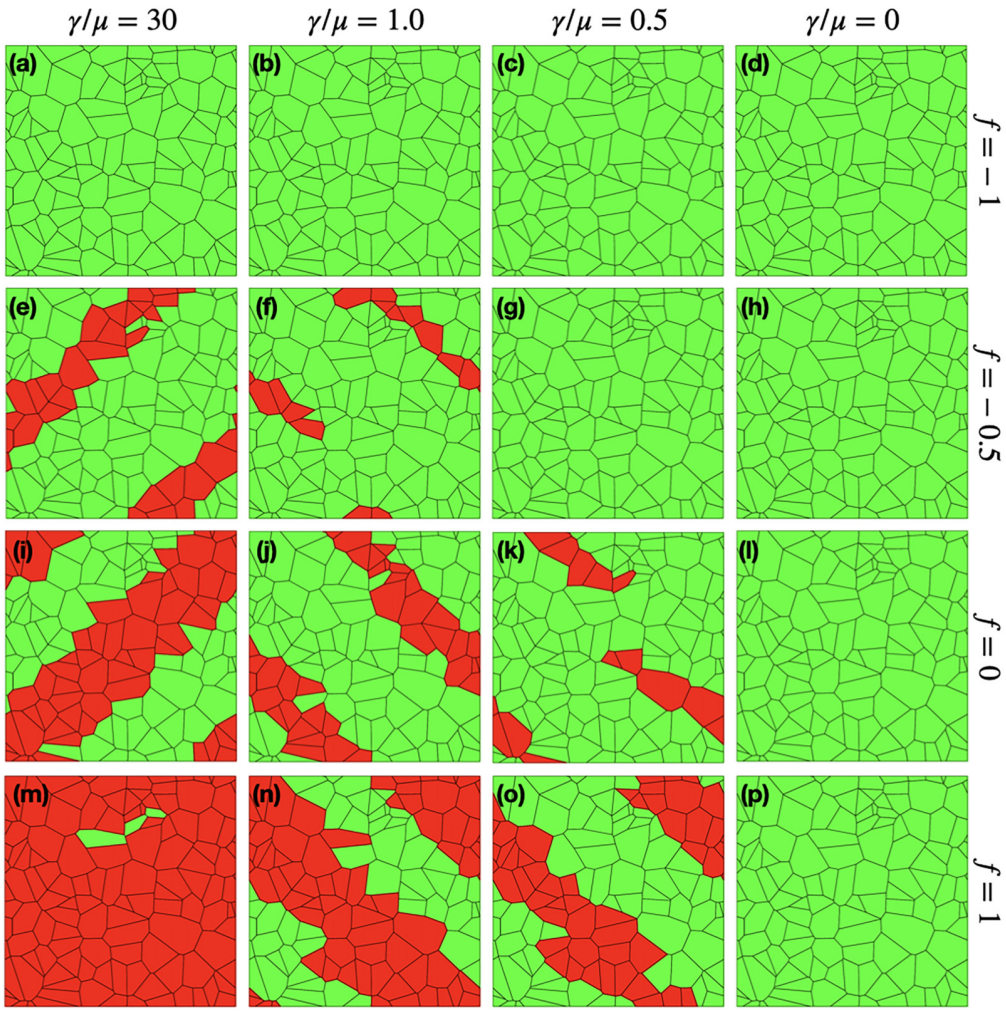

FIG. 4. Equilibrium phase distribution of tetragonal and cubic phases in LLZO for grains with uniform orientation. The microstructures consist of 100 grains and the parameters γ and f are varied. Red grains correspond to $s_i = +1$, i.e., the tetragonal phase, green to $s_i = -1$, which is the cubic phase.

chemical energy dominates for the cases in the left column [Figs. 4(a), 4(e), 4(i), and 4(m)], and then the volume fractions are close to the expected value f from the chemical perspective. Nevertheless, the elastic contribution is still sufficient to favor an ordering as inclined stripes similar to the above situation in Fig. 3, with an orientation as expected from the analysis in Ref. [5]. Also, a small cubic island remains even in the case $f = 1$ in Figs. 4(m). In the bottom row, the chemical contribution favors purely tetragonal systems ($f = 1$), whereas the elastic energy favors the cubic state due the the mechanical boundary conditions. In this extreme case the volume fractions are then strongly controlled by the weighting parameter γ/μ. For intermediate values, where two-phase structures are found, the strip patterns are are more rugged in comparison to the patterns in Fig. 3, which is mainly due to the smaller number of grains. For all other cases, as, e.g., for the row $f = 0$, where from a chemical perspective equal volume fractions of the phases are expected, the overall energy minimization including elastic contributions lead to deviations from this expectation, hence highlighting the aforementioned strong chemomechanical coupling.

As a consequence we observe indeed a tendency for the formation of ion conducting channels through the presence of elastic effects for suitable mechanical boundary conditions. However, it has to be pronounced that here all grains are assumed to have the same orientation, and therefore also the tetragonal distortion leads to an expansion in both x and z direction. As long as the orientation remains in this plane by a grain rotation, the eigenstrain tensor (11) remains invariant, hence favoring such a self-organization process toward an increased ionic conductivity of the solid electrolyte.

C. Interfacial energy

So far, we have considered with the elastic and chemical contributions only bulk energies. As a consequence, there is no selection of a length scale. In other words, a rescaling of the pattern (including a change of the grain size) will lead to identical patterns, and only the total energy changes according to its proportionality to the system volume.

The inclusion of interfacial contributions therefore leads to new physical effects, as—depending on the length scale—the

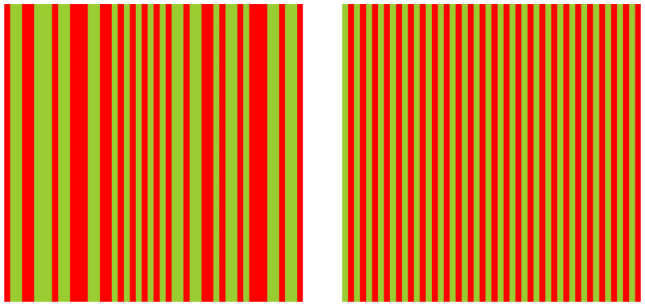

FIG. 5. Equilibrated microstructures for zero average strain and shear transformations with vanishing and negative interfacial energy in a system of 50×50 cuboidal grains. Left: $\sigma/\mu\epsilon_0^2 a = 0$, right: $\sigma/\mu\epsilon_0^2 a = -1$. The length is measured in multiples of the lattice unit a, the Poisson ratio is $\nu = 1/4$.

bulk and interface energies can compete. In fact, with the interfacial energy density (per area) σ, the ratio σ/μ sets a characteristic length scale. For a positive value of σ we expect a coarsening tendency of the microstructure, and hence in equilibrium the amount of interfaces shall be minimized in particular if the interfacial energy dominates.

To formulate an interfacial energy (per unit length in 2D) in the spirit of an Ising model for the quantum annealer, we use a nearest-neighbor interaction, which penalizes interfaces between different variants, using

$$E_{\text{interface}} = \frac{1}{2} \sum_{i,j(\text{NN})} a_{ij} \tilde{\sigma}_{ij} (1 - s_i s_j), \tag{13}$$

where a_{ij} is the interface length between grain i and j and $\tilde{\sigma}_{ij}$ is the interfacial energy for this pairs of grains. The formulation (13) is for general anisotropic interface energies, and for demonstrational purposes we focus here on the isotropic case with $\tilde{\sigma}_{ij} \equiv \sigma$ for all interfaces. The summation in this formula is limited to nearest-neighbor (NN) pairs, but also generalizations to longer ranged interactions are conceivable to mimic additional interactions.

As a simple illustration we use first the case of a shear transformation with eigenstrain

$$\epsilon^{(0)}_{\alpha\beta} = s_i \begin{pmatrix} 0 & \epsilon_0 & 0 \\ \epsilon_0 & 0 & 0 \\ 0 & 0 & 0 \end{pmatrix}, \tag{14}$$

which was conceptually discussed from point of view of elastic effects in Ref. [5]. If we use a discretization by equally sized cubes (hence, all $a_{ij} = a$) without interfacial effects, $\sigma = 0$, then the equilibrium pattern for fixed and vanishing average strain boundary conditions, $\langle \epsilon_{\alpha\beta} \rangle = 0$, are horizontal or vertical stripes with equal volume fractions of the two variants, hence the microstructure is effectively one-dimensional. In this case, the entire pattern is stress free, as in each lamella $\epsilon_{\alpha\beta} = \epsilon^{(0)}_{\alpha\beta}$. Consequently, an arbitrary arrangement of stripes with equal amounts of the red and green phases minimizes the elastic energy to zero; see left panel of Fig. 5. Consequently, the selection among all the possible stripe patterns becomes entirely through the interfacial energy for $\sigma \neq 0$. Thus, for $\sigma > 0$ the system minimizes the total energy by having a stripe pattern with as few interfaces as possible. With the condition $\langle \epsilon_{\alpha\beta} \rangle = 0$ we therefore obtain two equally sized red and green stripes, provided that the interfacial energy is not too high that even a strained single phase pattern is favorable. In turn, for a negative interfacial energy $\sigma < 0$ the optimal microstructure consists of a regular array of lamellae with minimum width a; see right panel in Fig. 5.

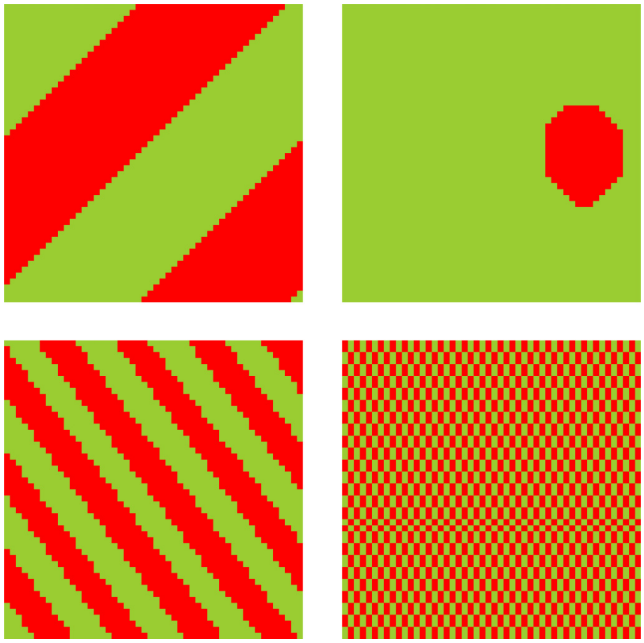

FIG. 6. Top row: Equilibrated microstructures for zero average strain and tetragonal transformations with different values of positive interfacial energy in a system of 50×50 cuboidal grains. Left: $\sigma/\mu\epsilon_0^2 a = 1$, right: $\sigma/\mu\epsilon_0^2 a = 9$. Bottom row: The same for negative interfacial energy: Left: $\sigma/\mu\epsilon_0^2 a = -0.06$, right: $\sigma/\mu\epsilon_0^2 a = -0.07$. The length is measured in multiples of the lattice unit a, the Poisson ratio is $\nu = 1/4$.

For a tetragonal eigenstrain, see Eq. (9), patterns with regular inclined stripes for $\langle \epsilon_{\alpha\beta} \rangle = 0$ similar to Figs. 3 and 4 appear without interfacial energy. For a positive interfacial energy $\sigma > 0$, an increasing value of σ first leads to a reduction of the number of stripes as well as a rotation of the stripes to comply with the periodic boundary conditions (see top row of Fig. 6). A higher value of the interfacial energy destroys this morphology and leads to patterns with unequal amounts of the variants, as the interfacial energy overweights the elastic effects, though the latter alone would favor configurations where the mean eigenstrain vanishes due to the boundary condition. In a narrow intermediate parameter range, the appearing pattern contains a nucleus of one variant inside a matrix of the other one (see top right panel of Fig. 6). The elastic energy stabilizes the nucleus for the same argument as just above, whereas the interfacial energy balances this contribution and favors the disappearance of the nucleus. For even higher values of σ the system becomes single phased due to the dominance of the interfacial energy. For negative interfacial energy, patterns with more interfaces become favorable (see bottom row of Fig. 6). Initially, this leads to an increase of the stripe density and change of the orientation angle with decreasing interfacial energy, which

then start to become unstable up to the point where the lamellar microstructure is entirely destroyed. This transition occurs within a very narrow range of interfacial energies.

D. Discussion on the elastic energy calculation

The key element of the quantum-annealer-based determination of the elastic ground state microstructure is the formulation via pairwise interactions in the Ising formulation. An example for the interaction coefficients J_{ij} is shown in Fig. 2. This heatmap shows that the interactions with the closest neighbors is highest and decays with the distance between the grains. Depending on the dimension of the system, the elastic interactions decay asymptotically either as $1/r^2$ in 2 dimensions or $1/r^3$ in 3D. There are similarities to the computations of long ranged Coulomb interactions, e.g., for molecular dynamics simulations, which require the use of Ewald summation techniques to properly capture the long range tails of the interactions in periodic systems. Therefore, also here the use of a real space cutoff for the elastic grain-grain interactions is critical, although the interactions seem to decay quickly.

To emphasize this effect, we consider again the shear transformation case (14), which leads to stripe patterns; see Fig. 5. As mentioned before, this example can be solved analytically easily, as having a vanishing stress in each stripe by $\epsilon_{\alpha\beta} = \epsilon^{(0)}_{\alpha\beta}$ leads to a completely stress free case, which is compatible with both the boundary conditions $\langle\sigma_{\alpha\beta}\rangle = 0$ and $\langle\epsilon_{\alpha\beta}\rangle = 0$, provided that the volume fractions of the two variants is equal. However, from the picture of pairwise interactions in the Ising representation this solution is not obvious. As all the Ising coefficients are different from zero, it is an almost miraculous cancellation of all $N(N-1)/2$ mutual interactions, such that the total elastic energy is exactly zero (apart from a constant offset, which is typically not considered for the annealer formulation). If now the range of the interactions is artificially cut off, then it cannot be expected that the elastic energy agrees with the analytical calculation.

To illustrate this effect, we set up a regular stripe microstructure manually in a system discretized by 50×50 cuboidal grains with a given lamella thickness λ. Additionally, we impose an artificial cutoff to the range of the interactions by setting $J_{ij} = 0$ beyond a given separation of the considered grains. Figure 7 shows the resulting elastic energy, as computed from the truncated Ising summation for different stripe thicknesses λ. In all cases we see that the expected energy $E = 0$ is only reached without a cutoff (in the periodic system, this is achieved if the range of the interaction is taken at least half the system length, which is 25 in the example). With the cutoff, the energy is obtained incorrectly, and then also the quantum annealer is obviously not able to find the physically correct ground state configuration. Qualitatively, the energy is close to the expected value, if the cutoff range is significantly larger than the stripe thickness λ, but as in general the equilibrium microstructure can only be obtained based on exact Ising coefficients, we can therefore conclude that the use of any cutoff for the elastic interaction energy calculation is not appropriate.

Apart from the issue of a real space cutoff, also possible numerical rounding errors have to be considered. As the elastic energy is represented through a summation over $\sim N^2$ terms, even small errors can lead in total to improper results. For the shear transformation example, the grain-grain interaction at a distance of 20 lattice units in [100] direction has decayed to about 2% of the maximum interaction strength at next-to-nearest-neighbor interactions (see Fig. 2). To illustrate the potential influence of numerical inaccuracies, a random noise of this strength is added artificially to all considered pair interaction coefficients, leading to modified total energies, which do not converge to the analytical result without cutoff anymore; see Fig. 7. Therefore, the comparison to an analytically known solution like the stripe patterns can help to identify possible rounding errors.

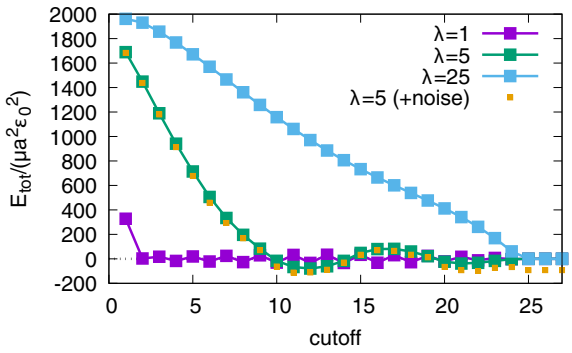

FIG. 7. Total elastic energy as expressed through the Ising summation for a regular lamellar structure with strip width λ as function of the real space interaction cutoff. The correct elastic energy $E_{\text{tot}} = 0$ is reached only without cutoff, i.e., larger than half of the system size, which is 25 here. For the case with noise, an uncorrelated random variable with uniform distribution, vanishing mean value and maximum magnitude of 2% of the strongest grain-grain interaction in [100] interactions is added to all interaction parameters J_{ij} up to the cutoff distance, leading to an inappropriate total energy even without cutoff.

In many cases, the ground state configuration is unique, but for example for the shear transformation with the irregular "barcode" patterns as in Fig. 5, the ground state is strongly degenerate. Therefore, the Ising coefficients need to computed with very high accuracy in order not to introduce spurious biases. We indeed obtain for high resolution Fourier transformation computed interaction coefficients always different patterns by the quantum annealer, which is an indication for proper representation of the elastic energy through the Ising summation. In essence, a precise calculation of the interaction energy is therefore essential, and rough estimated, e.g., based on the proper long distance asymptotics, not sufficient.

IV. CONCLUSION AND OUTLOOK

The present paper's central result is the extended description and investigation of the underlying elastic calculations of the microstructure optimization via quantum annealing. We describe the underlying calculations of long-ranged elastic interactions in reciprocal space and show the resulting direct Ising formulation for the quantum annealer. Large scale simulations of equilibrium microstructures with 2500 grains and varying tensile strain result in the expected stripe

patterns, which are getting thinner for increasing strain. Here, the quantum annealing part requires just roughly one minute of computing time and presents no drastically increase with increasing system sizes. This shows that also a generalization to 3D structures with huge system sizes and therefore the generation of microstructures with representative volume elements is possible.

The application of the quantum annealing microstructure equilibration to the solid electrolyte LLZO includes a chemical energy component, which competes with the elastic energy and influences the resulting microstructures. In essence, the elastic effects favor a formation of ion conducting channels through a self-organization process for suitable mechanical boundary conditions. We note that these findings are based on a number of simplifying assumptions, but future investigations may extend the model's complexity toward an optimization of solid electrolytes. Therefore, this application is a promising step toward quantum-computing-based material design.

Further extensions include interfacial contributions to investigate the competition between bulk and interface energies and their influence on the microstructure formation.

The truncation of the elastic interaction range through a real space cutoff is tempting, however, we show that this is not useful due to an artificial scale selection, which results in improper microstructure predictions. Therefore, all interactions between the grains have to be taken into account with high accuracy. Fortunately, this is possible on the quantum annealer without great losses in computing time also for large system sizes.

ACKNOWLEDGMENTS

This work was funded by the German Federal Ministry of Education and Research (BMBF) via the project ALANO (Grant No. 13XP0396B) and the Helmholtz project ZeDaBase. Open access was funded by the Deutsche Forschungsgemeinschaft (DFG, German Research Foundation) Grant No. 491111487. The authors gratefully acknowledge the Jülich Supercomputing Centre [57] for funding this project by providing computing time on the D-Wave Advantage System JUPSI through the Jülich UNified Infrastructure for Quantum computing (JUNIQ).

APPENDIX: DERIVATION OF THE ELASTIC ENERGY

In this Appendix we determine the elastic equilibrium state for a given eigenstrain distribution and express the elastic energy for this equilibrated state in reciprocal space.

Generally, the Fourier transformation of a (real) function $f(\mathbf{r})$ is denoted as

$$\hat{f} = \frac{1}{V}\int_V f(\mathbf{r})\exp(i\mathbf{kr})\,d\mathbf{r}, \tag{A1}$$

inside a periodic cuboidal system with volume $V = L_x \times L_y \times L_z$. Then, the back transformation reads

$$f(\mathbf{r}) = \sum_{\mathbf{k}} \hat{f}(\mathbf{k})\exp(-i\mathbf{kr}), \tag{A2}$$

using the reciprocal lattice vectors

$$\mathbf{k} = 2\pi\left(\frac{n_x}{L_x}, \frac{n_y}{L_y}, \frac{n_z}{L_z}\right), \quad n_i \in \mathbb{Z}. \tag{A3}$$

The orthogonality between the base functions is expressed through Parseval's theorem, which holds for arbitrary functions $f_1(\mathbf{r})$, $f_2(\mathbf{r})$ and their Fourier transforms $\hat{f}_1(\mathbf{k})$, $\hat{f}_2(\mathbf{k})$,

$$\frac{1}{V}\int_V f_1(\mathbf{r})f_2(\mathbf{r})\,d\mathbf{r} = \sum_{\mathbf{k}} \hat{f}_1(\mathbf{k})\hat{f}_2^*(\mathbf{k}), \tag{A4}$$

where the star denotes complex conjugation. For numerical implementations, Fast Fourier libraries like FFTW can be used [58].

The strain can be split into a homogeneous (macroscopic shape deformation) and heterogeneous part [59]

$$\epsilon_{\alpha\beta}(\mathbf{r}) = \bar{\epsilon}_{\alpha\beta} + \delta\epsilon_{\alpha\beta}(\mathbf{r}). \tag{A5}$$

The homogeneous strain $\bar{\epsilon}_{\alpha\beta}$ is then defined such that the mean value of the fluctuation part vanishes,

$$\langle\delta\epsilon_{\alpha\beta}(\mathbf{r})\rangle = \frac{1}{V}\int_V \delta\epsilon_{\alpha\beta}(\mathbf{r})\,dV = 0. \tag{A6}$$

Similarly, we split the elastic energy into a contribution E_1 which does not contain the fluctuations $\delta\epsilon_{\alpha\beta}$ and the remaining part E_2,

$$E_1 = \int_V \left(\frac{\lambda}{2}\left(\bar{\epsilon}_{\alpha\alpha} - \epsilon^{(0)}_{\alpha\alpha}(\mathbf{r})\right)^2 + \mu\left(\bar{\epsilon}_{\alpha\beta} - \epsilon^{(0)}_{\alpha\beta}(\mathbf{r})\right)^2\right) d\mathbf{r} \tag{A7}$$

and

$$E_2 = \int_V \left(\frac{\lambda}{2}\left(\delta\epsilon^2_{\alpha\alpha}(\mathbf{r}) - 2\epsilon^{(0)}_{\alpha\alpha}(\mathbf{r})\delta\epsilon_{\beta\beta}(\mathbf{r})\right) + \mu\left(\delta\epsilon^2_{\alpha\beta}(\mathbf{r}) - 2\epsilon^{(0)}_{\alpha\beta}(\mathbf{r})\delta\epsilon_{\alpha\beta}(\mathbf{r})\right)\right) d\mathbf{r}, \tag{A8}$$

hence $E_{\mathrm{el}} = E_1 + E_2$.

Elastic equilibrium can be expressed through the minimization of the energy. Since E_1 and E_2 are functionals of independent degrees of freedom, the minimzation of E_{el} requires the separate minimization of E_1 and E_2. Here, we distinguish between two cases, namely (i) vanishing mean stress, $\langle\sigma_{\alpha\beta}\rangle = 0$, and (ii) given average mean strain, $\langle\epsilon_{\alpha\beta}\rangle = \bar{\epsilon}_{\alpha\beta}$.

In case (i) the elastic energy is minimized with respect to the (total) displacement components as degrees of freedom. This includes the minimization of E_1 with respect to the homogeneous strain contributions $\bar{\epsilon}_{\alpha\beta}$,

$$\frac{\partial E_1}{\partial\bar{\epsilon}_{\alpha\beta}} = \int_V \left[\lambda\delta_{\alpha\beta}\left(\bar{\epsilon}_{\gamma\gamma} - \epsilon^{(0)}_{\gamma\gamma}(\mathbf{r})\right) + 2\mu\left(\bar{\epsilon}_{\alpha\beta} - \epsilon^{(0)}_{\alpha\beta}(\mathbf{r})\right)\right] d\mathbf{r} = 0. \tag{A9}$$

By definition the mean stress is given in the isotropic case as

$$\bar{\sigma}_{\alpha\beta} = \langle\sigma_{\alpha\beta}(\mathbf{r})\rangle = \lambda\delta_{\alpha\beta}\left(\bar{\epsilon}_{\gamma\gamma} - \left\langle\epsilon^{(0)}_{\gamma\gamma}(\mathbf{r})\right\rangle\right) + 2\mu\left(\bar{\epsilon}_{\alpha\beta} - \langle\epsilon^{(0)}_{\alpha\beta}(\mathbf{r})\rangle\right), \tag{A10}$$

and therefore the minimization condition (A9) can be read as

$$\langle\sigma_{\alpha\beta}(\mathbf{r})\rangle = 0, \tag{A11}$$

which is in agreement with the desired boundary condition of vanishing mean stress, hence

$$\bar{\epsilon}_{\alpha\beta} = \left\langle \epsilon^{(0)}_{\alpha\beta}(\mathbf{r}) \right\rangle = \hat{\epsilon}^{(0)}_{\alpha\beta}(\mathbf{k}=0). \tag{A12}$$

For the minimization of E_2 we represent the strain variation $\delta\epsilon_{\alpha\beta}$ through the displacement field u_α,

$$\delta\epsilon_{\alpha\beta} = \frac{1}{2}\left(\frac{\partial u_\alpha}{\partial x_\beta} + \frac{\partial u_\beta}{\partial x_\alpha}\right), \tag{A13}$$

as the minimization has to be done with respect to u_α as independent degrees of freedom. Furthermore, we introduce the stress fluctuation

$$\delta\sigma_{\alpha\beta}(\mathbf{r}) = \lambda\delta_{\alpha\beta}\delta\epsilon_{\gamma\gamma}(\mathbf{r}) + 2\mu\,\delta\epsilon_{\alpha\beta}(\mathbf{r}) \tag{A14}$$

and the eigenstress

$$\sigma^{(0)}_{\alpha\beta} = \lambda\delta_{\alpha\beta}\epsilon^{(0)}_{\gamma\gamma} + 2\mu\epsilon^{(0)}_{\alpha\beta} \tag{A15}$$

as abbreviations. Then, the energy E_2 is minimized with respect to u_α,

$$\frac{\delta E_2}{\delta u_\alpha} = -\frac{\partial}{\partial x_\beta}\left(\delta\sigma_{\alpha\beta}(\mathbf{r}) - \sigma^{(0)}_{\alpha\beta}(\mathbf{r})\right) = 0, \tag{A16}$$

which is the expected stress balance. In reciprocal space this relation reads

$$G^{-1}_{\alpha\beta}\hat{u}_\beta = -ik_\beta\hat{\sigma}^{(0)}_{\beta\alpha}, \tag{A17}$$

with the inverse isotropic Green tensor

$$G^{-1}_{\beta\delta} = \lambda k_\beta k_\delta + \mu k_\alpha k_\alpha \delta_{\beta\delta} + \mu k_\beta k_\delta. \tag{A18}$$

By inversion we therefore get the solution (for $\mathbf{k} \neq 0$)

$$\hat{u}_\alpha = -iG_{\alpha\gamma}k_\beta\hat{\sigma}^{(0)}_{\beta\gamma}. \tag{A19}$$

For a two-dimensional plane strain setup we get explicitly for this tensor

$$G_{2D} = \frac{1}{\mu(\lambda+2\mu)k^4} \times \begin{pmatrix} (\lambda+\mu)k_y^2 + \mu k^2 & -(\lambda+\mu)k_xk_y \\ -(\lambda+\mu)k_xk_y & (\lambda+\mu)k_x^2 + \mu k^2 \end{pmatrix}, \tag{A20}$$

with $\mathbf{k} = (k_x, k_y)$ and $k = |\mathbf{k}|$. Inserting the (general) solution into the energy expressions gives in reciprocal space by using Parseval's theorem (A4)

$$E_1 = \frac{\lambda V}{2}\sum_{\mathbf{k}\neq 0}\hat{\epsilon}^{(0)}_{\alpha\alpha}(\mathbf{k})\hat{\epsilon}^{(0)*}_{\beta\beta}(\mathbf{k}) + \mu V\sum_{\mathbf{k}\neq 0}\hat{\epsilon}^{(0)}_{\alpha\beta}(\mathbf{k})\hat{\epsilon}^{(0)*}_{\alpha\beta}(\mathbf{k}) \tag{A21}$$

and

$$\begin{aligned} E_2 = {} & \frac{\lambda V}{2}\sum_{\mathbf{k}\neq 0}\delta\hat{\epsilon}_{\alpha\alpha}(\mathbf{k})\delta\hat{\epsilon}^*_{\beta\beta}(\mathbf{k}) - \lambda V\sum_{\mathbf{k}\neq 0}\hat{\epsilon}^{(0)*}_{\alpha\alpha}(\mathbf{k})\delta\hat{\epsilon}_{\beta\beta}(\mathbf{k}) \\ & + \mu V\sum_{\mathbf{k}\neq 0}\delta\hat{\epsilon}_{\alpha\beta}(\mathbf{k})\delta\hat{\epsilon}^*_{\alpha\beta}(\mathbf{k}) \\ & - 2\mu V\sum_{\mathbf{k}\neq 0}\hat{\epsilon}^{(0)*}_{\alpha\beta}(\mathbf{k})\delta\hat{\epsilon}_{\alpha\beta}(\mathbf{k}), \end{aligned} \tag{A22}$$

using

$$\delta\hat{\epsilon}_{\alpha\beta} = \tfrac{1}{2}(ik_\alpha\hat{u}_\beta + ik_\beta\hat{u}_\alpha). \tag{A23}$$

The total elastic energy expression can then be further simplified to

$$E_{\mathrm{el}} = \frac{V}{2}\sum_{\mathbf{k}\neq 0}\left[\hat{\sigma}^{(0)*}_{\alpha\beta}(\mathbf{k})\hat{\epsilon}^{(0)}_{\alpha\beta}(\mathbf{k}) - \hat{\sigma}^{(0)}_{\alpha\gamma}(\mathbf{k})k_\alpha G_{\gamma\beta}k_\delta\hat{\sigma}^{(0)*}_{\beta\delta}(\mathbf{k})\right]. \tag{A24}$$

For case (ii), i.e., given mean strain conditions, $\bar{\epsilon}_{\alpha\beta}$ is not a degree of freedom, and therefore the variation of E_1 is not needed. Then we get for E_1

$$\begin{aligned} E_1 = {} & \frac{\lambda V}{2}\sum_{\mathbf{k}\neq 0}\hat{\epsilon}^{(0)}_{\alpha\alpha}(\mathbf{k})\hat{\epsilon}^{(0)*}_{\beta\beta}(\mathbf{k}) + \mu V\sum_{\mathbf{k}\neq 0}\hat{\epsilon}^{(0)}_{\alpha\beta}(\mathbf{k})\hat{\epsilon}^{(0)*}_{\alpha\beta}(\mathbf{k}) \\ & + \frac{\lambda V}{2}\left(\bar{\epsilon}_{\alpha\alpha} - \hat{\epsilon}^{(0)}_{\alpha\alpha}(\mathbf{k}=0)\right)^2 \\ & + \mu V\left(\bar{\epsilon}_{\alpha\beta} - \hat{\epsilon}^{(0)}_{\alpha\beta}(\mathbf{k}=0)\right)^2, \end{aligned} \tag{A25}$$

whereas E_2 remains unaffected. Finally, we therefore get for the total elastic energy

$$\begin{aligned} E_{\mathrm{el}} = {} & \frac{V}{2}\sum_{\mathbf{k}\neq 0}\left[\hat{\sigma}^{(0)*}_{\alpha\beta}(\mathbf{k})\hat{\epsilon}^{(0)}_{\alpha\beta}(\mathbf{k}) - \hat{\sigma}^{(0)}_{\alpha\gamma}(\mathbf{k})k_\alpha G_{\gamma\beta}k_\delta\hat{\sigma}^{(0)*}_{\beta\delta}(\mathbf{k})\right] \\ & + \frac{\lambda V}{2}\left(\bar{\epsilon}_{\alpha\alpha} - \hat{\epsilon}^{(0)}_{\alpha\alpha}(\mathbf{k}=0)\right)^2 \\ & + \mu V\left(\bar{\epsilon}_{\alpha\beta} - \hat{\epsilon}^{(0)}_{\alpha\beta}(\mathbf{k}=0)\right)^2, \end{aligned} \tag{A26}$$

which differs from case (i) only by the homogeneous contribution. Obviously, the earlier case follows from the average strain relaxation with $\hat{\epsilon}^{(0)}_{\alpha\beta}(\mathbf{k}=0) = \bar{\epsilon}_{\alpha\beta}$, in agreement with the conditions (A11) and (A12).

[1] A. Karma and W. J. Rappel, Phase-field method for computationally efficient modeling of solidification with arbitrary interface kinetics, Phys. Rev. E **53**, R3017(R) (1996).

[2] K. Wang, G. Boussinot, C. Hüter, E. A. Brener, and R. Spatschek, Modeling of dendritic growth using a quantitative nondiagonal phase field model, Phys. Rev. Mater. **4**, 033802 (2020).

[3] A. Finel, Y. Le Bouar, B. Dabas, B. Appolaire, Y. Yamada, and T. Mohri, Sharp phase field method, Phys. Rev. Lett. **121**, 025501 (2018).

[4] L.-Q. Chen, Phase-field models for microstructure evolution, Annu. Rev. Mater. Res. **32**, 113 (2002).

[5] R. Sandt, Y. Le Bouar, and R. Spatschek, Quantum annealing for microstructure equilibration with long-range elastic interactions, Sci. Rep. **13**, 6036 (2023).

[6] L. C. P. dos Santos, T. Hang, R. Sandt, M. Finsterbusch, Y. Le Bouar, and R. Spatschek, Elastic energy driven multivariant selection in martensites via quantum annealing, Phys. Rev. Res. **6**, 023076 (2024).

[7] A. B. Finnila, M. A. Gomez, C. Sebenik, C. Stenson, and J. D. Doll, Quantum annealing: A new method for minimizing multidimensional functions, Chem. Phys. Lett. **219**, 343 (1994).

[8] J. Brooke, D. Bitko, T. F. Rosenbaum, and G. Aeppli, Quantum annealing of a disordered magnet, Science **284**, 779 (1999).

[9] T. Kadowaki and H. Nishimori, Quantum annealing in the transverse Ising model, Phys. Rev. E **58**, 5355 (1998).

[10] S. Morita and H. Nishimori, Mathematical foundation of quantum annealing, J. Math. Phys. **49**, 125210 (2008).

[11] A. Rajak, S. Suzuki, A. Dutta, and B. K. Chakrabarti, Quantum annealing: An overview, Phil. Trans. R. Soc. A. **381**, 20210417 (2023).

[12] R. H. Warren, Mathematical methods for a quantum annealing computer, J. Adv. Appl. Math. **3**, 82 (2018).

[13] M. W. Johnson, M. H. Amin, S. Gildert, T. Lanting, F. Hamze, N. Dickson, R. Harris, A. J. Berkley, J. Johansson, P. Bunyk, E. M. Chapple, C. Enderud, J. P. Hilton, K. Karimi, E. Ladizinsky, N. Ladizinsky, T. Oh, I. Perminov, C. Rich, M. C. Thom, E. Tolkacheva, C. J. S. Truncik, S. Uchaikin, J. Wang, B. Wilson, and G. Rose, Quantum annealing with manufactured spins, Nature (London) **473**, 194 (2011).

[14] S. Boixo, T. F. Rønnow, S. V. Isakov, Z. Wang, D. Wecker, D. A. Lidar, J. M. Martinis, and M. Troyer, Evidence for quantum annealing with more than one hundred qubits, Nat. Phys. **10**, 218 (2014).

[15] R. Sandt and R. Spatschek, Efficient low temperature Monte Carlo sampling using quantum annealing, Sci. Rep. **13**, 6754 (2023).

[16] B. Camino, J. Buckeridge, P. A. Warburton, V. Kendon, and S. M. Woodley, Quantum computing and materials science: A practical guide to applying quantum annealing to the configurational analysis of materials, J. Appl. Phys. **133**, 221102 (2023).

[17] R. Harris, Y. Sato, A. J. Berkley, M. Reis, F. Altomare, M. H. Amin, K. Boothby, P. Bunyk, C. Deng, C. Enderud, S. Huang, E. Hoskinson, M. W. Johnson, E. Ladizinsky, N. Ladizinsky, T. Lanting, R. Li, T. Medina, R. Molavi, R. Neufeld, T. Oh, I. Pavlov, I. Perminov, G. Poulin-Lamarre, C. Rich, A. Smirnov, L. Swenson, N. Tsai, M. Volkmann, J. Whittaker, and J. Yao, Phase transitions in a programmable quantum spin glass simulator, Science **361**, 162 (2018).

[18] P. Kairys, A. D. King, I. Ozfidan, K. Boothby, J. Raymond, A. Banerjee, and T. S. Humble, Simulating the Shastry-Sutherland Ising model using quantum annealing, PRX Quant. **1**, 020320 (2020).

[19] K. Kitai, J. Guo, S. Ju, S. Tanaka, K. Tsuda, J. Shiomi, and R. Tamura, Designing metamaterials with quantum annealing and factorization machines, Phys. Rev. Res. **2**, 013319 (2020).

[20] J. Nelson, M. Vuffray, A. Y. Lokhov, T. Albash, and C. Coffrin, High-quality thermal gibbs sampling with quantum annealing hardware, Phys. Rev. Appl. **17**, 044046 (2022).

[21] M. Vuffray, C. Coffrin, Y. A. Kharkov, and A. Y. Lokhov, Programmable quantum annealers as noisy gibbs samplers, PRX Quant. **3**, 020317 (2022).

[22] S. Mandrà, Z. Zhu, and H. G. Katzgraber, Exponentially biased ground-state sampling of quantum annealing machines with transverse-field driving Hamiltonians, Phys. Rev. Lett. **118**, 070502 (2017).

[23] M. S. Könz, G. Mazzola, A. J. Ochoa, H. G. Katzgraber, and M. Troyer, Uncertain fate of fair sampling in quantum annealing, Phys. Rev. A **100**, 030303(R) (2019).

[24] S. Mukherjee and B. K. Chakrabarti, On the question of ergodicity in quantum spin glass phase and its role in quantum annealing, J. Phys. Soc. Jpn. **88**, 061004 (2019).

[25] M. Yamamoto, M. Ohzeki, and K. Tanaka, Fair sampling by simulated annealing on quantum annealer, J. Phys. Soc. Jpn. **89**, 025002 (2020).

[26] M. Jünger, E. Lobe, P. Mutzel, G. Reinelt, F. Rendl, G. Rinaldi, and T. Stollenwerk, Quantum annealing versus digital computing: An experimental comparison, ACM J. Exp. Algorithm. **26**, 1 (2021).

[27] O. Parekh, J. Wendt, L. Shulenburger, A. Landahl, J. Moussa, and J. Aidun, Benchmarking adiabatic quantum optimization for complex network analysis, https://www.osti.gov/biblio/1459086 (2015).

[28] B. Yan and N. A. Sinitsyn, Analytical solution for nonadiabatic quantum annealing to arbitrary Ising spin Hamiltonian, Nat. Commun. **13**, 2212 (2022).

[29] A. D. King, J. Raymond, T. Lanting, R. Harris, A. Zucca, F. Altomare, A. J. Berkley, K. Boothby, S. Ejtemaee, C. Enderud, E. Hoskinson, S. Huang, E. Ladizinsky, A. J. R. MacDonald, G. Marsden, R. Molavi, T. Oh, G. Poulin-Lamarre, M. Reis, C. Rich, Y. Sato, N. Tsai, M. Volkmann, J. D. Whittaker, J. Yao, A. W. Sandvik, and M. H. Amin, Quantum critical dynamics in a 5, 000-qubit programmable spin glass, Nature (London) **617**, 61 (2023).

[30] R. Y. Li, R. Di Felice, R. Rohs, and D. A. Lidar, Quantum annealing versus classical machine learning applied to a simplified computational biology problem, npj Quantum Inf. **4**, 14 (2018).

[31] A. Perdomo-Ortiz, N. Dickson, M. Drew-Brook, G. Rose, and A. Aspuru-Guzik, Finding low-energy conformations of lattice protein models by quantum annealing, Sci. Rep. **2**, 571 (2012).

[32] A. Irbäck, L. Knuthson, S. Mohanty, and C. Peterson, Folding lattice proteins with quantum annealing, Phys. Rev. Res. **4**, 043013 (2022).

[33] E. Boyda, S. Basu, S. Ganguly, A. Michaelis, S. Mukhopadhyay, and R. R. Nemani, Deploying a quantum annealing processor to detect tree cover in aerial imagery of California, PLoS ONE **12**, e0172505 (2017).

[34] F. Neukart, G. Compostella, C. Seidel, D. von Dollen, S. Yarkoni, and B. Parney, Traffic flow optimization using a quantum annealer, Front. ICT **4**, 29 (2017).

[35] M. Ohzeki, A. Miki, M. J. Miyama, and M. Terabe, Control of automated guided vehicles without collision by qantum annealer and digital devices, Front. Comput. Sci. **1**, 9 (2019).

[36] L. Mañosa and A. Planes, Mechanocaloric effects in shape memory alloys, Phil. Trans. R. Soc. A. **374**, 20150310 (2016).

[37] K. Otsuka and X. Ren, Physical metallurgy of Ti–Ni-based shape memory alloys, Prog. Mater. Sci. **50**, 511 (2005).

[38] D. Sherrington, A simple spin glass perspective on martensitic shape-memory alloys, J. Phys.: Condens. Matter **20**, 304213 (2008).

[39] S. Kartha, T. Castán, J. A. Krumhansl, and J. P. Sethna, Spin-Glass nature of tweed precursors in martensitic transformations, Phys. Rev. Lett. **67**, 3630 (1991).

[40] J. P. Sethna, S. Kartha, T. Castán, and J. A. Krumhansl, Tweed in Martensites: A potential new spin glass, Phys. Scr. **T42**, 214 (1992).

[41] R. Vasseur and T. Lookman, Spin models for ferroelastics: Towards a spin glass description of strain glass, Solid State Phenom. **172-174**, 1078 (2011).

[42] C. A. Geiger, E. Alekseev, B. Lazic, M. Fisch, T. Armbruster, R. Langner, M. Fechtelkord, N. Kim, T. Pettke, and W. Weppner, Crystal chemistry and stability of "$Li_7La_3Zr_2O_{12}$" garnet: A fast lithium-ion conductor, Inorg. Chem. **50**, 1089 (2011).

[43] E. Enkhbayar and J. H. Kim, Study of codoping effects of Ta^{5+} and Ga^{3+} on Garnet $Li_7La_3Zr_2O_{12}$, ACS Omega **7**, 47265 (2022).

[44] L. J. Miara, S. P. Ong, Y. Mo, W. D. Richards, Y. Park, J.-M. Lee, H. S. Lee, and G. Ceder, Effect of Rb and Ta doping on the ionic conductivity and stability of the garnet Li_{7+2x-y} $(La_{3-x}Rb_x)$ $(Zr_{2-y}Ta_y)$ O_{12} $(0 \leqslant x \leqslant 0.375, 0 \leqslant y \leqslant 1)$ Superionic Conductor: A first principles investigation, Chem. Mater. **25**, 3048 (2013).

[45] H. Buschmann, J. Dölle, S. Berendts, A. Kuhn, P. Bottke, M. Wilkening, P. Heitjans, A. Senyshyn, H. Ehrenberg, A. Lotnyk, V. Duppel, L. Kienle, and J. Janek, Structure and dynamics of the fast lithium ion conductor $Li_7La_3Zr_2O_{12}$, Phys. Chem. Chem. Phys. **13**, 19378 (2011).

[46] S. Yu, R. D. Schmidt, R. Garcia-Mendez, E. Herbert, N. J. Dudney, J. B. Wolfenstine, J. Sakamoto, and D. J. Siegel, Elastic properties of the solid electrolyte $Li_7La_3Zr_2O_{12}$ (LLZO), Chem. Mater. **28**, 197 (2016).

[47] J. F. Nonemacher, C. Hüter, H. Zheng, J. Malzbender, M. Krüger, R. Spatschek, and M. Finsterbusch, Microstructure and properties investigation of garnet structured $Li_7La_3Zr_2O_{12}$ as electrolyte for all-solid-state batteries, Solid State Ion. **321**, 126 (2018).

[48] R. Sandt, Y. Wang, and R. Spatschek, Investigation of mechanical properties of garnet structured $Li_7La_3Zr_2O_{12}$ under Al^{3+} and Ta^{5+} co-substitutions, Solid State Ion. **402**, 116364 (2023).

[49] W. C. Johnson and P. W. Voorhees, Elastic interactions and stability of misfitting cuboidal inhomogeneities, J. Appl. Phys. **61**, 1610 (1987).

[50] C. H. Rycroft, VORO++: A three-dimensional Voronoi cell library in C++, Chaos **19**, 041111 (2009).

[51] F. Aurenhammer, Voronoi diagrams—A survey of a fundamental geometric data structure, ACM Comput. Surv. **23**, 345 (1991).

[52] J. Raymond, R. Stevanovic, W. Bernoudy, K. Boothby, C. C. McGeoch, A. J. Berkley, P. Farré, J. Pasvolsky, and A. D. King, Hybrid quantum annealing for larger-than-QPU lattice-structured problems, ACM Trans. Quantum Comput. **4**, 1 (2023).

[53] V. Choi, Minor-embedding in adiabatic quantum computation: II. Minor-universal graph design, Quant. Inf. Process. **10**, 343 (2011).

[54] J. J. Berwald, The mathematics of quantum-enabled applications on the D-Wave quantum computer, Not. Am. Math. Soc. **66**, 832 (2019).

[55] D-Wave Leap quantum cloud service, https://cloud.dwavesys.com.

[56] H.-C. Yu, D. Taha, T. Thompson, N. J. Taylor, A. Drews, J. Sakamoto, and K. Thornton, Deformation and stresses in solid-state composite battery cathodes, J. Power Sources **440**, 227116 (2019).

[57] https://www.fz-juelich.de/ias/jsc.

[58] M. Frigo and S. G. Johnson, The design and implementation of FFTW3, Proc. IEEE **93**, 216 (2005).

[59] A. G. Khachaturyan, *Theory of Structural Transformations in Solids* (Dover Publications, Mineola, NY, 2008).

scientific reports

Check for updates

OPEN

Efficient low temperature Monte Carlo sampling using quantum annealing

Roland Sandt[1]✉ & Robert Spatschek[1,2]

Quantum annealing is an efficient technology to determine ground state configurations of discrete binary optimization problems, described through Ising Hamiltonians. Here we show that—at very low computational cost—finite temperature properties can be calculated. The approach is most efficient at low temperatures, where conventional approaches like Metropolis Monte Carlo sampling suffer from high rejection rates and therefore large statistical noise. To demonstrate the general approach, we apply it to spin glasses and Ising chains.

The recent advent of quantum annealing (QA) is an important step towards the development of quantum computing in the future, which will significantly boost also statistical physics and materials science modeling. In general, QA, as implemented by the company D-Wave, allows to find efficiently ground state configurations of discrete optimization problems, with many possible applications in academia and industry[1–5]. There are many problem types to which QA has been applied, like the demonstration of scaling or algorithmic advantages for QA in specific problem classes[6–8]. So far, applications of QA in the field of materials science are still rare, and among them are the determination of equilibrium microstructures with long-range elastic interactions[9], phase transitions in the transverse field Ising model[10], the investigation of energy states of frustrated magnetic systems via the Shastry-Sutherland model[11] and the designing of metamaterials[12]. Another example is the combined use of quantum annealers and Boltzmann machines to sample spin glasses and to predict molecular dynamics data of a MoS_2 layer[13].

The concept of QA is to initialize the system's Hamiltonian at cryogenic temperatures in a well defined ground state, and then to smoothly convert the energy landscape such that it represents the desired optimization problem[14,15]. If this adiabatic transformation is performed carefully, the system ends up in the ground state of the destination Hamiltonian. An explicit finite temperature modeling of this transition has been performed for the Sherrington-Kirkpatrick spin glass model, see[16,17] and references therein. However, apart from the stochastic nature of the approach itself, the preparation, transformation and readout process are not perfectly adiabatic, noise-free and decoupled from the environment, hence frequently states with higher energy are found, especially for Hamiltonians with small energy gaps. For a typical QA experiment, multiple repetitions and reads are used to determine the true ground state. In this paper we demonstrate that this deficit of the technology can actually be turned into a virtue, as it allows to determine finite temperature thermodynamic properties extremely efficiently. Related to that, the concept of using QA as (noisy) Gibbs sampler has been discussed recently[18,19], but it turns out that a tuning of the temperature for performing quantitative simulations is challenging. Moreover, it has been shown that at least for some machine architectures degenerate ground states are sampled unequally with an exponential bias, contrary to the thermodynamic equilibrium concept that equal energy states should be visited with the same probability in the canonical ensemble, therefore demanding special attention[20–24].

From a materials science perspective, the ground state configuration at temperature $T = 0$ K is often only of limited interest for many practical applications. For example, for a ferromagnet, all spins are aligned in the ground state, whereas for finite temperatures thermal fluctuations lead to finite correlation lengths, phase transitions and temperature dependent magnetizations. A conventional approach for a statistical modeling of such properties is to use Monte Carlo (MC) sampling techniques, as an explicit computation of the partition function is typically not feasible due to the vast size of the phase space. The probably most prominent approach for such computations is the generation of discrete Markov chains using Metropolis transition probabilities, which generate a sequence of configurations which obey Boltzmann statistics, and therefore allow to express the ensemble average through the easier calculation of time averages along these Markov chains[25,26]. In practise, a transition from one state to another is taking place with probabilities depending on the energy difference ΔE between two configurations according to a Boltzmann distribution $p \sim \exp(-\beta \Delta E)$ with $\beta = 1/kT$ with the Boltzmann constant k. Usually,

[1]Structure and Function of Materials, Institute of Energy and Climate Research, Forschungszentrum Jülich GmbH, 52425 Jülich, Germany. [2]JARA-ENERGY, 52425 Jülich, Germany. ✉email: r.sandt@fz-juelich.de

such approaches are inefficient at low temperatures, as then the rejection rate for new configurations is very high, and hence an insufficient sampling of the phase space is achieved with trapping in local minima, resulting in noisy predictions of the desired thermodynamic properties. Another important sampling strategy was developed by Wang and Landau, using a non-Markovian algorithm to extract the density of states via a flat histogram technique, from which all desired thermodynamic properties can be calculated[27]. Besides these major techniques, Dall et al. developed an algorithm to sample the Boltzmann distribution fast at low temperatures. However, this algorithm is most suitable for systems with short range interactions[28]. Another possibility for the fair sampling of ground and degenerate states is the introduction of parallel tempering with isoenergetic cluster updates in Monte Carlo methods[29] or the combination with simulated annealing on a quantum annealer[30,31]. We mention that Boltzmann machines, which can serve as a link between machine learning and statistical thermodynamics[32], are investigated in the context of QA[33–36] from a computer science perspective, but to the best of our knowledge, the direct application of QA for classical finite temperature modeling for statistical physics and materials science has not yet been accomplished and is the subject of the present paper.

Results

Spin glass. The key feature of the quantum annealer is that it finds preferentially configurations which are close to the global energy minimum of the phase space. As a first illustration how to determine the low temperature thermodynamics from these configurations, we use a spin glass[37,38] with random couplings, which is given by the Hamiltonian

$$H = \sum_{i<j} J_{ij} s_i s_j + \sum_i h_i s_i \tag{1}$$

with $N = 20$ spins $s_i = \pm 1$ and random values for the coupling constants, $J_{ij}, h_i \in [-J_{\max}, J_{\max}]$, $J_{\max} = 1/2$. As the matrix J_{ij} is fully populated, the model also includes long-range interactions. We point out that due to the random couplings, the energy landscape of the spin glass contains many states with nearby energy values without degeneracy, which avoids the issue of potentially unfair sampling of isoenergetic states. An example from materials science for such a spin glass are misfitting coherent grains in a polycrystalline solid, where the coupling constants result from elastic long-range interactions and external forces[9]. We repeat the quantum annealing read out process 10,000 times to get an estimate of the distribution of identified states, as due to the above mentioned reasons also higher energy states are found in practise. Therefore, we obtain a (sub-)set of states $S = \{x_i\}$, and each configuration consists of the value of spin variables, $x_i = (s_1^{(i)}, \ldots, s_N^{(i)})$, for which the resulting probability distribution is illustrated in the inset of Fig. 1a.

The distribution of the states depends to good approximation only on the energy of the individual configurations and follows (roughly) a Boltzmann distribution (with different effective temperatures), as has been discussed in the literature[18,19], although it should be noted that quantum fluctuations can lead to deviations from the purely thermal probability distribution[39]. For the following steps it is important to mention that the explicit form of the distribution is not critical, and we only exploit the fact that states with low energies are found preferentially.

Additionally, a rescaling of the Hamiltonian $H \to aH$ by a factor $0 < a < 1$ allows to sample regions of the phase space with higher energy (see inset in Fig. 1a), requiring to switch off the automatic rescaling of the coupling constants by the D-Wave framework. The smaller a is chosen, the more high energy configurations are sampled. Explicitly, for the $N = 20$ spin glass with a configuration space of size $2^N \approx 10^6$, we use 10,000 reads,

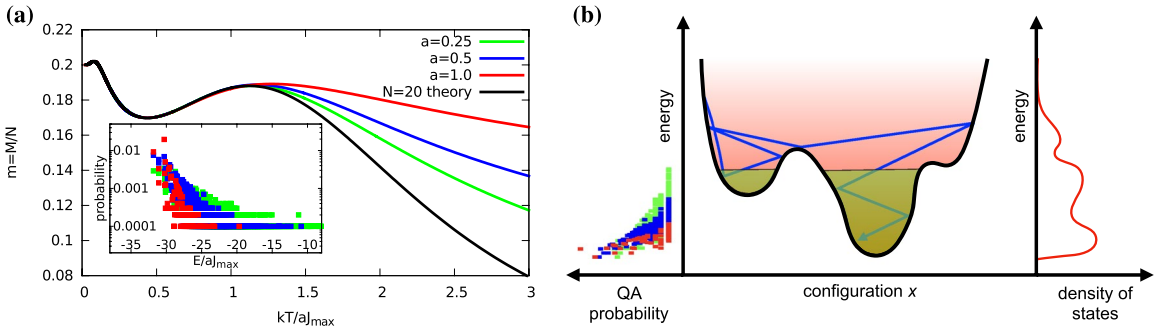

Figure 1. Mean magnetization and probability distribution of a spin glas and sampling strategy. (**a**) The plot shows the temperature dependent magnetization of an $N = 20$ random coupling spin glass. The QA sampled values coincide with the theoretical results in the low temperature regime, whereas for elevated temperatures the energy rescaling factor a affects the quality of the results. The probability for getting a state x, which is estimated using 10,000 repetitions of the sampling, depends to good approximation only on its energy $E(x)$ and follows essentially a Boltzmann distribution, as shown as inset. Different rescaling factors $a > 0$ shift the distributions to higher or lower energies. (**b**) Illustration of the different sampling strategies. The blue trajectory illustrates the Markov chain generated by the Metropolis algorithm to generate a Boltzmann probability distribution (red shading). Alternatively, the Wang-Landau approach constructs the density of states, from which thermodynamic properties can be predicted. In contrast, the QA approach identifies low energy configurations (green shading), which are taken as most representative fraction of the phase space for low temperature expectation values.

which lead to around 300 (for $a = 1.0$) to 5,000 (for $a = 0.25$) distinct configurations in the subset S (the actual numbers fluctuate due to the non-deterministic behavior). We note that the concept of the rescaling of coupling constants has been previously used to effectively change the temperature of the distribution generated by the quantum annealer[18,19], which is however not required here.

To obtain a numerical estimate of the canonical partition function using QA, we take the identified distinct low energy configuration set S and use the approximated canonical partition function

$$Z_a = \sum_{x \in S} \exp(-\beta H(x)), \tag{2}$$

which obviously becomes more accurate for a better sampling of the low energy configurations. Notice that the desired (and given) inverse temperature β is typically not related to the effective one related to the probability distributions of the QA sampling. With the estimated Boltzmann probability $p_a(x) = \exp(-\beta H(x))/Z_a$ of a state x we can obtain estimated expectation values of an observable $A(x)$ according to

$$\langle A \rangle = \sum_{x \in S} p_a(x) A(x). \tag{3}$$

We emphasize that the set S is significantly smaller than the size 2^N of the phase space, and therefore estimated values can be calculated efficiently also for large values of N, for which a direct computation of the partition function is no longer feasible. Furthermore, the same set is used for all temperatures, and therefore it is not necessary to create new chains of configurations like for Metropolis sampling. In this sense, the proposed algorithm is comparable to multicanonical approaches employing Wang-Landau sampling. As S contains mainly the low energy configurations, we expect that the estimated expectation values get accurate for low temperatures, i.e. large values of the inverse temperature $\beta = 1/kT$.

This expectation is confirmed in Fig. 1a for the magnetization per spin, $m = M/N = N^{-1}\langle \sum_{i=1}^{N} s_i \rangle$. The results show that irrespective of the choice of the rescaling parameter a, the low temperature magnetization always coincides with the theoretical expectation, which is obtained from a brute force sampling of the partition function. Hence, a is here not used as a method to tune the effective temperature, as compared to the approaches mentioned above[18,19]. As discussed above, a smaller value of a leads to sampling of more excited states, and consequently the better the agreement with the theoretical prediction also for higher temperatures. We emphasize that a single value of the parameter a is sufficient to determine the low temperature behavior accurately, and the dependence on the choice of this parameter is weak, which is beneficial for applications, as no careful tuning of this degree of freedom is required.

In essence, we can consider the (imperfect) quantum annealing process as a way to find a representative set of states in the phase space which contribute strongest to the partition function from statistical mechanics due to their high Boltzmann weight. These selected configurations are used to estimate thermodynamic properties. This strategy, compared to conventional Boltzmann sampling approaches, is illustrated in Fig. 1b. The simple and robust concept is to identify potentially relevant low energy states, with no weighting according to the probability of appearance during the readout process. Instead, the proper Boltzmann weighting is then done in the approximated calculation of expectation values and the partition function, using directly the desired temperature.

1D Ising model. To investigate the performance of the approach also for larger systems, we consider the 1D Ising model, as in this case an analytical solution is known and allows also for comparisons in situations, where a brute force sampling of the phase space is no longer feasible. Moreover, the example differs from the previous one by having a sparse interaction matrix J_{ij} and the existence of degenerate states. Therefore, these two cases cover a wide range of typical situations.

Explicitly, we use a one-dimensional Ising model with nearest neighbor ferromagnetic coupling to illustrate the calculation of thermodynamic properties using the set of states S sampled in analogy to the demonstration above. The model is described by the Hamiltonian ($J < 0$)

$$H = J \sum_{k=1}^{N} s_k s_{k+1} + B \sum_{k=1}^{N} s_k \tag{4}$$

with periodic boundary conditions ($s_{N+1} = s_1$), and has a simple analytical solution also for finite values of N, which serves as benchmark for the procedure. In fact, the canonical partition function is[40]

$$Z = \sum_{\text{states}} \exp(-\beta H) = \lambda_+^N + \lambda_-^N \tag{5}$$

with the eigenvalues

$$\lambda_\pm = \exp(-\beta J)\left[\cosh(\beta B) \pm \sqrt{\sinh^2(\beta B) + \exp(4\beta J)}\right], \tag{6}$$

from which e.g. the Helmholtz free energy $F = -kT \ln Z$ and the magnetization per spin $m = M/N = (\partial F/\partial B)/N$ can be calculated.

Again, the comparison between the exact solution and the QA sampling shows an excellent agreement of the magnetization for low temperatures, as shown in Fig. 2 for $N = 20$ and $N = 50$ spin systems.

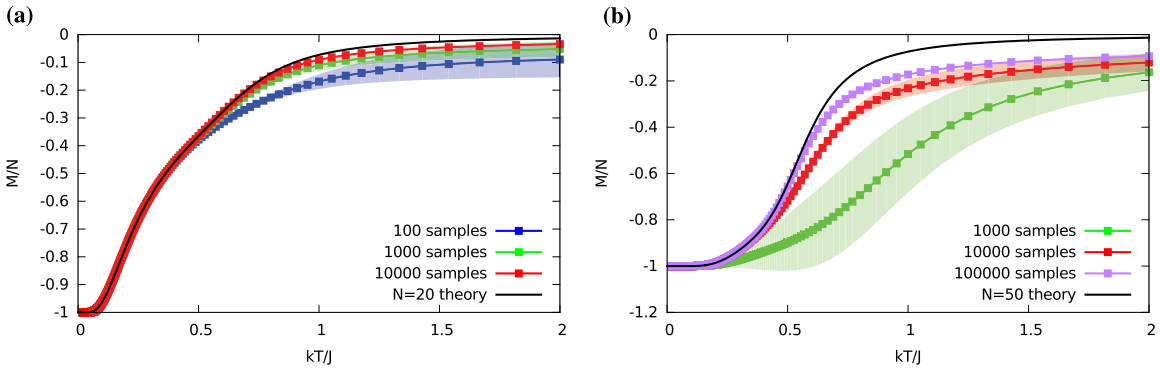

Figure 2. Magnetization of the 1D Ising model with periodic boundary conditions. The graphs show the magnetization per spin as function of temperature for (**a**) $N = 20$ and (**b**) $N = 50$ spin systems, comparing the exact analytical solution with the results from the quantum annealer. In the low temperature regime there is a perfect match, which becomes worse for higher values of kT/J. In the high temperature limit, where we expect the average magnetization to vanish, the annealer prediction saturates at finite values, as high energy states are not sampled properly. An increase of the number of annealing cycles leads to more accurate predictions, which is further enhanced by spin flip reversals. The parameters for coupling constants are $B/J = 0.01$. Ten spin reversal transformations are considered for each sampling, while for 100, 000 samples in the $N = 50$ system 1, 000 spin flip transformations are used. The shading illustrates the error bars of the calculations, as estimated from repeated simulations (see "Methods" section).

For low temperatures the quantum annealing sampling is indeed in perfect agreement with the exact solution, already even for a low number of sampled configurations, which are typically generated anyway for QA applications. For higher temperatures deviations are visible, and the estimated magnetization saturates at unphysical finite values. This is an expected result, as for high temperatures all states contribute to the partition function, and then the pre-selection advantage by the QA is lost. The deviations decrease with increasing number of samples and increase with higher numbers of spins.

It is known that slight asymmetries in the quantum annealer can lead to favoring of specific spin alignments, and therefore spin reversal transformations, which change signs of the coupling constants without changing the physical results (see "Methods" section), can be beneficial[41]. We indeed observe a better agreement with the theoretical prediction if this feature is used. Figure 3a shows the influence of different number of spin reversal transforms on resulting magnetization and computational demand.

An increasing number of transforms lead to better results, compared to the exact analytical solution at the expense of an increase of the needed annealing time. However, quantum annealing sampling needs only a fraction of time compared to other algorithms, and therefore this increase will not be critical for many applications.

An additional analysis of the magnetic field term of the Ising Hamiltonian in Fig. 3b shows the expected alignment of spins for varying external magnetic field B. All curves show the expected low temperature agreement with theory, depicted as dotted lines. Surprisingly, for low magnetic fields, where the asymmetry between

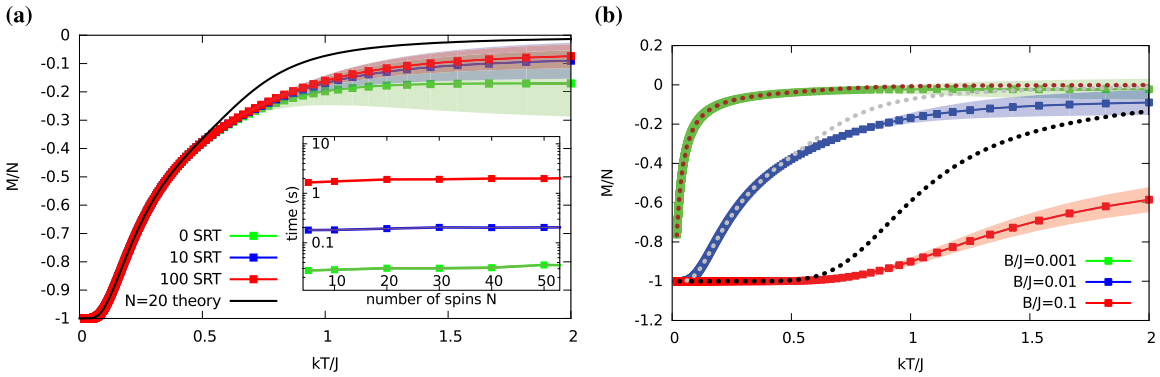

Figure 3. Influence of different number of spin-reversal gauge transforms and varying magnetic fields. (**a**) Different amounts of spin-reversal transformations (SRT) during the annealing change the sampling outcomes. For QA of the N=20 spin system with $B/J = 0.01$ and altogether 100 samples no, 10 and 100 SRT are used. A higher fraction of spin flips leads to more accurate predictions of the magnetization, as compared to the analytical solution (black curve). The inset shows the increasing computational demand of additional SRT. On the vertical axis, the measured QPU access time including corresponding overhead is shown as function of the number of spins in a logarithmic representation. (**b**) Magnetization as function of temperature for different external magnetic fields B. The dotted lines show the exact analytical solution for the corresponding magnetic fields.

spin up and down configurations is lower, and where usually thermodynamic sampling is most difficult, the best agreement between simulation and theoretical prediction is reached even for elevated temperatures.

The D-Wave frontend Leap also provides functionality to influence the transformation from the transverse to the desired Hamiltonian. Usually, the associated parameters can be used to obtain the true ground state in a more reliable way. In this spirit, also reverse annealing[42] is useful for a successful ground state search and consequently to suppress the appearance of excited states. In general, a pause in the annealing process leads to a interruption of the quantum fluctuations induced by the transverse field and allows for thermal relaxations[43]. Here, we have checked whether these features can also be used to achieve the opposite goal of the usual improved global minimization, namely a better sampling of low energy states above the ground state. It turns out that a pause in the annealing procedure has only minor influence on the expectation value of the magnetization, whereas quenching improves the chance of finding low energy states. Therefore, we have modified the annealing schedule up to the maximum possible duration of 2000 µs, including a quench step. With such a customized annealing schedule, a better prediction of the magnetization at low temperatures is found already for just 100 samples in an $N = 50$ spin system, compared to the standard schedule. Therefore, a change of the annealing protocol can lead to additional improvements for the thermodynamic predictions, although typically the effect is less pronounced than the use of the spin reversal transformations mentioned above, and therefore the standard 20 µs annealing schedule is used for all shown plots.

We compare the preceding QA results to conventional MC sampling using the Metropolis algorithm (see "Methods" section). For each temperature, a separate Markov chain is generated for the sampling. The comparison of both approaches is shown in Fig. 4 for the magnetization m and the heat capacity per spin, $c = k\beta^2(\langle H^2\rangle - \langle H\rangle^2)/N$.The generic and frequently used Metropolis MC approach suffers from low acceptance rates for proposed configurations at low temperatures, and therefore an accurate sampling in this regime is difficult. Exactly in this low temperature regime the quantum annealer approach plays its strength as it accesses directly the low energy configurations, which give the highest contribution to the partition function. The same set of generated configurations is used for all temperatures, like for multicanonical sampling techniques. We note that for the Monte Carlo sampling typically many more samples are necessary than for QA to get comparable results in the low temperature regime, and this number increases significantly for larger spin systems. Due to the focus on the QA approach, we refrain from further MC code optimization, Wang-Landau sampling and a comparison to other algorithms, which can perform well also for low temperatures. The presently suggested approach can become most relevant in situations, where QA is anyway used for identifying ground state configurations, as then at almost no additional computational cost also thermodynamic properties can be obtained. Altogether, we find that the different approaches complement each other very well, in particular since the QA approach is most suitable in the low temperature regime.

Discussion

Quantum annealing is an efficient approach to determine global minima of complex energy landscapes, which are described by Ising Hamiltonians or, equivalently, quadratic unconstrained binary optimization (QUBO) problems. Due to machine imperfections and the stochastic nature of quantum annealing, typically several repetitions of the annealing process have to be performed, in order to find reliably the true ground state(s). Whereas for many applications the excited, higher energy states are ignored in the end, we have demonstrated here that they can be used for an efficient Monte Carlo Boltzmann sampling to obtain thermodynamic properties above absolute zero. These additional results are obtained essentially for free or at low computational cost, since in

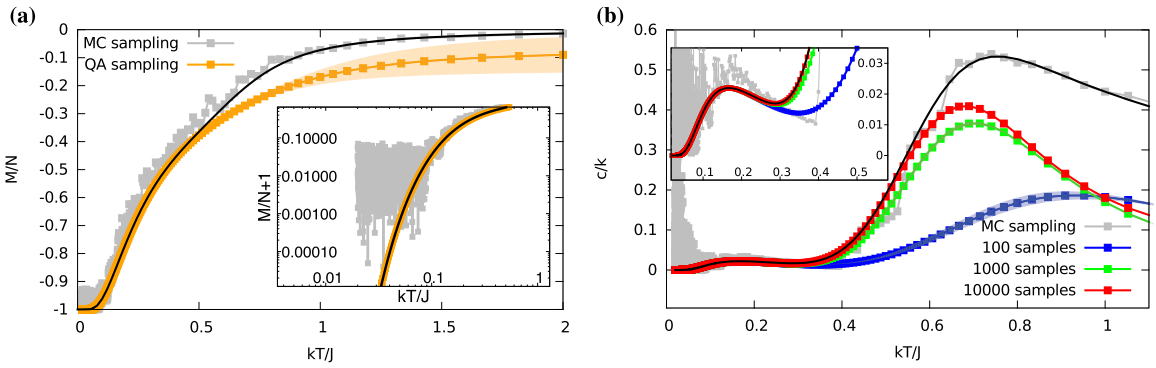

Figure 4. Comparison to Metropolis Monte Carlo sampling. (**a**) Comparison of the analytical theory, Metropolis Monte Carlo sampling and quantum annealing sampling for the 1D Ising model with $N = 20$ spins and $B/J = 0.01$. Whereas the Metropolis algorithm performs well in the high temperature regime, the results get noisy for low temperatures due to the high rejection rate of proposed states. Notice that the used 10^8 random trial configurations correspond to more than the 2^N configurations of the phase space, while only 100 samples with 10 spin flip transformations are necessary for the quantum annealing sampling. The exact analytical solution is depicted as black solid line. The inset shows the magnification of the low temperature regime using a logarithmic representation of $M/N + 1$. (**b**) Heat capacity per spin for the same parameter set as in panel (**a**). The plot compares the analytical solution (black curve) to the Metropolis MC sampling (grey curve) and QA predictions for different number of reads. The inset shows the magnification of the low temperature regime.

the low temperature regime often only very few configurations with energies slightly above the ground state are required to predict the low temperature thermodynamics.

The shown simulations do not exhibit artifacts which could indicate an improper sampling of energetically equivalent states, although such configurations exist in particular in the considered Ising model already due to translation invariance. In principle, e.g. an exponential bias of degenerate ground or low energy state configurations[20] could be expected to lead to inappropriate low temperature predictions, but the current results do not show such discrepancies. We believe that the robustness of the approach relies on the fact that it is sufficient to identify each low energy configuration x once to be included into the set S, and therefore unfair sampling artifacts are screened if the number of reads is high enough. It is conceivable that for larger system sizes N such effects become more pronounced, and we observe that for sizes $N \approx 80$ on the used machine (Advantage system 4.1 with Pegasus topology) indeed more reads are required to obtain reliable results, and then the required computing time increases significantly. A good indication for such a need of more reads is that the identified low energy states have only a low number of realizations, as then the chances for missing relevant states is increased. In general, we note that the considered examples are not adjusted to the machine topology, and we therefore do not expect a strong machine type dependence of the prediction quality.

Let us briefly discuss limitations of the proposed sampling approach: First, the system sizes, which can be considered with QA, are currently limited due to the available machine sizes. However, the development of quantum annealing is still at its beginning and progressing fast, hence it can be expected that in the future faster and highly connected machines, especially with a higher number of accessible qubits, will be available, which will allow to study also models in higher dimensions with first and second order phase transitions also at finite temperatures. In the meantime, also the use of hybrid approaches[44], which combine QA and classical minimization methods, may turn out to be useful also for finite temperature sampling. Such approaches are in general already provided by D-Wave, but they currently require manual repeated sampling due to the lower efficiency compared to pure QA. Also, overriding the automatic coupling constant renormalization is not possible, as the focus of the approach is to find most efficiently the true ground state. Nevertheless, the use of hybrid methods allows to study significantly larger system sizes than with pure QA[9].

The second limitation is that QA requires to express the problem in terms of an Ising or QUBO formulation. We emphasize that the 1D Ising model was mainly used here to have an exact solution for benchmarking the results. Nevertheless, the methodology is applicable also to other problems where thermal excitations can play a role, e.g. for (weak) coherency strains in microstructures with long range elastic interactions[9]. In general, the Ising or QUBO limitation can actually be less severe as it may appear. To illustrate this, let us consider a simple three state system, $k = 1, 2, 3$ with discrete states x_k and energy levels E_k. This case can be represented through the Ising Hamiltonian $H = \sum_{i<j}^{N} J_{ij} s_i s_j + \sum_{i}^{N} h_i s_i$ with $N = 2$ spins. The three parameters J_{12}, h_1 and h_2 can be uniquely determined via a linear system of equations from the given energy values E_k by identifying the states x_k with spin pair configurations (s_1, s_2). As the Ising model leads to 2^N configurations, there is one undesired state in this example, which can simply be omitted in the calculation of the thermodynamic properties. This way illustrates how the approach for obtaining low temperature data can be extended to general problems beyond the Ising or QUBO model.

Finally, it is not a priori clear up to which temperature the QA approach can deliver quantitative results. As demonstrated in this work, the use of more samples can improve the results, and a convergence study could be performed to extrapolate to the limit of infinite sample sizes. However, in practise such an approach will probably less useful, as it effectively leads to a sampling of the entire phase space, and then conventional approaches can be used more efficiently. Therefore, we believe that the QA sampling approach will be most useful to complement classical methods like Metropolis or Wang-Landau sampling, and will play its strengths in the low temperature limit at low computational overhead, where the other approaches are less suitable, in particular if anyway QA minimization is employed.

Methods

Quantum annealing. Like general purpose quantum computers, quantum annealers use qubits to process and store information, physically realized via superconducting loops, which represents different spin states via clockwise or anticlockwise circulating currents[45]. The interaction of these superconducting loops with external flux biases allows the construction of an energy landscape, where energy difference and barrier height are controlled via these fluxes[45]. At the start of the computation, the system is initialized in the ground state of a known Hamiltonian $H_0 \sim -\sum_i \sigma_i^x$ with Pauli matrices σ_i, i.e. a strong transverse magnetic field[46,47]. During the annealing process, the Hamiltonian is turned into the desired one based on an Ising model[48] $H_p = \sum_i h_i s_i + \sum_{i<j} J_{ij} s_i s_j$ with spin states $s_i = \pm 1$, bias h_i and couplings J_{ij} between spins s_i and s_j, for which an energetic minimum is sought, $\min_{\{s_i=\pm 1\}} H_p$.

The annealing process follows the time dependence[49] $H(s) = \frac{1}{2}A(s)H_0 + \frac{1}{2}B(s)H_p$ with normalized anneal parameter $s \in [0, 1]$ and annealing evolution functions $A(s)$ and $B(s)$. For $s = 0$, $A(0) \gg B(0)$, the initial, well known ground state is present, while for $s = 1$, $A(1) \ll B(1)$, the system is expressed through the desired problem Hamiltonian[43]. In a standard annealing schedule the annealing parameter increases linearly, where varying this curve via pauses and quenches leads to a freezing of the system at an intermediate point with excited energy states[50]. This allows the sampling of the quantum Boltzmann distribution and a comparison towards classical estimators shows performance advantages of the quantum annealer for increasing system sizes[50]. Also, reverse annealing is possible, where qubits are initialized in a classical state and local minima are then searched around this state[51].

The Hamiltonians H_0 and H_p do not commute[48], and the time of the initial Hamiltonian to adopt the low energy state is sufficiently large to ensure the validity of the adiabatic theorem of quantum mechanics[52], which

states that a system remains in its eigenstate, if changes occur adiabatically. Nevertheless, the machines are not perfect and do not always adopt the corresponding low energy state of the system. Therefore, also higher energy states are found, which differ from the ground state, especially if energetically close low energy states exist, a suitable number of repetitions is made and the annealing process is repeated according to a specified number of reads.

In our work the application of spin flip reversals is beneficial and improves the sampling further. This feature reflects that the machine is technically not absolutely invariant under an inversion of spins due to slight asymmetries. To overcome an artificial bias, the annealer can automatically transform the couplings according to $h_i \rightarrow h_i g_i$ and $J_{ij} \rightarrow J_{ij} g_i g_j$ with random gauges $g_i \in \{-1, +1\}$, which leave the physical problem invariant.

We use the D-Wave framework Leap[53], as it allows to directly formulate the problem in terms of an Ising Hamiltonian. The standard embedding composite *EmbeddingComposite*, which automatically minor-embeds[54] a problem into a sampler, is used in this work. Depending on the problem size, the given number of reads (samples) is distributed over several backend calls due to time limits of individual calls.

All quantum annealing calculations are repeated $n = 10$ times to determine the standard deviation $\sigma = \pm\sqrt{\frac{1}{n-1}\sum_{i=1}^{n}(x_i - \bar{x})^2}$, which is presented as shaded area in the plots. Here, n refers to the number of experiment repetitions, and for each of them, the given total number of reads is used.

Metropolis Monte Carlo. Starting point of the Metropolis Monte Carlo sampling is the generation of random spin configurations. In each iteration all spins are flipped and this new configuration is accepted, if the energy is lower than the previous one, i.e. $\Delta E < 0$. If the new energy is higher, the configuration is accepted with a probability given by the Boltzmann factor $\exp(-\Delta E/kT)$. For each configuration in particular the magnetization $M = \sum_{i=1}^{N} s_i$ is calculated and averaged along the generated trajectory. These calculations are repeated for each temperature.

Data availability

Data that was obtained during this project will be made available by the corresponding author upon request.

Received: 24 February 2023; Accepted: 19 April 2023
Published online: 25 April 2023

References

1. Irbäck, A., Knuthson, L., Mohanty, S. & Peterson, C. Folding lattice proteins with quantum annealing. *Phys. Rev. Res.* **4**, 043013. https://doi.org/10.1103/PhysRevResearch.4.043013 (2022).
2. Perdomo-Ortiz, A., Dickson, N., Drew-Brook, M., Rose, G. & Aspuru-Guzik, A. Finding low-energy conformations of lattice protein models by quantum annealing. *Sci. Rep.* **2**, 571. https://doi.org/10.1038/srep00571 (2012).
3. Boyda, E. *et al.* Deploying a quantum annealing processor to detect tree cover in aerial imagery of California. *PLoS One*https://doi.org/10.1371/journal.pone.0172505 *(2017)*.
4. Neukart, F. *et al.* Traffic flow optimization using a quantum annealer. *Front. ICT* **4**, 55. https://doi.org/10.3389/fict.2017.00029 (2017).
5. Ohzeki, M., Miki, A., Miyama, M. & Terabe, M. Control of automated guided vehicles without collision by qantum annealer and digital devices. *Front. Comput. Sci.*https://doi.org/10.3389/fcomp.2019.00009 *(2019)*.
6. Albash, T. & Lidar, D. Demonstration of a scaling advantage for a quantum annealer over simulated annealing. *Phys. Rev. X* **8**, 031016. https://doi.org/10.1103/PhysRevX.8.031016 (2018).
7. King, A. *et al.* Scaling advantage over path-integral Monte Carlo in quantum simulation of geometrically frustrated magnets. *Nat. Commun.* **12**, 1113. https://doi.org/10.1038/s41467-021-20901-5 (2021).
8. Tasseff, B. et al. On the emerging potential of quantum annealing hardware for combinatorial optimization. Preprint at https://doi.org/10.48550/arXiv.2210.04291 (2022).
9. Sandt, R., Le Bouar, Y. & Spatschek, R. Quantum annealing for microstructure equilibration with long-range elastic interactions. *Sci. Rep.* **13**, 6036. https://doi.org/10.1038/s41598-023-33232-w (2023).
10. Harris, R. *et al.* Phase transitions in a programmable quantum spin glass simulator. *Science* **361**, 162–165. https://doi.org/10.1126/science.aat2025 (2018).
11. Kairys, P. *et al.* Simulating the Shastry-Sutherland ising model using quantum annealing. *PRX Quantum* **1**, 020320. https://doi.org/10.1103/PRXQuantum.1.020320 (2020).
12. Kitai, K. *et al.* Designing metamaterials with quantum annealing and factorization machines. *Phys. Rev. Res.* **2**, 013319. https://doi.org/10.1103/PhysRevResearch.2.013319 (2020).
13. Liu, J. *et al.* Boltzmann machine modeling of layered MoS_2 synthesis on a quantum annealer. *Comput. Mater. Sci.* **173**, 109429. https://doi.org/10.1016/j.commatsci.2019.109429 (2020).
14. Kadowaki, T. & Nishimori, H. Quantum annealing in the transverse Ising model. *Phys. Rev. E* **58**, 5355. https://doi.org/10.1103/PhysRevE.58.5355 (1998).
15. Morita, S. & Nishimori, H. Mathematical foundation of quantum annealing. *J. Math. Phys.* **49**, 125210. https://doi.org/10.1063/1.2995837 (2008).
16. Mukherjee, S. & Chakrabarti, B. K. On the question of ergodicity in quantum spin glass phase and its role in quantum annealing. *J. Phys. Soc. Jpn.* **88**, 061004. https://doi.org/10.7566/JPSJ.88.061004 (2019).
17. Chakrabarti, B. K. & Mukherjee, S. Quantum annealing and computation. In *Reference Module in Materials Science and Materials Engineering*. https://doi.org/10.1016/B978-0-323-90800-9.00057-3 (Elsevier, 2023).
18. Nelson, J., Vuffray, M., Lokhov, A., Albash, T. & Coffrin, C. High-quality thermal Gibbs sampling with quantum annealing hardware. *Phys. Rev. Appl.* **17**, 044046. https://doi.org/10.1103/PhysRevApplied.17.044046 (2022).
19. Vuffray, M., Coffrin, C., Kharkov, Y. & Lokhov, A. Programmable quantum annealers as noisy Gibbs samplers. *PRX Quantum* **3**, 020317. https://doi.org/10.1103/PRXQuantum.3.020317 (2022).
20. Mandrà, S., Zhu, Z. & Katzgraber, H. Exponentially biased ground-state sampling of quantum annealing machines with transverse-field driving hamiltonians. *Phys. Rev. Lett.* **118**, 070502. https://doi.org/10.1103/PhysRevLett.118.070502 (2017).
21. Könz, M., Mazzola, G., Ochoa, A., Katzgraber, H. & Troyer, M. Uncertain fate of fair sampling in quantum annealing. *Phys. Rev. A* **100**, 030303. https://doi.org/10.1103/PhysRevA.100.030303 (2019).

22. Pelofske, E., Golden, J., Bärtschi, A., O'Malley, D. & Eidenbenz, S. Sampling on NISQ Devices: "Who's the Fairest One of All?" in 2021 *IEEE International Conference on Quantum Computing and Engineering (QCE)*, 207–217, https://doi.org/10.1109/QCE52317.2021.00038 (2021).
23. Ochoa, A., Jacob, D., Mandrà, S. & Katzgraber, H. Feeding the multitude: A polynomial-time algorithm to improve sampling. *Phys. Rev. E* **99**, 043306. https://doi.org/10.1103/PhysRevE.99.043306 (2019).
24. Kumar, V., Tomlin, C., Nehrkorn, C., O'Malley, D. & Dulny III, J. Achieving fair sampling in quantum annealing. Preprint at https://doi.org/10.48550/arXiv.2007.08487 (2020).
25. Metropolis, N., Rosenbluth, A., Rosenbluth, M. & Teller, A. Equation of state calculations by fast computing machines. *J. Chem. Phys.* **21**, 1087–1092. https://doi.org/10.1063/1.1699114 (1953).
26. Landau, D. & Binder, K. *A Guide to Monte Carlo Simulations in Statistical Physics* (Cambridge University Press, 2021).
27. Wang, F. & Landau, D. P. Efficient, multiple-range random walk algorithm to calculate the density of states. *Phys. Rev. Lett.* **86**, 2050–2053. https://doi.org/10.1103/PhysRevLett.86.2050 (2001).
28. Dall, J. & Sibani, P. Faster Monte Carlo simulations at low temperatures. The waiting time method. *Comput. Phys. Commun.* **141**, 260–267. https://doi.org/10.1016/S0010-4655(01)00412-X (2001).
29. Zhu, Z., Ochoa, A. & Katzgraber, H. Fair sampling of ground-state configurations of binary optimization problems. *Phys. Rev. E* **99**, 063314. https://doi.org/10.1103/PhysRevE.99.063314 (2019).
30. Somma, R., Batista, C. & Ortiz, G. Quantum approach to classical statistical mechanics. *Phys. Rev. Lett.* **99**, 030603. https://doi.org/10.1103/PhysRevLett.99.030603 (2007).
31. Yamamoto, M., Ohzeki, M. & Tanaka, K. Fair sampling by simulated annealing on quantum annealer. *J. Phys. Soc. Jpn.* **89**, 025002. https://doi.org/10.7566/JPSJ.89.025002 (2020).
32. Torlai, G. & Melko, R. Learning thermodynamics with Boltzmann machines. *Phys. Rev. B* **94**, 165134. https://doi.org/10.1103/PhysRevB.94.165134 (2016).
33. Xu, G. & Oates, W. Adaptive hyperparameter updating for training restricted Boltzmann machines on quantum annealers. *Sci. Rep.* **11**, 2727. https://doi.org/10.1038/s41598-021-82197-1 (2021).
34. Sato, T., Ohzeki, M. & Tanaka, K. Assessment of image generation by quantum annealer. *Sci. Rep.* **11**, 13523. https://doi.org/10.1038/s41598-021-92295-9 (2021).
35. Li, R., Albash, T. & Lidar, D. Limitations of error corrected quantum annealing in improving the performance of Boltzmann machines. *Quantum Sci. Technol.* **5**, 045010. https://doi.org/10.1088/2058-9565/ab9aab (2020).
36. Goto, H., Lin, Z. & Nakamura, Y. Boltzmann sampling from the Ising model using quantum heating of coupled nonlinear oscillators. *Sci. Rep.* **8**, 7154. https://doi.org/10.1038/s41598-018-25492-8 (2018).
37. Edwards, S. & Anderson, P. Theory of spin glasses. *J. Phys. F Met. Phys.* **5**, 965–974. https://doi.org/10.1088/0305-4608/5/5/017 (1975).
38. Sherrington, D. & Kirkpatrick, S. Solvable model of a spin-glass. *Phys. Rev. Lett.* **35**, 1792–1795. https://doi.org/10.1103/PhysRevLett.35.1792 (1975).
39. Zhang, B., Wagenbreth, G., Martin-Mayor, V. & Hen, I. Advantages of unfair quantum ground-state sampling. *Sci. Rep.* **7**, 1044. https://doi.org/10.1038/s41598-017-01096-6 (2017).
40. Huang, K. *Statistical Mechanics* (Wiley, 1987).
41. Pelofske, E., Hahn, G. & Djidjev, H. Optimizing the Spin Reversal Transform on the D-Wave 2000Q in *2019 IEEE International Conference on Rebooting Computing (ICRC)*, 1–8, https://doi.org/10.1109/ICRC.2019.8914719 (2019).
42. D-Wave Systems Inc. Reverse Quantum Annealing for Local Refinement of Solutions [Whitepaper]. https://www.dwavesys.com/resources/white-paper/reverse-quantum-annealing-for-local-refinement-of-solutions (2017).
43. Kadowaki, T. & Ohzeki, M. Experimental and theoretical study of thermodynamic effects in a quantum annealer. *J. Phys. Soc. Jpn.* **88**, 061008. https://doi.org/10.7566/JPSJ.88.061008 (2019).
44. Raymond, J. *et al.* Hybrid quantum annealing for larger-than-QPU lattice-structured problems. *ACM Trans. Quantum Comput.*https://doi.org/10.1145/3579368 *(2023).*
45. Johnson, M. *et al.* Quantum annealing with manufactured spins. *Nature* **473**, 194–198. https://doi.org/10.1038/nature10012 (2011).
46. Boixo, S. *et al.* Evidence for quantum annealing with more than one hundred qubits. *Nat. Phys.* **10**, 218–224. https://doi.org/10.1038/nphys2900 (2014).
47. Rønnow, T. *et al.* Defining and detecting quantum speedup. *Science* **345**, 420–423. https://doi.org/10.1126/science.1252319 (2014).
48. Warren, R. Mathematical methods for a quantum annealing computer. *J. Adv. Appl. Math.* **3**, 82–90. https://doi.org/10.22606/jaam.2018.33002 (2018).
49. Berwald, J. The mathematics of quantum-enabled applications on the D-wave quantum computer. *Not. Am. Math. Soc.* **66**, 832–841. https://doi.org/10.1090/noti1893 (2019).
50. D-Wave Systems Inc. Performance advantage in quantum Boltzmann sampling [Whitepaper]. https://www.dwavesys.com/resources/white-paper/performance-advantage-in-quantum-boltzmann-sampling (2017).
51. Golden, J. & O'Malley, D. Reverse annealing for nonnegative/binary matrix factorization. *PLoS One* **16**, e0244026. https://doi.org/10.1371/journal.pone.0244026 (2021).
52. Lucas, A. Ising formulations of many NP problems. *Front. Phys.*https://doi.org/10.3389/fphy.2014.00005 *(2014).*
53. D-Wave Leap quantum cloud service. https://cloud.dwavesys.com. Accessed 24 Feb 2023.
54. Choi, V. Minor-embedding in adiabatic quantum computation: II. Minor-universal graph design. *Quantum Inf. Process.* **10**, 343–353. https://doi.org/10.1007/s11128-010-0200-3 (2011).

Acknowledgements

This research was funded by the German Federal Ministry of Education and Research (BMBF) via the project ALANO and the Helmholtz project ZeDaBase. Open access was funded by the Deutsche Forschungsgemeinschaft (DFG, German Research Foundation) - 491111487. The authors gratefully acknowledge the Jülich Supercomputing Centre (https://www.fz-juelich.de/ias/jsc) for funding this project by providing computing time on the D-Wave Advantage^{TM} System JUPSI through the Jülich UNified Infrastructure for Quantum computing (JUNIQ).

Author contributions

R.S. and R.S. contributed to analytical and numerical calculations, methodology, visualization and analysis. Both authors contributed to the writing of the manuscript.

Funding

Open Access funding enabled and organized by Projekt DEAL.

Competing interests
The authors declare no competing interests.

Additional information
Correspondence and requests for materials should be addressed to R.S.

Reprints and permissions information is available at www.nature.com/reprints.

Publisher's note Springer Nature remains neutral with regard to jurisdictional claims in published maps and institutional affiliations.